UNIVERSITY OF BLIDA 1

Faculty of Science

Department of physics

Laboratory of Theoretical Physics and Interaction of Radiations with Matter

DOCTORAL THESIS

Specialty: Fundamental and Applied Physics

DEVELOPMENT OF A GAMMA SPECTROMETRY DETECTION SYSTEM FOR RADIOACTIVITY EVALUATION IN DIFFERENT TYPES OF SAMPLES

By

Salma BOUKHALFA

Approved by:

MOHAMED SIDOUMOU	Prof.	U. of Blida-1	President
GUESMIA ABDELKADER	MCA	U. of Blida-1	Examiner
BELGAID MOHAMED	Prof.	USTHB	Examiner
ANIS SAMY AMINE DIB	Prof.	USTOMB	Examiner
KHELIFI RACHID	Prof.	U. of Blida-1	Supervisor

Blida, 2021

ABSTRACT

This thesis has threefold objectives: 1) attempting to propose a solution for the poor energy resolution problem of NaI(Tl) spectrometer using unfolding GRAVEL code; 2) detection efficiency measurement of large samples using Monte Carlo codes i.e., MC_Gamma and Geant4; and 3) the quantification of naturally occurring radionuclides ^{232}Th, ^{40}K and ^{238}U found in the environmental samples (biological, geological, and polyethylene) using Gamma spectrometry chain. To achieve the first objective, a prior knowledge of natural background level, detector response function, Gaussian Energy Broadening, and measured spectrum is required. Moreover, the second objective needs to describe the experimental setup, and therefore, that should be validated with standard sources. In addition, the third objective merges the methodologies adopted in the first and second objectives.

The results have shown that 1) the escape peaks, Compton continuum, and background radiation had been successfully removed so the incident spectrum was restored; 2) the Monte Carlo computational code revealed satisfactory results where an experimental validation using ^{137}Cs, KCl calibration sources was conducted. Therefore, satisfactory results were presented by Geant4, MC_Gamma**,** and GRAVEL; 3) Quantification of NORMs was performed in biological, geological, and polyethylene samples following the unfolding process and Monte Carlo calibration. The measured activities were used to evaluate the dosimetric parameters such as hazard indices, radium equivalent, threshold consumption, annual committed dose for the biological samples, and annual doses for the geological samples.

The results show: 3.86 E–2, 1.08 E–2, and 9 E–4 mSv of the annual doses (of geological samples) is received from brick, cement, and gravel respectiviely; the annual consumption of milk and wheat for adult (biological samples), should be equivalent to 98 g/day and 147 g/day respectively.

Keywords: NaI(Tl), gamma spectrometry, Monte Carlo, Geant4, detection efficiency, econvolution, natural radioactivity, dosimetry.

RESUME

Cette thèse a trois objectifs : 1) tenter de proposer une solution au problème du chevauchement des en utilisant le code itératif GRAVEL ; 2) mesure de l'efficacité de détection des échantillons volumineux à l'aide de codes Monte Carlo : MC_Gamma et Geant4 ; et 3) la quantification des radionucléides naturels ^{232}Th, ^{40}K et ^{238}U trouvés dans les échantillons environnementaux (biologiques, géologiques et polyéthylène) à l'aide de la chaîne de spectrométrie Gamma.

Pour atteindre le premier objectif, une connaissance préalable du niveau de bruit de fond naturel, de la fonction de réponse du détecteur, de l'élargissement gaussien (GEB), et de l'énergie et du spectre mesuré est requise. De plus, le deuxième objectif doit décrire la diapositive expérimentale, et donc, qui doit être validé avec des sources étalons. De plus, le troisième objectif fusionne les méthodologies adoptées dans les premier et deuxième objectifs.

Les résultats ont montré que 1) les pics d'échappement, le continuum de Compton et le rayonnement de fond avaient été supprimés avec succès, de sorte que le spectre incident a été restauré ; 2) le code de calcul Monte Carlo a révélé des résultats satisfaisants où une validation expérimentale utilisant des sources d'étalonnage de ^{137}Cs, KCl a été menée. Par conséquent, des résultats satisfaisants ont été présentés par Geant4, MC_Gamma et GRAVEL ; 3) La quantification des NORM a été réalisée dans des échantillons biologiques, géologiques et de polyéthylène après le processus de dépliage et l'étalonnage Monte Carlo. Les activités mesurées ont permis d'évaluer les paramètres dosimétriques tels que les indices de risque, le radium équivalent, le seuil de consommation, la dose annuelle engagée pour les échantillons biologiques et les doses annuelles pour les échantillons géologiques.

Les résultats montrent : 3,86 E-2, 1,08 E-2 et 9 E-4 mSv des doses annuelles (d'échantillons géologiques) sont reçues de la brique, du ciment et du gravier respectivement ; la consommation annuelle de lait et de blé pour adulte (échantillons biologiques), devrait être équivalente à 98 g/jour et 147 g/jour respectivement.

Mots clés : NaI(Tl), spectrométrie gamma, Monte Carlo, Geant4, GRAVEL, efficacité de détection, deconvolution, radioactivité naturelle, dosimetrie.

Contenant

Contenant

Contenant

Figure List

CHAPTRE I : GAMMA SPECTROMETRY: FROM RADIOACTIVITY TO DOSIMETRY

CHAPTRE II : EFFICIENCY COMPUTATIONAL MODEL

CHAPTRE III : GAMMA SPECTRA UNFOLDING : INVERSE MATRIX METHOD

CHAPTRE IV : DOSIMETRY AND APPLICATION TO ENVIRONMENTAL RADIOACTIVITY MEASUREMENT

Figure List

APPENDIX A : MONTE CARLO SIMULATIONS

TABLES LIST

CHAPTRE I : GAMMA SPECTROMETRY: FROM RADIOACTIVITY TO DOSIMETRY

CHAPTRE II : EFFICIENCY COMPUTATIONAL MODEL

CHAPTRE III : GAMMA SPECTRA UNFOLDING : INVERSE MATRIX METHOD

CHAPTRE IV : DOSIMETRY AND APPLICATION TO ENVIRONMENTAL RADIOACTIVITY MEASUREMENT

APPENDIX B : EFFECTIVE ATOMIC NUMBER

ABREVIATIONS LIST

A_i	Activity concentration of *i* radionuclide ($Bq.kg^{-1}$)
ADC	Analog Digital Converter
BDL	Below Detection Limit
BGO	Bismuth Germanate
CE	European Commission
CsI(Tl)	Thallium Activated Cesium Iodide
D	Absorbed dose ($nGy.h^{-1}$)
$D_{average}$	Average dose ($Sv.y^{-1}$)
$D_{IThreshold}$	Thresold consumption rate dose ($kg.y^{-1}$)
$D_{ingestion}$	Ingestion dose coefficient ($Sv.Bq^{-1}$)
E	Annual dose ($mSv.y^{-1}$)
FLUKA	FLUktuierende KAskade
FWHM	Full Width at Half Maximum
Geant4	GEometry ANd Tracking.
GRAVEL	Iterative algorithm for spectra unfolding.
GSA	Gamma Spectrometry Analyses
H_{ex}	External hazard index
H_{in}	Internal hazard index.
HPGe	Hight Purity Germanium
H_T	Equivalent dose of tissue or organ T
IAEA	International Atomic Energy Agency
ICRP	International Commission on Radiological Protection
INAA	Instrumental Neutron Activation Analyses
KERMA	Kinetic Energy Released in Matter
LaBr	Lanthanum Bromide
MAXED	Computer code for MAXimum Entropy Deconvolution
MC_Gamma	Monte Carlo for Gamma particle
MCA	Multi Channel Analyser
MCNP	Monte Carlo for N particle
MgO	Magnesium Oxide powder
NAA	Neutron Activation Analyses
NaI(Tl)	Sodium iodide (NaI) detector activated by thallium (Tl)
NORM	Naturally Occurring Radioactive Materials
ONS	Office National des Statistiques.
PENELOP	Penetration and Energy Loss of Positrons and Electrons
PMT	Photo Multiplicator Tube
R (E, E_0)	Detector response function
R_{aeq}	Radium equivalent ($Bq.\ kg^{-1}$)
ROI	Region Of Interest.
SAND II	Spectrum unfolding code based on an iterative adjustment
UNSCEAR	United Nation Scientific Committee on the Effects of Atomic Radiation
USDA	U.S Department of Agricultural
V	Source Volume
WHO	World Health Organisation
W_R	Radiation weight factor
W_T	Tissue weight factor
XCom	U.S Department of Agricultural
XRF	X-Ray Fluorescence

Y_{intake}	Yearly intake ($Bq.y^{-1}$)
Z (E)	Incident spectrum
Z_{effe}	Effective atomic number.
χ	Chi-value.
ε	Detection efficiency.
μ	Linear attenuation coefficient
ρ	Density of the material
Φ (E)	Measured spectrum
η	Electronic noise.
Ω	solid angle (Steradiant)

GENERAL INTRODUCTION

Many international organizations of human protection from radiation exposure are interested in the natural and/or artificial radioactivity evaluation; as an objective to measure and protect the public as well as the biota against the effects of exposure to ionizing radiations. The radiations are emitted from many sources including medical therapy, cosmic radiations, terrestrial radionuclides etc. For instance, the disintegration of terrestrial radionuclides produces the emission of radon and thoron which are transmitted through inhalation or ingestion and associated with the emission of alpha, beta, and gamma particles.

In environmental sciences, scholars argued that there are about 340 Natural Occurring Radioactive Materials (NORM) also called terrestrial background radiations. Moreover, they assumed more than 60 radio – isotopes that could be found in different matrixes such as soil [1 – 8], sediments [9 – 14], foodstuff [15],construction materials [16 – 26], water [27], and in food chains.

The international organizations of IAEA (2010) [28] and UNSCEAR (1988 [29], 2000 [30]) reported that the majority of the universal dose is accruing from natural sources. Moreover, the WHO 2012 [31] reported that 19.9 % of annual absorbed dose (mSv/year) for the world population is issued from medical diagnostic, 0.98 % from human – made sources, and more than 79 % emitted from natural radiations in which 15.7 % and 12.7 % from terrestrial and cosmic radiations respectively, 9.48 % from internal exposure, and 41.2 % from the series decay of uranium and thorium isotopes i.e., radon and thoron.

Other factors like agricultural and industrial human activities can also contribute to the annual absorbed dose by increasing the concentration of the NORM's in environmental samples, which may cause radiological contamination and diseasessuch as cancers, chronic lung, etc. [32 – 33].

In agricultural soils, the concentration of thorium and uranium is increased due to the extensive use of fertilizers which are technologically optimized agricultural products and rich in phosphate [34]. The fertilizers absorption by plants' roots can be successively involvedinthe food chain throughthe fast transmission to vegetables, fruits, leaves, plants, fodders, flowers, etc [35]. In addition, the mining activities can increase the radioactivity level, therefore the background level becomes higher.

In the ecosystem, research on radioactive radiation is still not properly quantified. Therefore, many national and international studies were conducted to assess and control the concentration of the NORM's (^{238}U, ^{232}Th, and ^{40}K) in different environmental samples using many experimental technics e.g., NAA, INAA, Alpha spectrometry, radiochemical separation, Industry Coupled Plasma Mass Spectrometry (ICP – MS), and GSA, etc.

Recently, more technological nuclear equipment for radiations measurements consists of a mobile gamma spectrometry system called in – situ and airborne (aerial) survey team. This was developed for the localization, identification, quantification, consumable inspection hygiene, and dose rate estimation for some radioelements such as ^{137}Cs, ^{99}Tr, NORM's, etc., in live time.

The most common gamma – ray spectrometers are High Purity Germanium detectors and light scintillators e.g., $LaBr_3$, NaI(Tl), and other types of inorganic or organic detectors. The physical characteristics such as detection efficiency, response time, energy resolution, cost, empirical conditions like temperature are the main important criteria for spectrometer choice in laboratory, aerial, and in – situ measurement. This technic is very fast for qualitative and/or quantitative analyses as well as suitable forthe non – destructive method.

The HPGe detectors have an excellent energy resolution of about 2 %[1], which is very appropriate for peak searching. The spectrometry analyses require large size and low – cost detectors. However, HPGe detectors are characterized by low detection efficiency due to their limited size and their high market cost.

On the other hand, the sodium iodine NaI(Tl) scintillator presents the lowest cost spectrometers. Their high detection efficiency attributed to their unlimited size make the NaI(Tl) to a large extent as the most detectors for radiation monitoring. The main disadvantage of the NaI(Tl) spectrometer is the poor energy resolution at a low energetic range. Where the interaction of high gamma energy produces secondary peaks e.g., first and second escape peaks in addition to scattered photons at different θ angles. These factors prevent us from reliable analysis especially when quantification is needed. For solution, the quantitative problem can be solved using anti – Compton systems, unfolding process, etc, presenting significant and reliable data at the end.

[1]FWHM was measured for ^{60}Co peak (1332 keV).

The present thesis aimed to develop a detection system coupled with a NaI(Tl) gamma spectrometer for natural radioactivity evaluation in different environmental samples.

Three main objectives were pursued: the first objective endeavored the modelization of NaI(Tl) spectrometer using Monte Carlo simulation codes. The second consisted of the unfolding process for the experimental spectrum counted by NaI(Tl) detector. The third was to the quantification of NORMs in different environmental samples using combined methods of the first and second objectives.

In this regard, the present thesis encompasses four chapters, two annexes, and a proposed algorithm applied for radioactivity measurements.

The first chapter discusses the theoretical background of the radioactivity phenomenon, the interaction of gamma radiations with the matter, detection system, and dosimetry of ionizing radiations.

The second chapter presents different methods e.g., mathematical expressions, experimental measurements, and Monte Carlo simulation for efficiency calibration. An example of the Monte Carlo model for large efficiency measurements was presented and tested by a standard source.

The third chapter consists of gamma spectra unfolding using iterative code. The energetic response function and the mathematical model of the scintillator spectrometer were used to restore the emitted spectra. The validation of the measured and the followed methodology is presented.

The forth chapter is dedicated to natural radioactivity evaluation combined with Monte Carlo calibration and unfolding process. The efficiency curves for different environmental matrixes were plotted taking into account the validated detector model, densities, and elemental composition of the studied samples. Then, the measured spectra were unfolded for two gamma windows corresponding to ^{40}K and ^{238}U. In this part, the background radiations, escape, and scattered peaks were successively subtracted. The net areas were calculated using the output unfolding files. The obtained results i.e., detection efficiency and the net surface will be used to calculate the specific activities and the dosimetric parameters.

Finally, **general conclusion** with some perspectives is presented. In addition, appendices contain the Monte Carlo codes and effective atomic number measurement, and

the proposed algorithm for radioactivity measurement written in C++ language. The entred package such as densities, effective atomic numbers, efficiency curves, gamma line intensities, and unfolding surfaces are saved in the data program. Therefore, the manipulator can easily pass from density to mass activity in $Bq.kg^{-1}$.

CHAPTER I: GAMMA SPECTROMETRY

FROM RADIOACTIVITY TO DOSIMETRY

The main purpose of this chapter is to describe the radioactivity sources and the interaction of the gamma radiations with the matter. In this description, we highlight the detection system and the main spectrometer used in gamma – ray spectrometry. Subsequently, we present the effect of the incident radiation on human bodies by defining the dose meaning.

The main bibliographical sources of this Chapter are the books of G Knoll, N Tsoulfanidis, and F Khan.

1.1. Radioactivity

In 1898, Antoine Becquerel discovered a new spontaneous and continuous phenomenon of non– stable radioactive elements situated at exciting levels called the father nucleus. These elements disintegrated to a lower energetic level with the emission of nuclear particles $(\alpha, \beta ...)$ or wave radiation (photons). Accordingly, the new radioelement called the daughter nucleus is formed. The processes of disintegration should stop once having a stable daughter nucleus. In this context, two types of radioactivity can be distinguished:

1.1.1. Artificial sources

The man – made sources were discovered in 1934 by Irène and Fédéric Juliout-Curie. Their formation is due to the production of the non – stable nucleus through, for instance, the bombardment of stable elements by nuclear particles, e.g., neutron, to inducing nuclear reaction. Therefore, new radioactive nuclei were formed. These reactions are generally made in nuclear reactors, research centers, hospitals for an energetic production purpose, scientific research, medical applications (radio – tracers, radioisotopes, sterilization of medical instruments, radiotherapy, etc.), among others. Consequently, their existence level is a function of the technology development and the research works.

It is worth mentioning that the anthropogenic radioelements have generally a short half – life. However, some of these are notable like ^{137}Cs, ^{70}Sr, and ^{84}Kr with a half– life of 30, 28.1, and 10.73 years respectively.

1.1.2. Natural radioactivity source

This source is a spontaneous phenomenon, caused by whether natural particles originally cosmic or terrestrial radioelements which are called primordial. The cosmic radioactivity is due to the presence of galactic radiation, primary radiation, coming from the sun, stars, other galaxies outward the solar system, or by the interaction of primary radiation (high energetic particle) with atmospheric particles. Consequently, secondary particles like protons, neutrons, muons, photons are produced [36]. On the other side, the primordial radioelements are classed on three natural radioactive series, namely: Uranium – 235 ($T = 7.1 \times 10^8$ y), Uranium – 238 ($T = 4.47 \times 10^9$ y), Thorium – 232 ($T = 14.05 \times 10^8$ y), and Potassium – 40 ($T = 1.24 \times 10^9$ y). The disintegration of ^{238}U, ^{235}U, and ^{232}Th is presented in Figure1.1. These radionuclides can be found in natural matrixes such as sea or river waters, rocks, sediments, soil, food, etc. It is important to note that the natural radioactivity level can vary according to geological and time function. This is because of

natural factors such as soil moisture, snow, and atmospheric concentration of radium – 226 [37 – 39]. From each series decay, it can be found four radio – isotopes of radium, namely: ^{223}Ra (Alpha emitter, coming from ^{235}U decay with a half – life of 11.43 ± 0.05 day); ^{224}Ra (Alpha emitter, coming from series decay of ^{223}Th chain, with a half – life of 3.627 ± 0.07 day); ^{226}Ra (Alpha particle emitter, member of ^{238}U series decay with a half – life of $5.844 \times 10^5 \pm 0.025 \times 10^5$ days); and ^{228}Ra (Beta minus particle emitter, member of ^{232}Th series decay with a half – life of 2100 ± 11 days) [40]. As result, three primordial series decay forms approximately 33 radioisotopes and three stable elements.

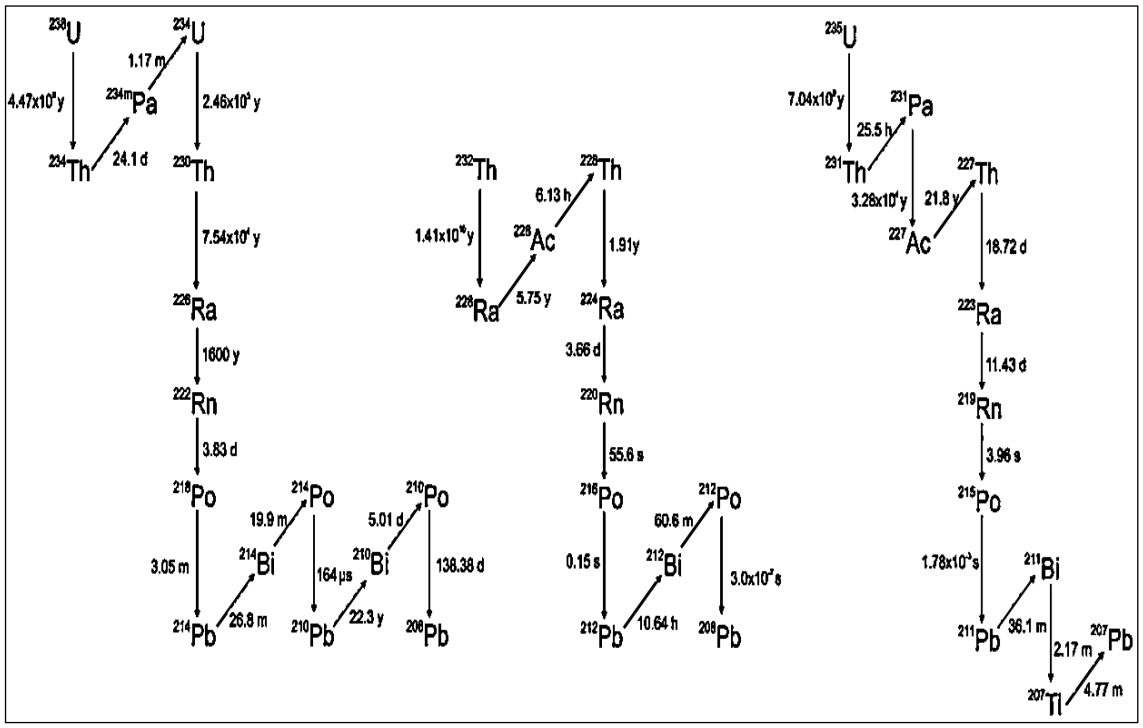

Figure 1. 1: Disintegration chain of ^{235}U, ^{238}U, and ^{232}Th.

1.1.3. Radioactive equilibrium

The transition from the excited to the low – excited ground creates a nuclear equilibrium whereby the ratio of the father to the daughter will be constant. Moreover, there are two types of nuclear equilibrium that can be distinguished [41]:

Firstly, it consists of transient equilibrium that occurs when the half – life of the nucleus parent (T_1) is not much greater than the half–life of the nucleus daughter (T_2) as well as their relative activities decrease as a time function (equation 1.1). This type of equilibrium is applied in medical imaging where the half – life of ^{99}Mo (67 hours) is greather than the ^{99m}Tc (6 hours).

$$\frac{A_2}{A_1} = \frac{T_2}{T_1 - T_2} = \frac{\lambda_1}{\lambda_2 - \lambda_1} \tag{1.1}$$

On the contrary, secular equilibrium is achieved when the half – life of the progeny, e.g., ^{222}Ra, is very smaller than the half – life of the father nucleus, e.g.,^{226}Ra. Therefore, their corresponding activities are neither increasing nor decreasing over time (equation 1.2).

$$A_2 \cong A_1 \tag{1.2}$$

Finally, the induced photons, e.g., gamma decay, pass through any type of matter (density and atomic number), and, from this point, different types of interaction processes are produced.In the next section, only three types of gamma particle interaction have been discussed.

1.2. Interaction of gamma radiation with matter

1.2.1. Photoelectric effect

In the photoelectric process, the incident photons interact with the atomic electron then it is entirely absorbed (Figure 1.2). The photoelectron particle is produced probably emitted from the K shell of the target atoms. The kinetic energy of the outgoing electron is [42 –43]:

$$E_e = E_\gamma - E_{bindingenergy\ of\ the\ electron} \tag{1.3}$$

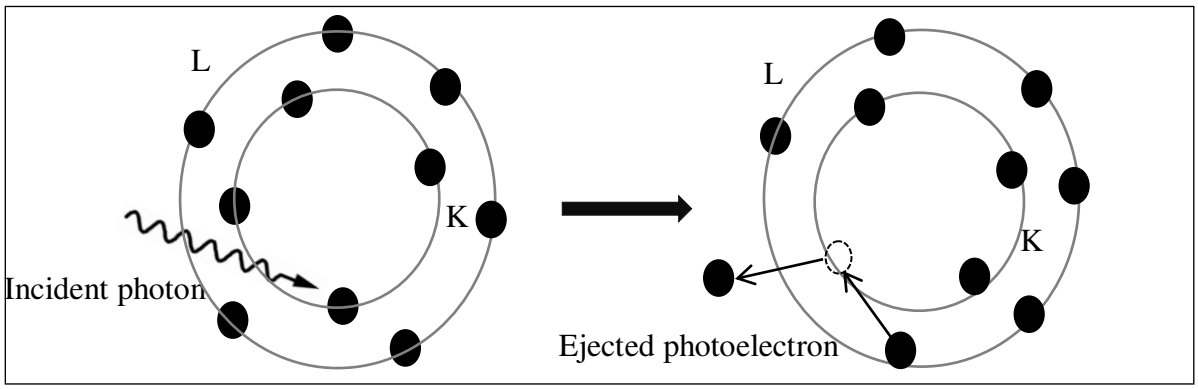

Figure 1. 2: Photoelectric effect.

1.2.2. Compton scattering

In the incoherent scattering or Compton – effect, the incident γ – ray (E_γ) is deflected with θ angle on a free electron. A part of its energy and momentum is transferred to the recoil electron (Figure 1.3). Due to the variation of scattering angle, the energy of scattered photon $(E_\gamma^{'})$ at θ deviation can be written as following [42 – 43]:

$$E_{\gamma}^{'} = \frac{E_{\gamma}}{1+\frac{E_{\gamma}}{m_0c^2}(1-\cos\theta)} \tag{1.4}$$

The recoil electron (knocked electron) energy (E_e) in the Compton process is:

$$E_e = E_{\gamma} \times \frac{\frac{2E_{\gamma}}{m_0c^2}}{1-\frac{2E_{\gamma}}{m_0c^2}+\left(1+\frac{E_{\gamma}}{m_0c^2}\right)^2 \times \tan^2\varphi} \tag{1.5}$$

The energy range of Compton electrons varies from $E_{Min}(\theta=0)$ to $E_{Max}(\theta=\pi)$ values:

$$\begin{cases} E_{Min}=0 \\ E_{Max}=h\nu-\dfrac{h\nu}{1+\dfrac{2h\nu}{m_0c^2}}; \quad Compton \quad edge \end{cases} \tag{1.6}$$

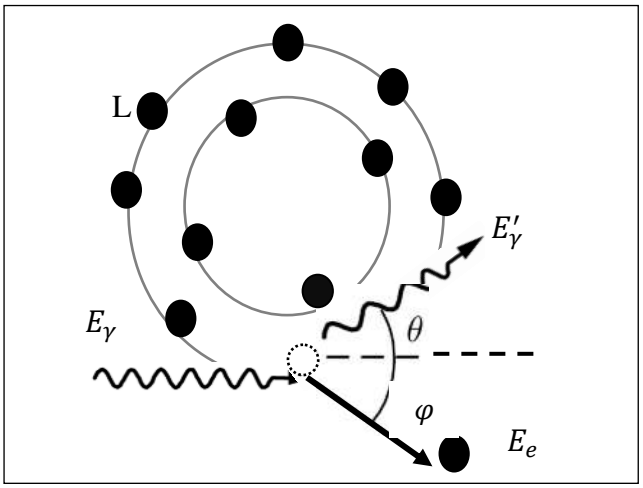

Figure 1. 3: Compton scattering.

1.2.3. Pairs production

The interaction between the incident photon and atom nucleons, in a Colombian field of a nucleus, generates a pair of e^- and e^+ (Figure 1.4). The nuclear process is possible when the incident gamma energy is great or equal to 1.022 MeV [42 – 43]

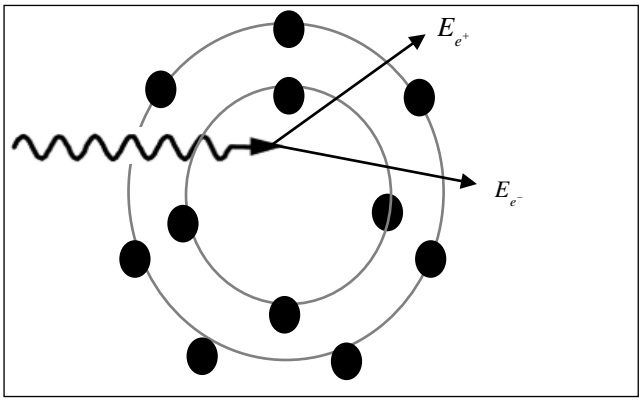

Figure 1. 4: Pairs production.

Figure 1.5 describes the three important major interactions of gamma – ray in different absorber materials as atomic number and energy function.

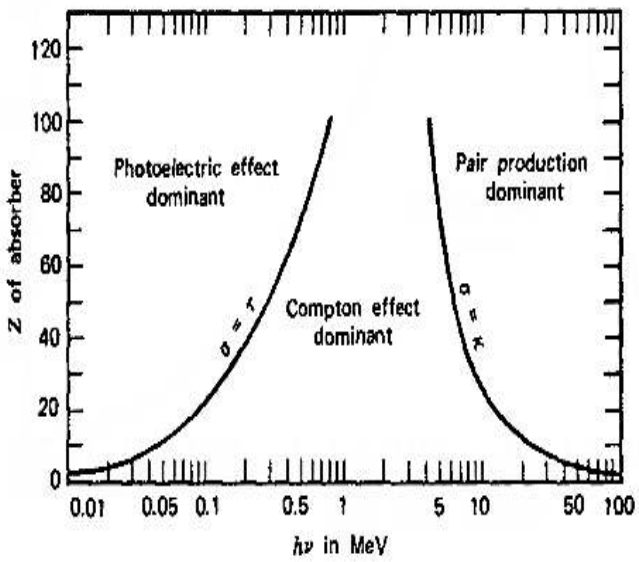

Figure 1. 5: Relative importance of the 3 major types of gamma interaction in different absorbers. From Evans (1955) [44].

In Chapter 2, we present a spectra example explaining the induced peaks after the interaction of high photon energy with scintillator crystal.

As previously stated, other types of photon interaction as Rayleigh and Thomson, would not be mentioned in this section.

1.2.4. Photon beam attenuation

Interaction of γ –radiation with different mediums by different physical processes per unit of path length is defined by gamma-ray attenuation coefficient $\mu(E)$ or macroscopic cross-section [42 –43].

Let I_0 and I, the intensity of the incident and transmitted photon are respectively crossed at X thickness of the target. This latter is characterized by density ρ and effective atomic number Z_{effe}. In addition, the following Beer – Lambert law is given to calculate the linear attenuation coefficient of any sample as follows [53]:

$$\mu(E) = \frac{1}{X} \ln\left(\frac{I_0}{I}\right) \tag{1.7}$$

Experimentally, equation (1.7) is applied just in narrow beam geometry (Figure 1.6) where the incident photons are perpendicular to the target (sample).

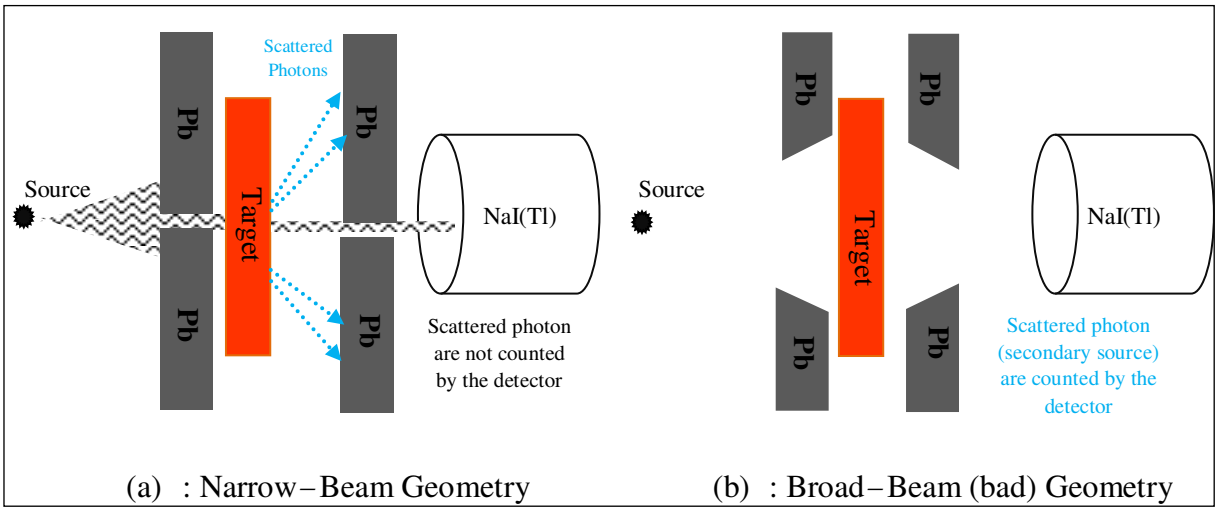

Figure 1. 6: Narrow and broad beam geometry for measurement of attenuation in absorbing materials.

It is important to note that the modeling photon attenuation through any traveled medium can be successively done using computer programs e.g., Geant4, MCNP, and XCom data (See, Appendix A). To conclude, the measurement of the interacted gammas is acquired using gamma – ray spectrometers. In the next section, the gamma detectors and their associated nuclear instrument will be presented.

1.3. Gamma spectrometry measurement

1.3.1. Scintillator spectrometers

Solid, liquid, and gas are scintillator materials associated with the scintillation light emission. Two types of scintillator detector can be physically established: *organic* (e.g, liquid scintillators, plastic scintillators, and a crystal); and *inorganic* scintillator existed only in crystal format e.g., NaI(Tl), CsI(Tl), BGO, etc.

The *liquid scintillator* generally has organic structure. It is often constructed by two elements, and in some cases, a third element can be added as an objective to shift the wavelength interval. In addition, it is applied for the quantification of β^- and ^{12}C particle, for example. This type of scintillator is very cheap in commercial stores, but it can be easily damaged under exposure to intense radiation [42 – 43]. The mechanism of fluorescence of this detector type is made by intermediate energetic states.

The second type of organic spectrometer consists ofa *plastic scintillator* is formed by thermal polymerization reaction which is organic or inorganic materials added to the solvent. This scintillator is suitable for fast timing measurement with a decay time of 2 ns

order. They have low–cost and are easily fabricated, and available at different size processes [42 – 43].

The mechanism of scintillation in an *inorganic detector* is perfectly made by adding a small fraction of impurities (activator) in the crystal (Figure 1.7). The objective is to enhance the probability of returning electrons to the valence band with the emission of visible photons during the de-excitation process [42, 45].

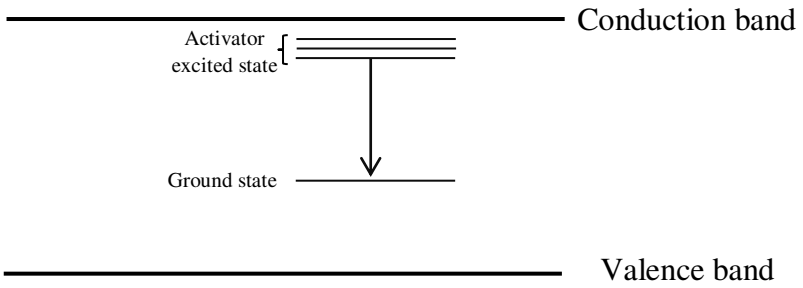

Figure 1. 7: Scintillation mechanism in the activator scintillator [43].

Afterward, the emitted light will be converted into electrons using the scintillator integral part that is located at the back of the crystal and called the photo – multiplicator tube (PMT). The process of collection, conversion, and multiplication are starting as follow (Figure 1.8):

Firstly, the incident light of quantic energy that is equal to *hv* will be converted into electrons, called photo-electrons, inside the photocathode material. Then, the incident electron (primary) will be transferred to the first dynode and guided under the effect of the electrical field. This latter aims to lead the direction of the electrons. At this instant, secondary electrons are produced. Between each dynode, an electrical field was applied to succeed the amplification process (HV). Production of secondary electrons is explained by the amplification phenomenon (10^6 times) where the conversion and amplification mechanism are quickly made, in 10^{-9} seconds in general [42 – 43].

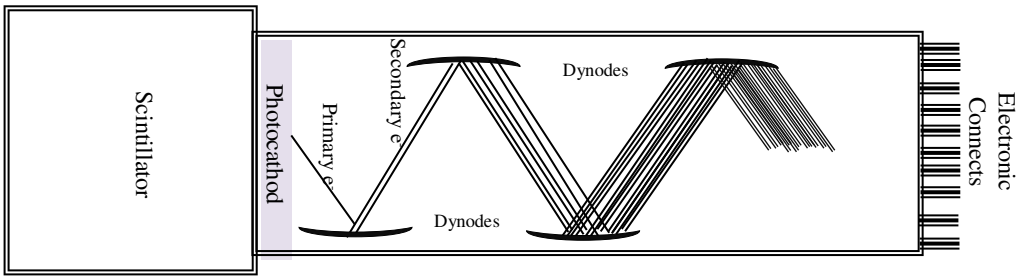

Figure 1. 8: Schematic of the photo - multiplicator tube.

1.3.2. HPGe spectrometers

A semi – conductor diode with a P.I.N structure is fabricated. It is presented as excellent gamma spectrometers with different sizes and/or geometry. Three types of HPGe configuration can be distinguished (Figure 1.9) [42, 46]:

– *Planar Geometry:* presented as a germanium disc (Figure 1.9.a) available in different diameters, having an electrical contact on the flat surfaces is applied. A thin window on Carbon or Beryllium was added to the front-end of the detector to collect the low energetic radiations. This type of geometry can be successfully used resulting in high energetic resolution and efficiency.

– *Coaxial Geometry*: configured in a hollow cylinder (Figure 1.9.b), larger than planer configuration. The main characteristics are: high energy resolution, a good detection efficiency, and suitable for low energetic range (Beryllium window);

– *Well – Type Geometry:* same configuration of a coaxial detector, but on the upside-down (Figure 1.9.c). This type is suitable for low radioactivity levels, where the detection efficiency is 4π in order and small sample quantity, etc. It is extremely sensitive to the summing effect.

Table 1. 1 : Energy resolution (%) of HPGe detector in different configurations. From Knoll, 2000.

Energy (keV) / *Configuration*	*122*	*1332*
Coaxial	0.80	3.40
Planar	0.65	2.00
Well – Type	1.2	2.1

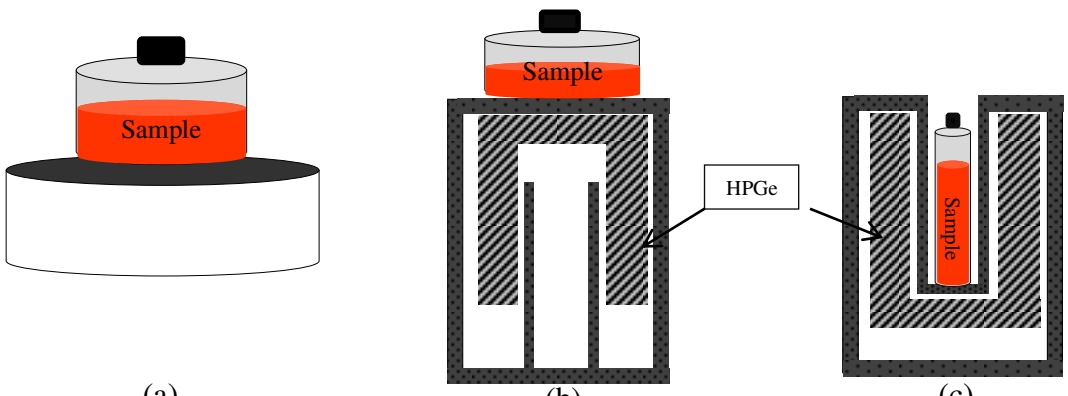

Figure 1. 9: Hight Purity Germanium configuration: planar, coaxial, and well - type.

Table 1. 2: Energy resolution (%) of HPGe and NaI(Tl) detector.

Materials	*Size*	*Energy resolution*[*]	*Detection efficiency*[**]
HPGe	Limited	2.18 %	< 1 %
NaI(Tl)	Unlimited	23.33 %	3 % – 10 %

*Energy resolution of different detectors was measured for X-ray beam at 140 keV [43, 47].

** [48 - 49]

Figure 1.10 presents gamma spectra distribution counted for NaI(Tl) and HPGe spectrometer. In practice, the choice of the nuclear spectrometer is depending on the application and the objective of the measurements.

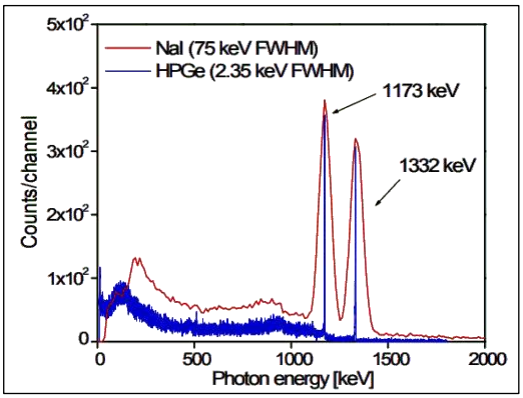

Figure 1. 10: Comparison of NaI(Tl) and HPGe spectra for cobalt - 60. Adapted from : Radioisotopes et méthodologies de rayonnement I, II. SooHyunByun, note des cours. Université McMaster, Canada[54].

1.3.3. Acquisition chain

It consists of nuclear modules (Figure 1.12) composed of Amplificatory, Pre – amplificatory, Multi-Channel Analyzer (MCA), and Analogic Digital Converter (ADC). The role of each instrument is [42 –43]:

– *High Voltage Power Supply*: it is an instrumental model that aims at the control and the monitoring of the High Voltage Power supply. In Figure 1.12, column a, the front panel of HVP with red light indicator aims to indicate the manipulator if the high voltage is On/Off;

– *Preamplifier:* is the first nuclear instrument directly placed on the back of the detector. The main objective of the preamplifier is to minimize the source noise, attaching the detector output to the rest of the detection system, and converting the current impulsion that comes from the detector to the voltage impulsion (impedance). Figure 1.12, column b, presents the preamplifier interface;

– *Amplifier*: is an electronic module, located after the preamplifier, aimed to increase the amplitude of the pulse (signal), and also to convert the input signal that is coming from the preamplifier into a suitable form for the presentation to the next part (ADC). (See, Figure 1.12, column c);

– *Analog – Digital Converter (ADC)*: it consists of the measurement of amplitude (V) of the conditioned voltage pulse (input) which will be transferred to MCA after amplitude numbering (address);

– *Multi-Channel Analyzer (MCA)*: it is mainly aimed to measure the pulse height distributions and organize them as histogram data (See Figure 1.12, column d). The horizontal and the vertical axes correspond to the number of counts (per channel) and the channel number or energy values respectively;

– *Oscilloscope*: is used to control the quality and noise of the measured signal and/or the noise change over time.

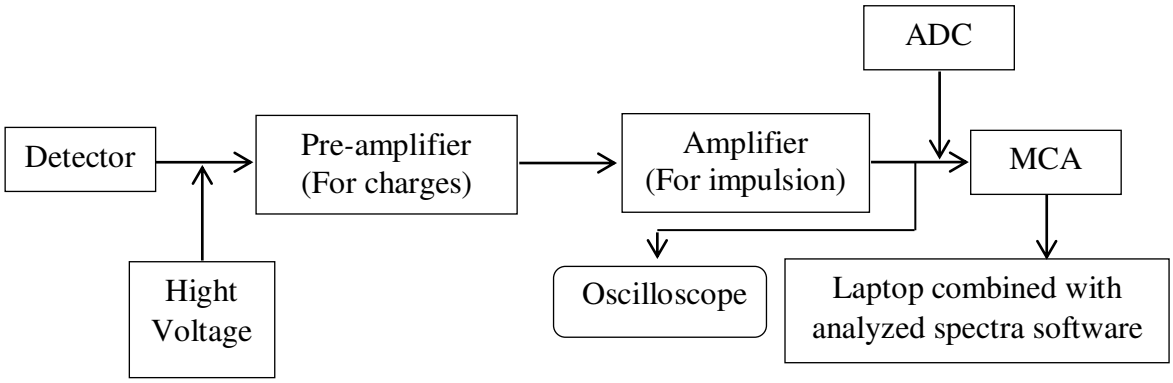

Figure 1. 11: Block diagram for spectrometry system.

(a) (b) (c) (d)

Figure 1. 12: Nuclear instrument used in detection system (From ORTEC Catalog). (a) Hight voltage supply, (b) Preamplifier, (c) Amplifier, (d): Analogue Digital Converter.

1.3.3.1. Energetic calibration

It consists of linear extrapolation between the energetic values (E) emitted from standard sources and their corresponding channel (C). The energetic calibration equation is written as follows [42]:

$$E = \alpha + \beta C + \gamma C^2 + ... \quad (1.8)$$

In practice, the manipulator must use a large number of standard sources to record their correspondent energies with their stored channels. After the affirmation of chain linearity, equation (1.8) takes the next form:

$$E = \alpha + \beta C \quad (1.9)$$

1.3.3.2. Efficiency calibration

It consists of an appropriate formula (polynomial, exponential, etc) fitted to relate the detection efficiency (in %) to energy as a function. Chapter 2 presents more details on the detection efficiency calibration for a point or extended sources.

1.4. Dosimetry of ionizing radiation

It aims to evaluate the biological damage received from the exposure of ionizing or non – ionizing radiation whether on human bodies called the individual dosimetry or on geological sites called the area dosimetry. Many international organizations, like UNSCEAR, ICRU, EC, etc., defined some rules, procedures, and limits, etc., to protect the individuals from the harmful radiation effects. Three main classes of radiation protection can be classified into physical, protection, and operational quantities. They can be explained as the followings:

1.4.1. Physical quantities

They are used to characterize the particle field and the physical effects of the deposed energy in the traveled medium, corresponding to radiometric and dosimetric parameters, respectively. They are classified to [41, 50 – 51]:

– *Radiometric Parameters*: consists of the fluence ϕ (number of particle per surface unit), flux field $\dot{\phi}$ (number of particle per surface and time unit), and the intensity (number of particle per time units);

– *Dosimetry Parameters*: it consists of the absorbed dose (Gray) and KERMA. The absorbed dose describes the quantity of the transferred energy that is delivered by the charged particle to the matter by any type of ionizing radiation. Whilst the KERMA[2] describes the sum of the kinetic energy of charged particles that is originally produced by the interaction of non-charged particles e.g., photons or neutrons, per mass unit (kg).

1.4.2. Protection quantities

The International Commission of Radioprotection (ICRP) defined these quantities to predict the effects of ionizing radiation on individuals. Two kinds of protection quantities were determined as:

– *Equivalent Dose* or H_T (Sv): it is used to describe the biological effects when individuals are exposed to ionizing radiation. Moreover, it is related to the type (W_R) and the energy of the incident particle. It is calculated by multiplying the absorbed dose by the radiation factor (W_R);

– *Effective Dose*: it is defined to describe the sensibility of the organs (W_T), whereby $\sum W_T = 1$ for all organs, as well asofequivalent dose. In addition, the effective dose function is given as $W_R \times H_T$; the unit of efficacy dose is Sievert. Table 1.3 presents the radiological factors corresponding to energy and particle type, as the followings:

Table 1. 3: Radiological factors corresponding to energy and particle type [51 - 52].

Particle type	*Energy*	W_R
Photon, electron and muons	All Energies	1
Proton and Peon	All Energies	2
Alpha, Fission fragment	All Energies	20
Neutron	$\begin{cases} E_n \prec 1MeV \\ 1MeV \le E_n \le 50MeV \\ E_n \succ 50MeV \end{cases}$	$\begin{cases} 2.5+1.18e^{-\frac{\ln(E_n)^2}{6}} \\ 5+17e^{-\frac{\ln(2E_n)^2}{6}} \\ 2.5+3.25e^{-\frac{\ln(0.04E_n)^2}{6}} \end{cases}$

[2]Kinetic Energy Released in Material.

Table 1. 4: Tissue weighting factors (ICRP, 103) [52].

Organ	*Thyroid*	*Stomach*	*Skin*	*Colon*	*Lung*	*Rest of the body*
W_T	0.05	0.12	0.01	0.12	0.12	0.05

CHAPTER II: EFFICIENCY COMPUTATIONAL MODEL

This chapter summarizes the physics of gamma – rays for both point and voluminous sources using mathematical, experimental, and Monte Carlo methods.

It presents an accurate description of experimental and computational codes that aim to validate the geometrical model of the NaI(Tl) detector applied for large efficiency calculations. In addition, Appendix A. provides more details about the program running.

2.1. Introduction

The detection efficiency is one of the most key energetic characteristics for radiation measurement. It covers a large number of definitions including intrinsic, absolute, full energy peak, conversion, and multiplication efficiencies, etc. [42 – 43]. However, several methods aim to evaluate the detection efficiency either by mathematical formulas, Monte Carlo simulation, or semi – empirical methods. In the Monte Carlo codes, the detection efficiency is defined by the ratio of the number of recorded particles $\left(s^{-1}\right)$ to the number of emitted photons at $\left(4\pi\right)$ a solid angle $\left(s^{-1}\right)$. It can be calculated using the following equation:

$$\varepsilon(E)=\frac{N_{\det}}{N_{emi}} \tag{2.1}$$

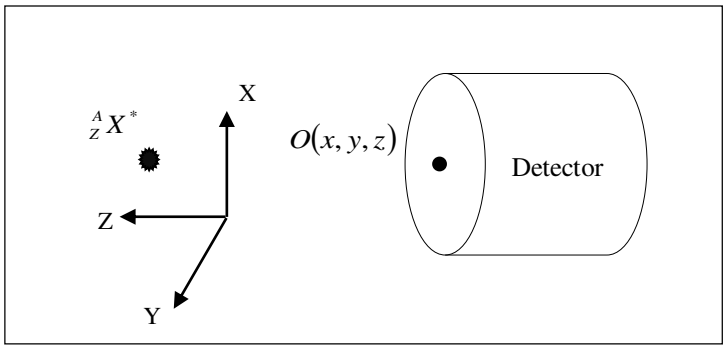

Figure 2. 1: Representation of point efficiency measurement.

Experimental measurements require functioning: the net photo – peak area $\left(r\right)$ which represents the recorded counts' rate minus background noise at their corresponding energy; the activity of standard sources $\left(A\right)$ in Bq ; the emission probability decay corresponding to each gamma – ray; and the spectroscopy time per second. The general expression used for the efficiency of the detector of isotropic source radiations with emission at a solid angle Ω [42]:

$$\varepsilon(E)=\frac{r}{F(E).A.\Omega.I_{\gamma}(\%)} \tag{2.2}$$

Where: $\left(r\right)$ is the number of recorded counts in s^{-1}; $\left(A\right)$ is source emitting particles per second; $F(E)$ is corrections factors added to efficiency formula. Concerning large sources (not point), it is necessary to underline the effects of the density and geometrical shape i.e., including $F(E)$ factors.

The detection efficiency of any spectrometric system depends on the geometrical characteristics (length, diameter, large, solid angle), the density of the sensitive part of the detector, the type, and the energy of the incident radiations [42, 55 – 57]. The next sections describe three different methods for efficiency measurement. It should be noted that all interactions of gamma radiations can occur inside the detector crystal. Then, the method used in this work for the calculation of environmental gamma spectrometry is described. The following brief introduction is addressed for experimental practitioners, Monte Carlo manipulators, and theoretical readers where the efficiency measurements are briefly explained.

2.2. Detection efficiency measurement

2.2.1. Mathematical model

Previous studies indicated that there are different analytical expressions, or/and approaches aimed to calculate the photo – peak efficiency for a point or extended sources, considering the source and the detector configuration. Numerous mathematical models and statistical equations were adapted to obtain the solution of particle transport in various geometry configurations as well as a special situation. To summarize, Irfan & Prasad (1970) [72] developed a model for efficiency calculation using mathematical expression.Their model was applied for isotropic coaxial radiating point sources. However, Gehreck (1990) [58] presented another mathematical formula that was limited for the asymmetrical source-detector position. Later, Gauss – Legendre (1994) [59] contributed to a semi – empirical and integral method for an application in large sample sources. Furthermore, this method was used to calculate spatial efficiency as a function of energy and coordinates. It includes the linear attenuation coefficient and the virtual center of the detector in the integral formula.

Later, Salim & Abbas (1995; 2002; 2006) [73, 61 – 62] and Abbas (2001; 2007) [60, 64] provided other detailed approaches for different detector – source configurations using more simplified mathematical expressions. Additionally, many other approaches consisted of the combination of the average length path inside the active volume of the detector, solid angle [63], and the coincidence effect for extended source [64]. Moreover, other researchers added correction factors such as self – absorption (S_f) [65] and the coincidence summing effect correction factors (CSF) [66] for the equation of efficiency measurement in bulk samples.These mathematical equations were validated either experimentally and/or in simulation data [67].

The present work studied the mathematical model using Gauss – Legendre integration. It can be experimentally calculates the spatial efficiency of the punctual source $\varepsilon_{ps}(x, y, z, E)$ at each (x, y, z) position and the linear attenuation coefficient $\mu(E)$ using multi – rays point source e.g.,^{152}Eu. Otherwise, these experimental quantities could be compensated with values resulted from a validated Monte Carlo model. The results of the linear attenuation coefficient and the values of the virtual center of the detector should be included in the Chebyshev transformation [75]. This latter is a transition from integral calculation to sum discrete domain. the efficiency of large sample volume (V) can be expressed as:

$$\varepsilon_{Vs}(E,V,z) \approx \frac{\alpha}{V}\left(\frac{\pi}{n+1}\right)\sum_{k=0}^{n}\frac{\sqrt{1-z_k^2}\left(e^{-\mu(E)\lambda(x,y,\alpha z+\beta)}\right)}{x_0^2+y_0^2+\left(\alpha z+\beta-Z_c(E)\right)^2} \tag{2.3}$$

Appendix (A) presents the algorithm in the MATLAB program implemented for the efficiency calculation of large samples using equation (2.3). This algorithm allows the efficiencies measurements considering the self – absorption factors, dimensional geometry, and experimental values of the virtual center of the detector $Z_c(E)$.

2.2.2. Experimental method

For large detection efficiency, the experiment requires the utilization of the same radionuclides regularly distributed in reference material whereby the experimental conditions e.g., size, density, effective atomic number, etc., should be preserved. It is necessary to ensure the homogeneous distribution of the radioelement on the sample [68]. These types of measurements imposed the correction of the self – absorption and/or summing effect phenomena.

2.2.3. Monte Carlo model

One of the most important characteristics of the Monte Carlo method is the effectiveness of efficient tools for tracking particles through complex geometries using computational computers. In comparison to the mathematical models, the physical problem might be particularly solved for the complex interactions. In recent years, the Monte Carlo simulation has become the most widely and suitable method for particle transport. The user of Monte Carlo should be aware during the process of entering data input description of the physical problem to avoid false physical results. The objective of the simulation is to construct an equivalent experimental setup i.e., source and detector for avoiding and/or reducing the complexity of the laboratory measurement. In terms of implication, the user

must involve the cross – sections, particle characteristics (configuration, energy, type, etc), and the detector configuration. The simulation results can accurately succeed after the validation of the constructed model. The following Monte Carlo codes are presented as powerful computational software for radiation detection, nuclear sites, radiological protection, shielding, and several other applications, e.g., MCNP [69], FLUKA [74], Geant (firstly developed at CERN in 1974), Geant4 [70] toolkits, PENELOPE [76], etc.

It should be noted that the reliability of the different methods must be experimentally verified. Figure 2.2 presents the history of the incident particle from starting to the end of the particle at the detection. Appendix (A) presents more details on cross – section definition in Monte Carlo language, mechanism of interactions, and some examples of Monte Carlo codes for calculations of detection efficiency.

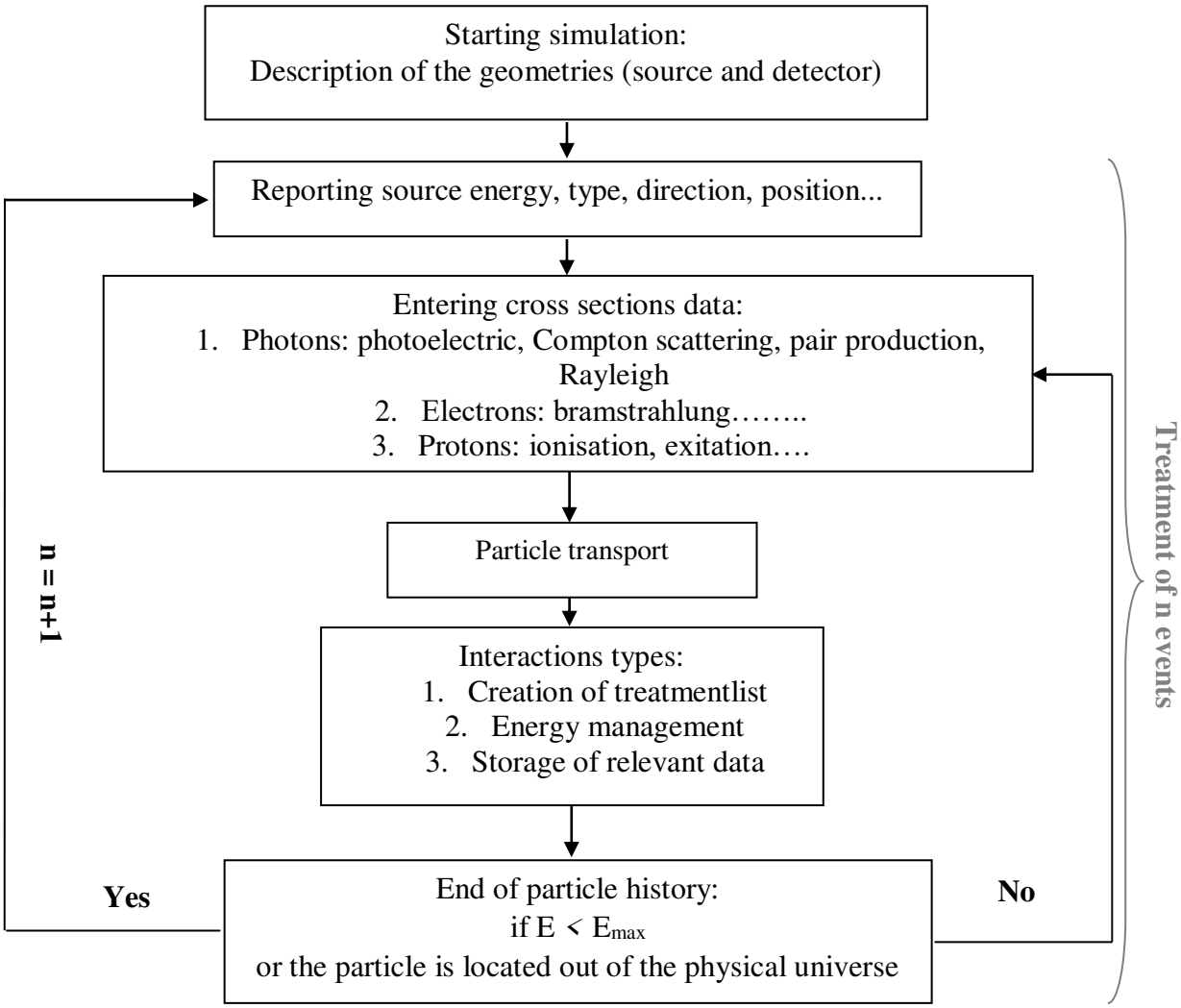

Figure 2. 2: Schematic diagram showing the simulation process in Monte Carlo codes. See, for example: [70].

This work focuses on two types of Monte Carlo codes for efficiency calculation: MC_Gamma and Geant4 toolkit.

2.3. Materials and methods

This part aims to construct a validated geometrical model for detection efficiency measurements. For this latter, it used the simulation model of 3" × 3" scintillation spectrometer NaI(Tl) and the standard gamma source prepared in the laboratory. Since the constructed geometry is validated, its model can be used in the next chapters for efficiency measurement applied in large environmental samples (See, Chapter 4).

2.3.1. Detection equipment

The experimental setup for large efficiency calibration is shown in Figure 2.3. It consists of NaI(Tl) detector maintained in the vertical position and KCl sample deposed on the detector facade. The synthetic sample was used because of the emission of the gamma line at 1460.8 keV corresponding to the natural radioelement ^{40}K. It should be noted that the detection system must be energetically calibrated at the first phase using ^{137}Cs (662 keV) and ^{60}Co (1172 and 1332 keV) standard sources (See, Chapter 3 section 4.1) . To reduce the effect of the background radiation on experimental data, the detection system was surrounded by cylindrical lead shielding.

Figure 2. 3: Experimental setup used for KCl detection efficiency.

2.3.2. Efficiency calibration for large standard source

This study used a fine and dried powder of potassium chloride KCl i.e., salt substitute particle, potted in a 200 mL cylindrical polyethylene bottle(R = 4 cm; H = 12 cm)adapted

for gamma spectrometry measurement. The sample was directly put on the top of the detector providing a high solid angle value. Experimentally, it is favorable to keep the distance source – detector as minimum as possible. To achieve this purpose, an estimation of a 1.mm distance was kept. The KCl efficiency calibration was recorded for 24 hours. The gamma spectra were acquired by Gamma Vision (Version 7) software. The performance parameters of the detector crystal: GEB function and efficiency measurement are discussed below.

2.3.3. NaI(Tl) configuration

It consists of 3" × 3" NaI(Tl) spectrometer modeled according to the description of the manufacturer. The density of NaI(Tl) crystal, MgO powder, and the aluminum cover were 3.667, 2.0, and 2.7 $g.cm^{-3}$, respectively. The dimensions, element composites, and densities were briefly defined. The SiO_2, reflection part, and the PM tube are not modeled. Figure 2.4 presentsthe constructed NaI(Tl) model using Geant4 and MC_Gamma.

To validate the detector energetic response, the Gaussian Energy Broadening (GEB) is considered in the Geant4 (See, Chapter 3). Using Geant4, the output data file of the pulse height distribution will be normalized on the photoelectric peak by the source activity. To obtain the net value, the experimental data subtracted the radiation background. These two steps allowed us to validate the Gean4 code applied for a voluminous source. However, efficiency calculations in MC_Gamma code require the data entry of NaI and source geometry, number of histories, and batch number. The outputs of MC_Gamma should be the values of the efficiency at each selected energies.

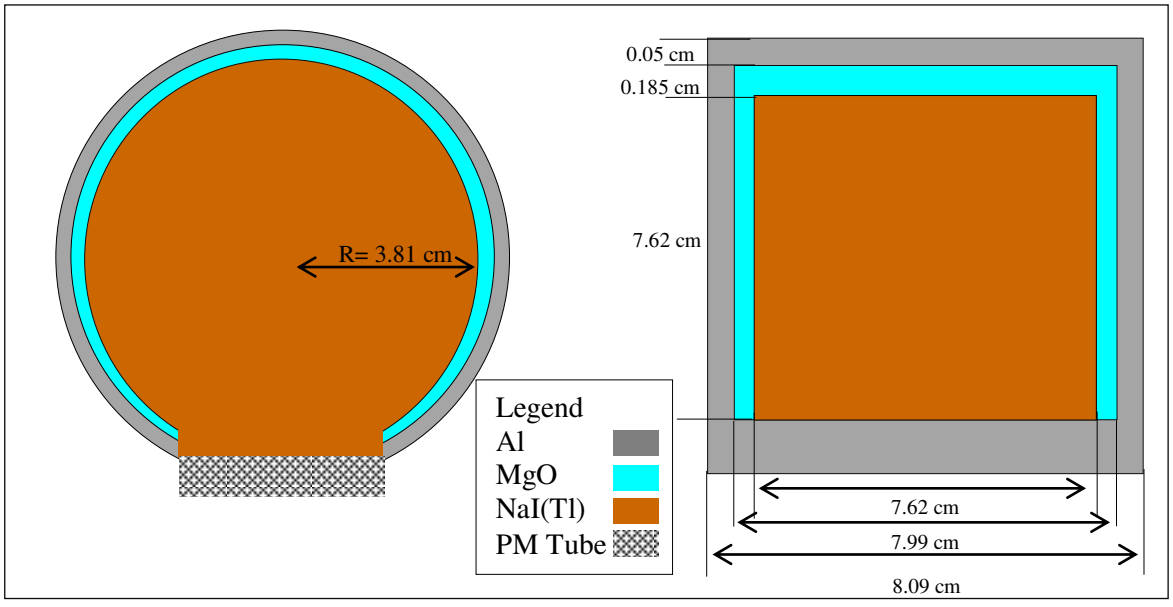

Figure 2. 4: Geometry of NaI(Tl) 3" × 3" scintillator detector.

2.4. Results and discussions

2.4.1. Validation of Geant4 model

Figure 2.5 indicates the simulated geometry with the Geant4 whereby the KCl sample was deposited on the detector top. It is produced using the Gnuplot program. It should be noted that the simulated geometry in Chapter 3 was re –used but this time for a large source.

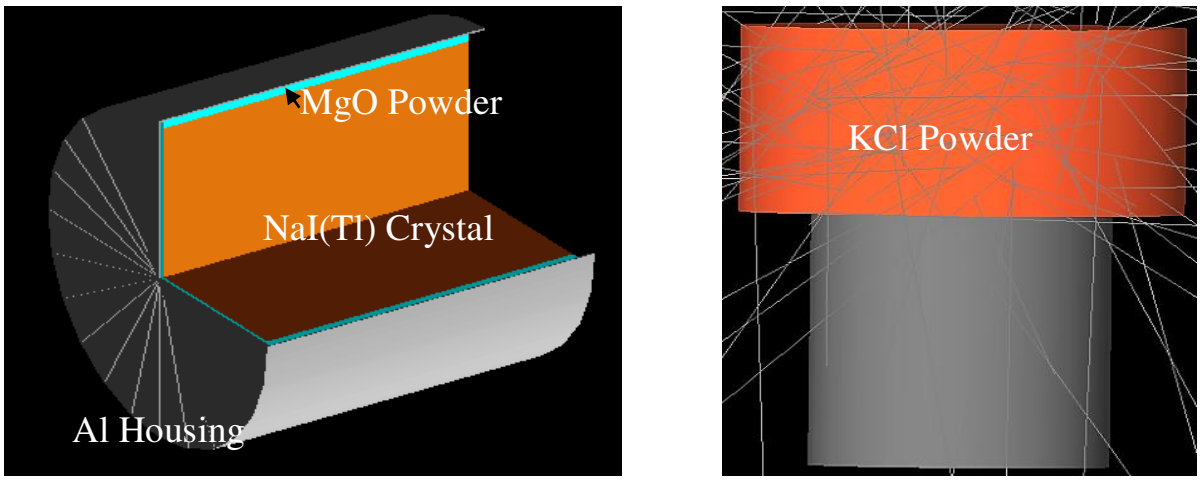

(a) (b)

Figure 2. 5: (a) Reproduced geometry structure of detection system, (b): simulation geometry: NaI(Tl) detector and KCl sample.

Figure 2.6 presents the experimental spectra issued for the KCl sample after 24 hours. Different energetic peaks can be observed. The origin of the selected peaks (from (a) to (h)) can be referred by:

- (a): photo –peak energy corresponds to 1460.8 keV;
- (b): Multiple diffusions of the incident photon at close θ angle;
- (c): Edge Compton (θ = π) corresponds to energy 1243 keV;
- (d): Single escape peak corresponds to 950 keV (1460.8 – 511);
- (e): Double escape peak corresponds to 438 keV (1460.8 – 2 × 511);
- (f): Retrodiffusion peak at 217.8 keV (1460. 8 – 1243);
- (g): Some peaks around 60 keV, corresponding to the photoelectric absorption in the materials immediately surrounding the detector and can lead to generation of a caracteristic X-ray that may reach the detector.

It can be explained by the energy degradation of incident photons according to several Compton diffusions.Using Origin Pro (2016) software, Figure 2.6 presents graphs of the comparison between Geant4 data and the experimental spectra counted for the KCl sample. It can be observed that there is a good agreement around the photo peak region, especially

between the measured and the simulated GEB function. However, some discrepancies at the low energetic range can also be observed. The obtained results indicated that the simulated Geant4 model can accurately simulate the transport of gamma particles for large sources.

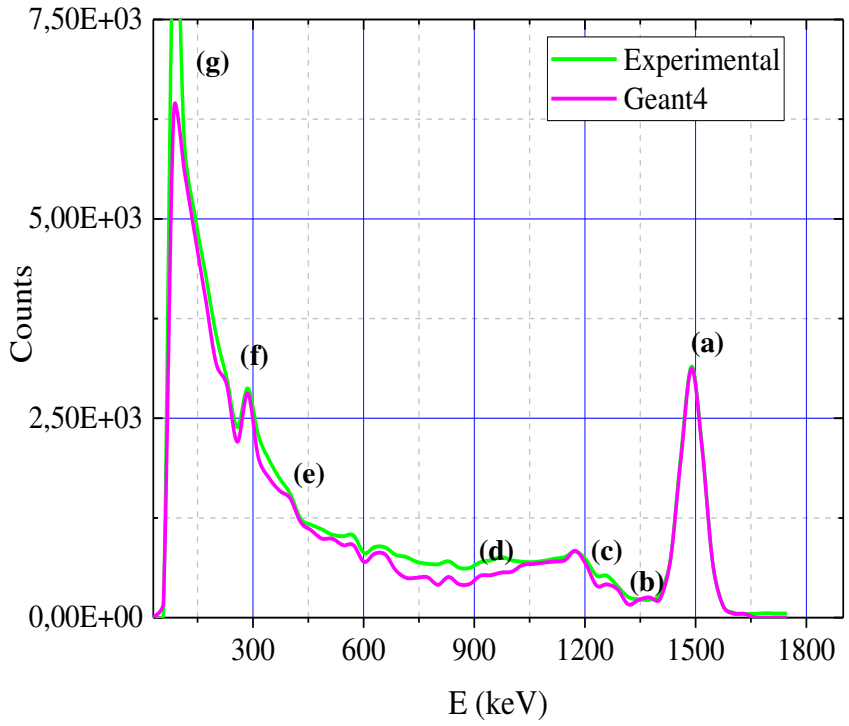

Figure 2. 6: Experimental and simulated spectra of KCl sample

2.4.2. MC_Gamma execution

Figure 2.7 summarizes a scheme of the steps of execution processes in the MC_Gamma program. Appendix (A) further details the MC_Gamma input data.

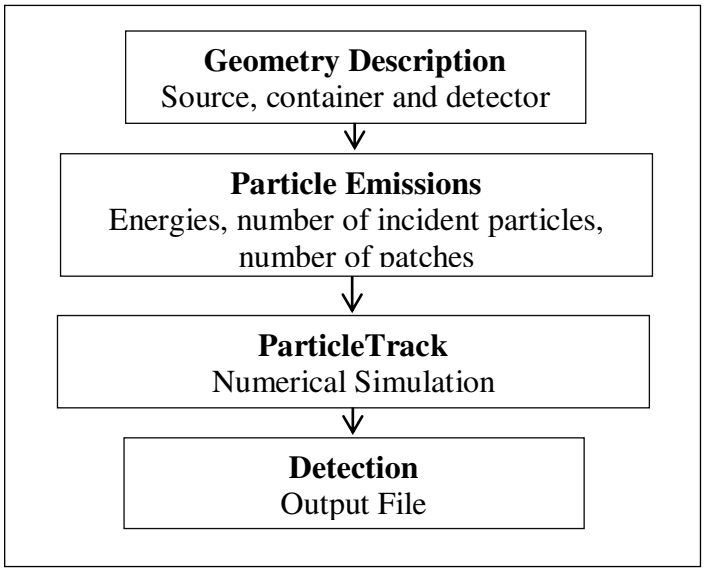

Figure 2. 7: Complete simulation steps in MC_Gamma language.

2.4.3. Comparing results: Geant4, MC_Gamma, and experimental data

Using whether Geant4 or MC_Gamma, the experimental validation of the Monte Carlo codes aimed to acquire reliable software for efficiency measurement. Typically, the experimental value of efficiency was calculated at 1.46 MeV using equation (2.2). This energy value is attributed to the disintegration of the natural element ^{40}K. Equation (2.2) considered the counting time, net area, sample weight, and source activity. Whereby, the source activity was calculated using equation (2.4):

$$A = \lambda N = \frac{\ln 2}{T_{1/2}} \frac{m}{M} N_a \tag{2.4}$$

Where: m is sample mass in (g); M is molar mass in $(g.mol^{-1})$; $T_{1/2}$ is half – life in (s); N_a is Avogadro's number. Table (2.1) illustrates the experimental value of the efficiency at 1.46 MeV of the KCl sample in comparison to the Geant4 and MC_Gamma software. It revealed an apparent agreement between Geant4, MC_Gamma, and the experiment.

Table 2. 1: Comparison of experimental and simulated efficiencies of KCl sample.

	Geant4	*MC_Gamma*	*Experiment*
$\varepsilon_{KCl}(1.46\,MeV)$	3.15 E–5 (%)	3.34 E–5 (%)	3.185 E–5 (%)

2.5. Conclusion

In radiation measurement, researchers are interested to obtain many analytical and/or non – analytical methods for detection efficiency calibration. Selecting the appropriate method is critical in achieving accurate results approximated to the experimental values. In this context, the simulation of Monte Carlo is considered fast and effective in measuring important physical values, especially when the geometry is complex and the particles are hard to track. Therefore, the current study used two programs of Monte Carlo simulation applied to gamma spectrometry. It aimed to supply to researchers a comparison of two techniques of the efficiency calibration Geant4 and MC_Gamma that might meet their analysis requirements. The selection of code is related to the user's needs whereby the used code will be adapted to suit the specific or non–habitual application.

This study results revealed that both programs indicate an impressive strong agreement of the simulated results in comparison to the experimental data. However, there

are some discrepancies in efficiency values that might be attributed to the non – simulated PMT and the inaccuracy of the GEB function. Hence, this calls for more optimization in the GEB function by reducing errors using more standard sources e.g., ^{152}Eu.

The next Chapter (4) will present the utilization of one of the validated codes for the efficiency measurement of environmental samples.

CHAPTER III: GAMMA SPECTRA UNFOLDING:

INVERSE MATRIX METHOD

This chapter attempts to solve the effect of poor resolution of sodium – iodine (Tl) scintillation detector for the quantification of interest radioactive elements found in gamma – spectrum. Therefore, it studies the unfolding of the gamma – rays counted by gamma spectrometer and response function construction. Accordingly, it proposes a GRAVEL computer code based on inverse matrix $R^{-1}(E, E_0)$ *calculation, response function* $R(E, E_0)$ *construction, and NaI(Tl) detector modeling. The first step test the unfolding process using standard radioactive source* ^{133}*Ba on 81 keV gamma peak whereby the matrix response function ranged from 20 to 110 keV. Appendix (A) provides a detailed description of GRAVEL execution.*

3.1. Introduction

Technically, the radiation unfolding idea is based on restoring the incident spectrum that already distorted by electronic noise and experimental data e.g., statistical fluctuations, scattered photons with detector periphery, recoil electrons, scattering peaks at small angles, background radiation, escape peaks, and especially the poor energetic resolution of the sodium iodide NaI(Tl) spectrometer. All these factors are unsuitable for peak searching, identifying, quantifying, and spectrum subsequent, especially if the spectral characterizing (net area) is very low.

The unfolding, or called deconvolution too, is recommended for collected complex spectra. It consists of presenting the spectral problem like matrixes convolution multiplications the following [42 − 43]:

$$\textit{Measured spectrum } Z(E) = \textit{Detector response function} \otimes \textit{Incident spectrum } \phi(E)$$

Where: the original spectrum is presented by a column vector $Z(E)$, the incident spectrum is presented by $\phi(E)$ a column vector, and the instrument response at each collected radiation of E_0 energy is described by the column of the response matrix $R(E, E_0)$. By which the physical solution, called the original spectrum, can be obtained by transforming the instrument matrix function $R(E, E_0)$ into a triangular format.

In this regard, many authors proposed several deconvolution techniques to solve the inverse problem. They suggested a stripping method where Compton continium is subtracted in descending order from each channel. Other suggestions for spectra unfolding used empirical methods, and/or iterative massive computer codes such as GRAVEL, MAXED, and FAZO, etc.The inverse problem revealed very good results especially for fast neutron spectra, calibration sources, and dose assessment, etc. The current study proposed an iteration algorithm (GRAVEL) applied for a collected gamma spectrum in few energetic channels.

3.2. Theoretical background

Let $\phi(E)$ is the registered gamma spectrum by γ detector (output signal), $Z(E)$ is the original spectrum emitted by a radioactive source (input signal), η is an electronic noise presented as an additional term δ ,and $R(E, E_0)$ is the ideal response function of the

detection system at different energy E_γ for emitting gamma – ray E_0 as shown in Figure 3.1.

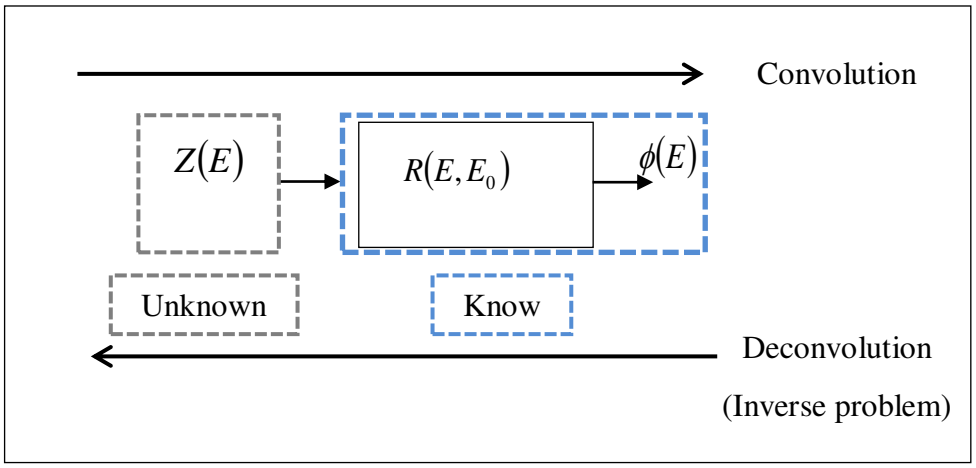

Figure 3. 1: Illustration of gamma spectra deconvolution.

Mathematically, $Z(E)$, $\phi(E)$, $R(E,E_0)$, and η could be related as a single integral expression, namely convolution product [99 – 100]. It can be expressed as:

$$\phi(E)=\int_0^\infty Z(E).R(E,E_0)dE+\eta \tag{3.1}$$

In linear algebra, equation (3.1) can also be expressed as the following matrix equation:

$$\begin{bmatrix}\phi_1\\ \phi_2\\ .\\ \phi_i\end{bmatrix}=\begin{bmatrix}R_{11} & . & . & . & R_{1j}\\ R_{21} & . & . & . & R_{2j}\\ . & . & . & . & .\\ R_{i1} & . & . & . & R_{ij}\end{bmatrix}\times\begin{bmatrix}Z_1\\ Z_2\\ \\ Z_i\end{bmatrix}+\begin{bmatrix}\eta_1\\ \eta_2\\ \\ \eta_i\end{bmatrix} \tag{3.2}$$

The results of random electrical signals, symbolized by η, generated by electronic devices can't be separately estimated from the detector response matrix. Consequently, equation (3.2) can be modified as the following:

$$\begin{bmatrix}\phi_1\\ \phi_2\\ .\\ \phi_i\end{bmatrix}=\begin{bmatrix}R_{11} & . & . & . & R_{1j}\\ R_{21} & . & . & . & R_{2j}\\ . & . & . & . & .\\ R_{i1} & . & . & . & R_{ij}\end{bmatrix}\times\begin{bmatrix}Z_1\\ Z_2\\ \\ Z_i\end{bmatrix} \tag{3.3}$$

Each element of the response matrix represents the contribution of a sub – matrix response corresponding to E_0 photon energy. The R_{ij} value is related to the response at j channel for

i energy. Therefore, the inverse matrix $R^{-1}(E, E_0)$ and the measured spectrum $\phi(E)$ must be calculated for the unfolding process.

Practically, the matrix elements can't be calculated for different energetic points. This is due to the lack of monoenergetic point sources. Hence, it is highly recommended to use the Monte Carlo method as a solution for matrix construction. Once the $R(E, E_0)$ matrix is constructed, the inverse problem can be successfully done using the unfolding software [96 − 97]. As previously mentioned in the introduction, this study employed a modified version of SAND− II code (renamed GRAVEL) GRAVEL [94 − 95], where the inversing matrix process $R^{-1}(E, E_0)$ was made in RSPGW class.

3.3. Materials and methods

3.3.1. Gamma spectrometry chain

A gamma spectrometry system was used to collect the measured gamma spectra $\phi(E)$. The NaI (Tl) detector was maintained in a vertical position and rounded by a cylindrical shield in 5 cm thick and 60 cm height. The emitted spectrum was collected at 10 cm from the spectrometer façade. The specific characteristics of the NaI(Tl) detector as volume is already presented in Chapter 2 section 3.3. Figure 3.2 shows the experimental setup utilizing NaI(Tl) detector housed by lead shielding and multi − gamma emitted source ^{133}Ba.

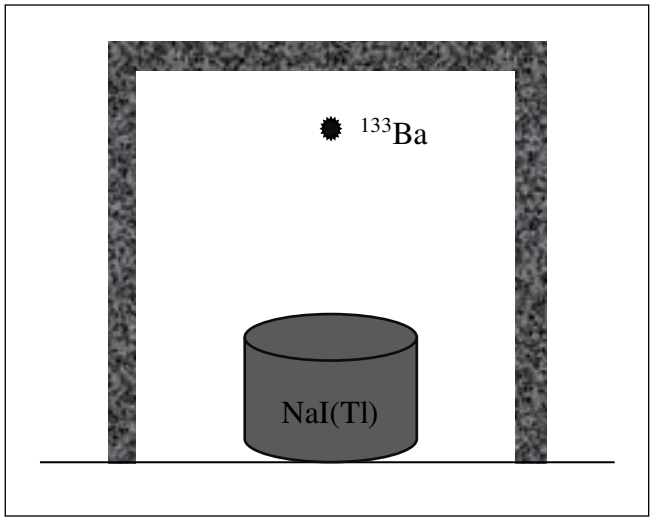

Figure 3. 2: Experimental setup for ^{133}Ba acquisition.

3.3.2. Detector modeling

A Geant4 of Monte Carlo code was employed to solve the problem of the matrix construction in several selected energy points. In this manner, the methodology initially consists of validating the mathematical model of the spectrometer by a punctual source.

Then, the adapted code will be able to simulate at any energy the response of this detector at each incident gamma particle.

For the experimental validation, the simulator should accurately define the dimensions and the compound of the simulated detector (See, Chapter 2). Also, it is obligatory to incorporate the Gaussian Energy Broadening function (GEB) in the input data files. In practice, two punctual sources (^{137}Cs and ^{60}Co) were used to establish the $FWHM$ and the resolution curves as an energy function. A simple formula of Gaussian energy is given as the following [42 − 43]:

$$f(E) = Ae^{-\left(\frac{2\sqrt{\ln 2}(E-E_0)}{FWHM}\right)^2} \tag{3.4}$$

A , E and E_0 are the normalization factors, broadened energy, and centroid energy of the tally, respectively. The $FWHM$ function is given as the following:

$$FWHM = a + b\sqrt{E + cE^2} \tag{3.5}$$

a , b , and c are the energetically constant coefficients provided from the least square fitting of equation (3.5).

3.3.3. Formation of response matrix using Geant4 code

To deconvolve the principal gamma of the ^{133}Ba window at 81 keV, the response function was simulated at a bin width of 1 keV along with the energetic range of 20 keV to 110 keV. For statistical calculation, Geant4 generated 10^6 events in each E_0 . The GEB energy function must be considered before starting the simulations. The user should take into account that the number of the simulation depends on the dimensions of the problem in the interested window, where a fixed bin width must be selected.

The energetic responses of each simulated energy, or sub − responses, should be then arranged in ascending order. This aimed to construct one input data file that presents the global window matrix [94].Chapter (4) presents an example of two response matrixes written in HEPROW format. It is previously mentioned that the single response function, $R(E, E_0)$ must be then transformed into an inverse single response function $R^{-1}(E, E_0)$ using RSPGW class from the HEPROW program [94].

3.3.4. GRAVELrunning

GRAVEL running should incorporate the following input files: the inverse response function and the net pulse height spectrum called multichannel file. This latter should first subtract the registered background level.

For the input pulse height files, UMSPHW will automatically perform the multichannel calibrations by introducing the bin width, channel number, number of escaped channels, number of the channel to be read, and the number of pulse in each channel. In addition, the resulted file will be written in HEPROW language. Furthermore, the user must select the convoluted zone (window), the distribution format, GEB function, iteration number, and interest gamma lines. It should be recalled that the analytical expressions for spectrum restoring and chi – square equation are integrated into the GRAVEL code (See, Appendix (A)). The resulted file is a deconvoluted pulse height spectrum as energy distribution.

3.4. Results and discussions

3.4.1. Validation of Geant4 model

The applicability test of the Geant4 model for the NaI(Tl) detector depends on the experimental validation by employing ^{137}Cs punctual source and 3" × 3" NaI(Tl) scintillator detector. Figure 3.3 provides a left view of the NaI(Tl) detector obtained by Geant4 code considering the compositional elements of the employed spectrometer, the distance of the ^{137}Cs source, and the gamma scintillator1 cm.

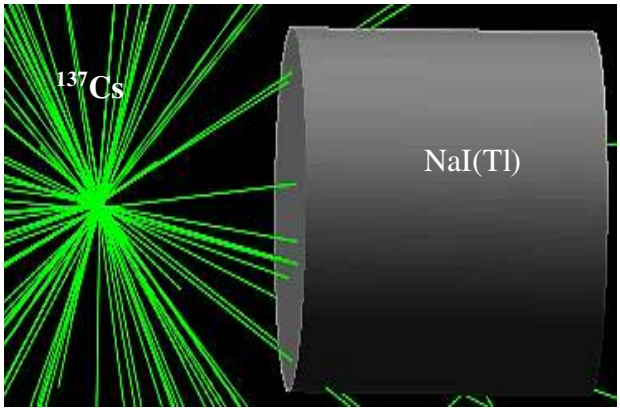

Figure 3. 3: 3D visualization of NaI(Tl) detector in Geant4 simulation.

In Figure 3.3, only the impacting elements have been used in the simulated model. Whereas, electrical connections and silicon dioxide (SiO_2) located on the back of the crystal are not described. However, the SiO_2 reflector intervenes just in the photons' reflection effects that

do not modify the total absorption peaks. Before the experimental validation of the simulated model, the MCA must be firstly calibrated to assure the linearity between the energy and the channels. Figure 3.4 shows that the MCA interface was calibrated using known checked sources (^{137}Cs and ^{60}Co). This was started from the first channel (142) containing the energy information to channel (276). Thus, energetic information was stored in 1022 channels and linearly fitted to know photo peaks for the yield of energy calibration.

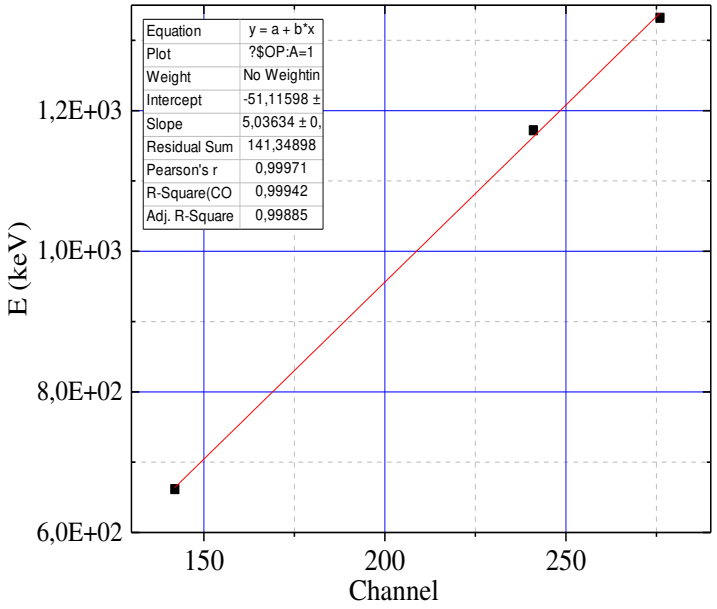

Figure 3. 4: Energy calibration using ^{137}Cs and ^{60}Co sources.

Nevertheless, the empirical values of $FWHM$ and the resolution of the NaI(Tl) detector are presented below. Figure 3.5 and Table 3.1 show that the adjustment parameters of the $FWHM$ are extrapolated through appropriate Power – law relation. The adjustment parameters (equation 3.5) are presented in the following table.

Table 3. 1: The adjustment parameters of FWHM.

$a(keV)$	$b(keV^{-1})$	$c(keV^{-1})$
-88.7888	8.57634	0.000558254

From figure 3.5, it can be observed that the energy resolution of the ^{137}Cs peak is estimated at 7.19 %. The values of other peaks are also reported corresponding to 1172 and 1332 keV. Moreover, it can be noticed that there is an inverse correlation between energy and the resolution; whereby more energy is increased, the more resolution will be accordingly decreased.

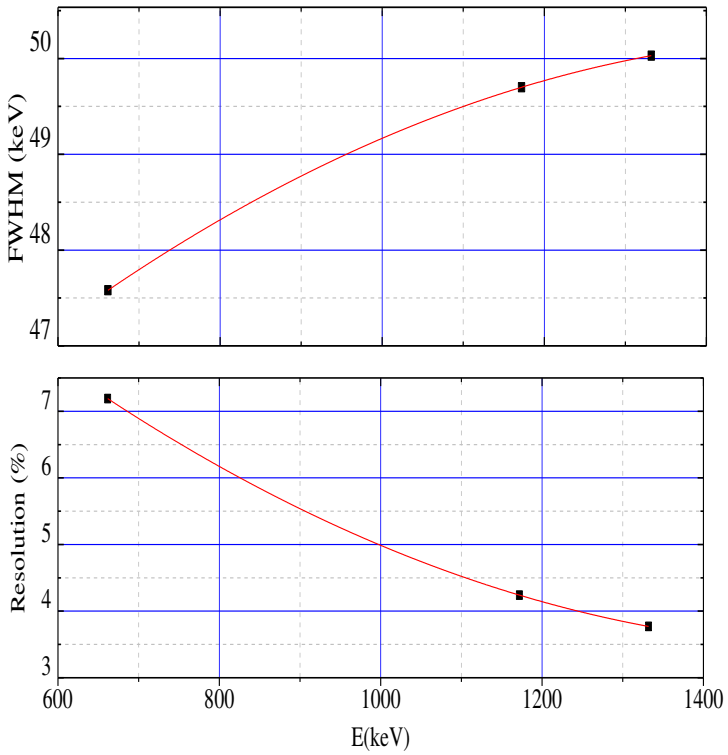

Figure 3. 5: FWHM and energy resolution (%) curves for NaI(Tl) detector.

Figure 3.6 illustrates the effect of the GEB function on the simulated gamma spectra.

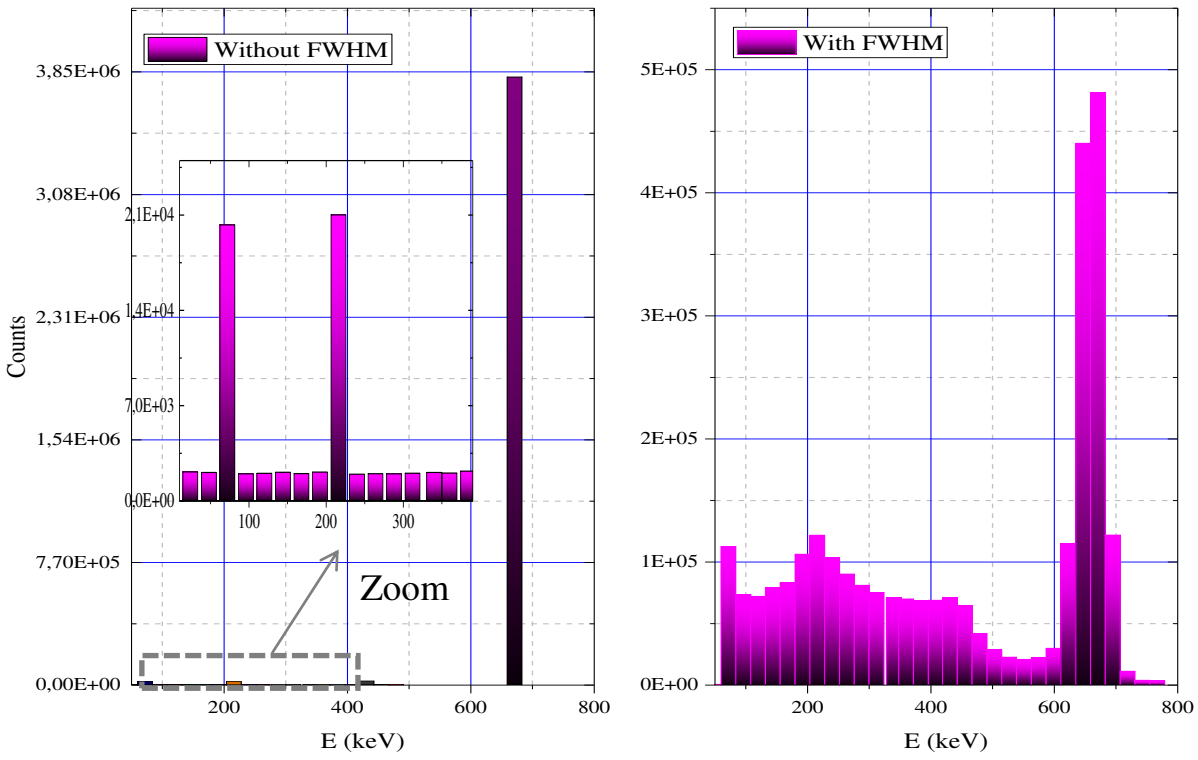

Figure 3. 6 : Effect of energy resolution in gamma spectra simulation by Geant4 code for cylindrical NaI(Tl) detector.

Figure 3.7 shows a comparison between the simulated spectrum with the experimental data. It is evident that there is good agreement amongst the spectrums, under the photo – peak region, but some incompatibility can also be observed.

The Compton background is less than the reference spectrum if the energy is lower than 300 keV. The difference may be attributed to the scattered photons in the closed cylindrical shielding system around the scintillator. The K–X ray peaks of the ^{137m}Ba source [96] and the effect of the photo– multiplicator tube are not considered in the Geant4 simulation.

In conclusion, a reliable Geant4 model can be efficiently used to simulate the response function of the NaI(Tl) spectrometer.

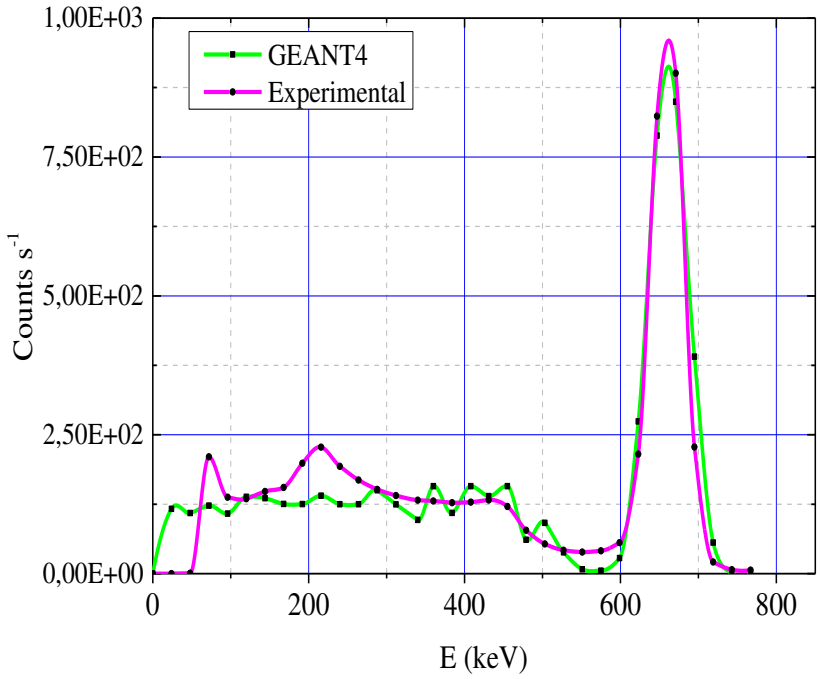

Figure 3. 7: Comparison between experimental and Geant4 results for ^{137}Cs source.

3.4.2. GRAVEL results

Figure 3.8 designs the plot of the unfolding signal obtained for the ^{133}Ba source and compared to the original spectrum. In this example, the background was not subtracted. It is observed that the *FWHM* of the deconvoluted spectrum is lower than the experimental data. From the same figure, the peak position was not changed after the unfolding process. In addition, some miscellaneous of semi – Gaussian peaks are observed.

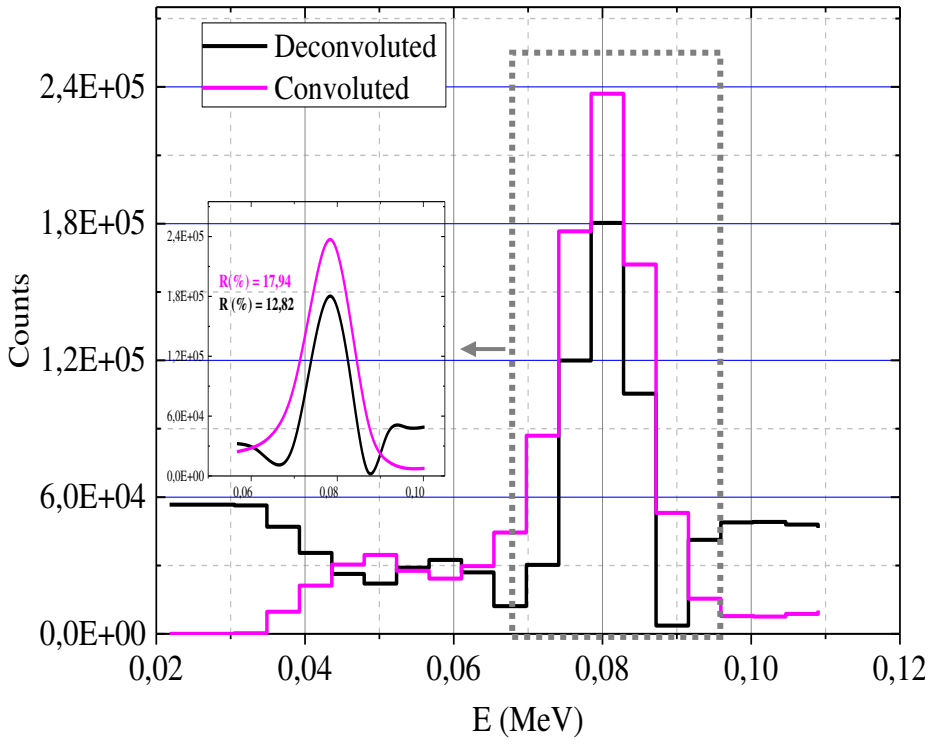

Figure 3. 8: Original spectrum and unfolded spectrum obtained by GRAVEL algorithm after 10000 iterations using ^{133}Ba source.

3.4.3. Validation of unfolding results

A direct comparison between deconvolving and certified activity is made to examine the deconvolution results with the experimental data.

Obviously, the estimated error of the deconvolution surface with the empirical data is approximately within 4 %. Subsequently, the unfolding code shows very good computability and efficiency for mother peak restoring. Also, the simulated NaI(Tl) model and GRAVEL algorithm are typically operational for the other deconvolution problem.

Table 3. 2: Real activity and deconvolved value for Barium radioactive source[3]

Isotope Activity	*Real value (kBq)*	*GRAVEL (kBq)*	*Relative error (%)*
^{133}Ba	29.2	28.0	4.11

3.5. Conclusion

This chapter presented a procedure for unfolding gamma spectra for γ-spectrometry measurement. Validation of the mathematical model of NaI(Tl) detector was made using

[3] The comparison was made after the subtraction of the natural background level.

^{137}Cs punctual source. The results have shown a better agreement with a statistical error of less than 5%.

The matrix response function of the scintillator counter is determined by Geant4 code. The unfolding method using the GRAVEL algorithm allows obtaining the arrived spectra to the detector. The difference between the calculated (GRAVEL) and the certified activity is less than 5 %.

CHAPTRE IV : ENVIRONMENTAL RADIOACTIVITY AND DOSIMETRY EVALUATION

Precise knowledge of gamma spectra distribution originally emitted from NORM's materials required a reconstruction of measured spectrum following the unfolding process. The natural radioactivity level in six different types of environmental samples used in Algeria had been investigated by gamma spectrometry chain. The analyzed materials were examined following the unfolding method employing GRAVEL code and Monte Carlo simulation for efficiency calibration. The radium equivalent activities, hazard indexes (external and internal), as well as absorbed and annual doses were estimated.

4.1. Introduction

This chapter selected six types of environmental samples including three geological samples (cement, gravel, and brick), two biological samples (wheat flour and milk powder), and a polyethylene sample (rubber). Moreover, it discussed the following phases of measurement:

- Phase I consisted of spectra collection $\phi(E)$, in which the laboratory measurement was carried out for six non-identical environmental samples;
- Phase II consisted of restoring the incident spectra $Z(E)$ using GRAVEL code;
- Phase III consisted of efficiency calibration using Monte Carlo code whether Geant4 or MC_Gamma;
- Finally, a radiological assessment was carried.

4.2. Materials and methods

4.2.1. Sample collection and conditioning

Solid random types of geological, biological, and polyethylene samples were collected from various locations of Blida and analyzed by gamma – ray spectrometry. The collected samples were kept in plastic bags, then brought to the Civil Engineering laboratory at the university of Blida1. They were crushed, dried in the ovens at 100^0C for 24 hours, and after that, ground using a grinder machine until they were transformed into powders. To achieve the homogeneity of samples, the powdered samples are sieved at 200 μm mesh, then stored in similar cylindrical polyethylene beakers (weighted for 200 g), correctly cataloged, and coded according to the type of sample. Before the estimation of the natural radionuclides, the prepared samples were stored for 28 days to achieve radioactive equilibrium between the radium and its progeny. Figure 4.1 shows the prepared samples used for gamma spectrometry measurement.

Figure 4. 1: Sample preparation and conditioning.

4.2.2. Gamma spectrometry chain: radioactivity measurement

All gamma spectrometry analysis were performed in the LPTHIRM laboratory at the university of Blida – 1. The concentration of the natural radionuclides ^{232}Th, ^{238}U, and ^{40}K were determined using a gamma spectrometry chain equipped with 3" × 3" ORTEC digiBase – RH SN 15014904 NaI(Tl) scintillator detector (See, Chapter (3)). To reduce the natural background level, the NaI(Tl) detector was placed vertically, and surrounded by the whole cylindrical lead with 5cm of thick, 50 cm in height, and 31 cm corresponding to the internal diameter of the shielding. For spectra acquisition, the detector was coupled to a computer with commercial GammaVision software (Version 7). The specific activity of ^{238}U, ^{232}Th, and ^{40}K was measured from the energy lines corresponding to gamma transitions: 1.76, 2.61, and 1.46 MeV, respectively. For quantitative analyses, the specific activity $\left(Bq.kg^{-1}\right)$ was calculated with equation (2.2).

4.3. Radiological hazard indices

4.3.1. Radium equivalent activity (Ra_{eq})

The common index should be used to compare the radiological effect of different materials containing ^{232}Th, ^{238}U, and ^{40}K, in one parameter called radium equivalent activity. This latter demonstrates the sum of weighted activities of the NORMs. It assumes that 1 $Bq.kg^{-1}$ of ^{226}Ra, 0.7 $Bq.kg^{-1}$ of ^{232}Th, and 13 $Bq.kg^{-1}$ of ^{40}K generates the same rate dose of emitted gamma radiation. Therefore, it can be written as the following equation [83 − 84]:

$$Ra_{eq} = A_{Ra} + 1.43A_{Th} + 1.43A_{K} \tag{4.1}$$

A_{Ra}, A_{Th} and, A_{K} are the activity concentration in dry weight $\left(Bq.kg^{-1}\right)$ of ^{238}U, ^{232}Th, and ^{40}K respectively. Whereby the maximum value of Ra_{eq} is recommended at 370 $Bq.kg^{-1}$ in the literature see, for example [83 − 84].

4.3.2. External and internal hazard index

In 1985, Mathew & Breketa defined two dosimetric indices called external $\left(H_{ex}\right)$ and internal $\left(H_{in}\right)$ hazard indexes to limit the radiation dose to an equivalent dose. They described the radiological and non – radiological hazards associated with the internal (digestion) and the external (by inhalation) exposure to radon (inert radioactive gas) and itsshort – life progeny.They can be calculated using the following equations [83 − 84] :

$$H_{ex} = \frac{A_{Ra}}{370} + \frac{A_{Th}}{259} + \frac{A_K}{4810} \leq 1 \tag{4.2}$$

$$H_{in} = \frac{A_{Ra}}{185} + \frac{A_{Th}}{259} + \frac{A_K}{4810} \leq 1 \tag{4.3}$$

It's assumed that 370, 259, and 4810 $Bq.kg^{-1}$ are emitted in the same gamma source.

4.3.3. Absorbed dose resulted from the external exposure of construction materials:

It describes the absorbed dose (D) in the air of 1 meter high on the ground attributed to the terrestrial gamma emitters. The global average value of absorbed dose rate is 55 $nGy.h^{-1}$ [85]. The absorbed dose is determined using the following equation (4.4):

$$D\left(nGy.h^{-1}\right) = 0.426A_{Ra} + 0.604A_{Th} + 0.0417A_K \leq 55 \tag{4.4}$$

4.3.4. Annual effective dose rate in construction materials

To estimate the health effect of exposure to natural radiation in one year, the annual effective dose rate (AED) is calculated by using the following formula:

$$E\left(mSv.y^{-1}\right) = D\left(nGy.h^{-1}\right) \times 8766\left(h.y^{-1}\right) \times 0.8 \times 0.7\left(Sv.Gy^{-1}\right) \times 10^{-6} \leq 1 \tag{4.5}$$

Where 0.7 $Sv.Gy^{-1}$ is the conversion coefficient from absorbed dose rate to an effective dose, 0.8 is the indoor occupancy factor proposed by UNSCEAR, and 8766 is the number of hours in one year. The worldwide average of annual affective dose rate is estimated to be 1 $mSv.y^{-1}$.

4.3.5. Threshold consumption rate ($kg.y^{-1}$)

The threshold consumption rate ($DI_{Threshold}$) represents the maximum amount consumption of swallowing a dose of food and beverages superior to 290 μSv per one year. This value is recommended by the UNSCEAR (2000a, 2000b, 2008) as an effective dose through the ingestion path. The $DI_{Threshold}$ was calculated according to the UNSCEAR formula:

$$DI_{Threshold}\left(kg.y^{-1}\right) = \frac{D_{average}\left(\mu Sv.y^{-1}\right)}{\sum_{k=1}^{3} D_{ingestion}\left(Sv.Bq^{-1}\right) \times A_i\left(Bq.kg^{-1}\right)} = \frac{290}{\sum_{k=1}^{3} D_{ingestion} \times A_i} \tag{4.6}$$

Where $D_{average}$ represents the threshold average annual committed effective dose due to the ingestion of NORMs via foodstuff (UNSCEAR, 2000a, b), A_i is the radionuclide activity concentration of each *i* radionuclides, and $D_{ingestion}$ is the ingestion conversion coefficients in $Sv.Bq^{-1}$ for each *i* radionuclides.

4.3.6. Yearly intake of natural radionuclides from the consumption food ($Bq.y^{-1}$)

This is used to describes the annual radioactivity level taken from the ingestion of the powdered milk and the powdered wheat[4], separately. It can be estimated by using equation (4.7) [91]:

$$Y_{\text{int}ake}\left(Bq.y^{-1}\right)=\frac{A_i \times F_c}{A_p} \tag{4.7}$$

Where $Y_{\text{int}ake}$ is the consumed radioactivity level in a year $\left(Bq.y^{-1}\right)$, A_i is the specific activity of "*i*" radionuclides (in $Bq.kg^{-1}$), F_c is the annual weight consumption of foodstuffs (kg), and A_P is the Algerian population.

Algerian office of statistics demonstrated that the population of Algeria was estimated at 43.85 million inhabitants in 2020 (ONS, https://www.ons.dz). According to the GAIN report, the American department of agriculture revealed that the annual consumption of wheat is approximately estimated at 10.6 MMT in 2019/2020. (USDA, 2019). This represents an individual annual consumption of 100 kg per inhabitant which is about double the individual consumption in the European Union and the triple of the rest of the world (https://www.alaraby.co.uk/economy/).

In 2018, the GAIN report indicated that wheat importation was 6.932685 MT which forms around 36.09 % of total imports in Algeria whereby the main foreign source is France with 4.376604 MT[5]. On the other hand, the annual consumption of milk in Algeria was estimated at 200.000 tonnes, where the universal amount determined the annual threshold consumption at 90 Litres per year.

It should be mentioned that the estimated values of the annual consumption rate for either milk or wheat may contain some uncertainty due to the number of consumers, wheat and/or milk allergy, and breastfeeding age…etc.

[4] The measurement is carried out forAlgerian statistics.
[5] MT: Million Tonne

Chapter 4 presents an application of the estimated values of Y_{intake} in committed effective dose measurement.

4.3.7. Effective committed dose in foodstuffs ($\mu Sv.y^{-1}$)

The committed effective dose is used to estimate the stochastic health effect on the human body due to the ingestion of radionuclides materials throughthe foods chains. Notably, the measured values do not represent the generic individual consumption dose, but it represents the committed dose of a person exposed under some consumption conditions. In this context, the following formula of Khandaker (2019) was adopted to estimate the committed effective dose, by:

$$D_{effective_i}\left(Sv.y^{-1}\right) = Y_{intake} \times D_{ingestion_i} \quad (4.8)$$

Where $D_{effetive}$ is the effective committed dose of *i* radioelement (in $Sv.y^{-1}$), and $D_{ingestion}$ is the ingestion dose coefficient of *i* radionuclide (in $Sv.kg^{-1}$). Table 4.1 presents the ICRP (2012) ingestion coefficient of dose factors.The total of $D_{effective}$ values is the sum of the $D_{effective_i}$ values.

Table 4. 1: Conversion factors (in) for ^{40}K, ^{238}U and ^{232}Th (See ICRP (1996)).

Age groupe	^{40}K	^{238}U	^{232}Th
Children (2-7 y)	2.1 × E–8	6.2 × E–7	3.5 × E–7
Children (7-12 y)	1.3 × E–8	8.0 × E–7	2.9 × E–7
Children (12-17 y)	7.6 × E–9	1.5 ×E–6	2.5 × E–7
Adults (>17 y)	6.2 × E–9	2.8 × E–7	2.3 × E–7

4.4. Results and discussions

4.4.1. Experimental spectrum emitted from natural radionuclides: deconvolution of ^{40}K and ^{238}U regions

This section uses the unfolding code GRAVEL to restore the original γ – distributions $Z(E)$ issued from environmental samples, which were already counted by NaI(Tl) 3" × 3" spectrometer. The interest regions will be deconvoluted selecting the photo – electric peaks of ^{40}K and ^{214}Bi (daughter of ^{238}U) at 1.46 and 1.76MeV, respectively, and following the same unfolding methodology that was already applied and validated by the calibration

source (See, Chapter (3)). As mentioned in Chapter (3), the dimensions of the response function depend on the energy borders of experimental spectra $(-3\sigma,+3\sigma)$. The instrument response function at the selected energies 1.46 and 1.76 MeV should be constructed using the validated spectrometer model used in Chapters (2) and (3). Table 4.2 summarizes the interest energetic regions of ^{214}Bi and ^{40}K. The given data windows consisted of two – response energetic functions.

Table 4. 2: Energetic windows of the relevant natural radioactive elements: ^{40}K and ^{238}U[6].

Radioelement	*Centroid peak energy (keV)*	*Energetic window (keV)*	*I_γ (%)*
^{40}K	1460.8	189	10.66
^{214}Bi	1764.5	145	15.28

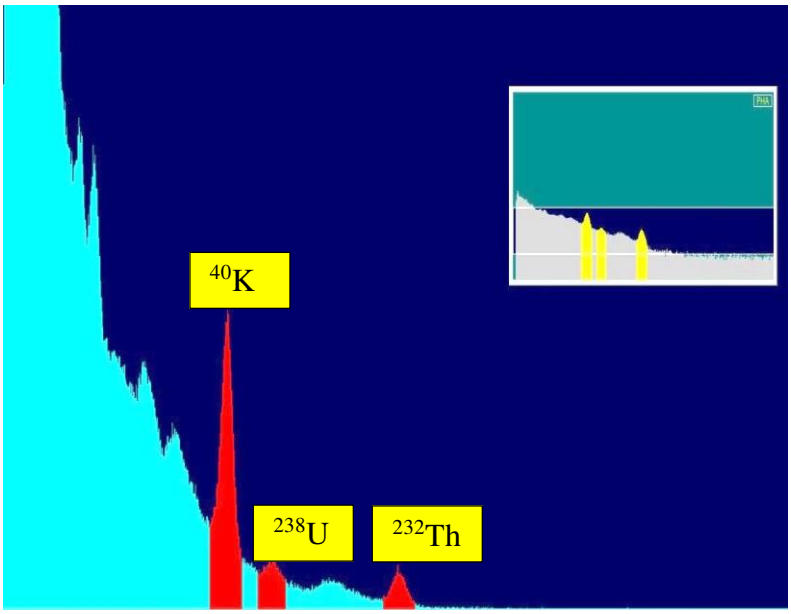

Figure 4. 2: Selection of interest ROIs regions showing by GammaVision software.

The recorded countsand the background radiation levelmust be firstly transformed in the HEPROW language[7] and saved as UMS_MES.PHS and UMS_INU.PHS, respectively (See Figure 4.3). Then, the recorded counts subtracted the background level to get the net counts $\phi(E)$ that also saved as OPR_1.PHS. Figure 4.2 represents an example of the gamma pulse height distribution issued from the cement sample. Figure 4.4 represents the interest region ROIs that will be used for spectra unfolding. It should be mentioned that the ^{232}Th concentration was directly calculated using a 2.61MeV gamma line. This is because that

[6] The bin width of the simulated matrixes at 1.46 and 1.76 MeV was fixed at 1 keV.
[7]More details for input data file can be found in Chapter (3)

^{232}Th is not affected by the first, second escape peaks, and Compton diffusions, in addition to the fact that is far from these diffusion radiation factors as illustrated below.

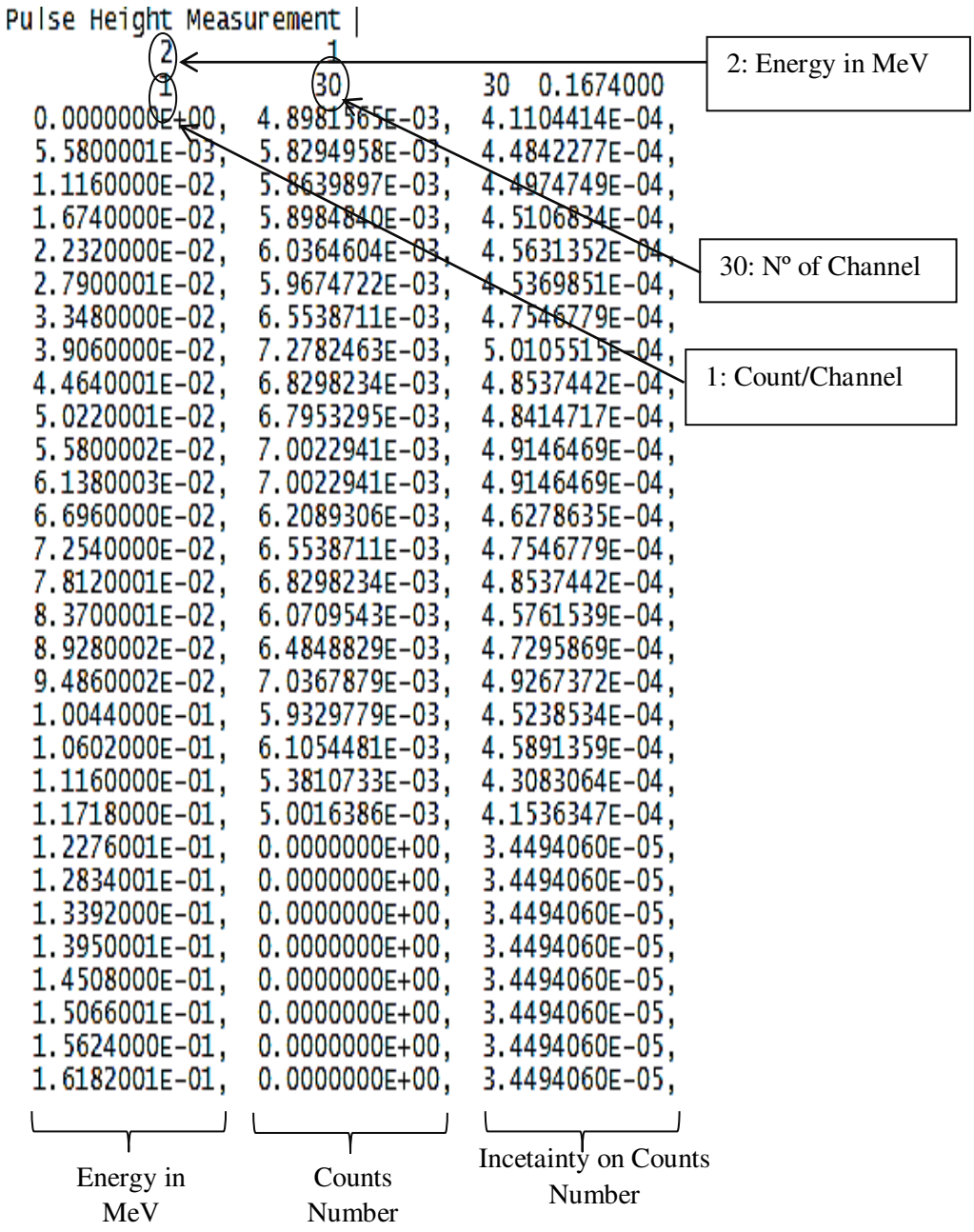

Figure 4. 3: Example of pulse height spectrum in HEPROW format.

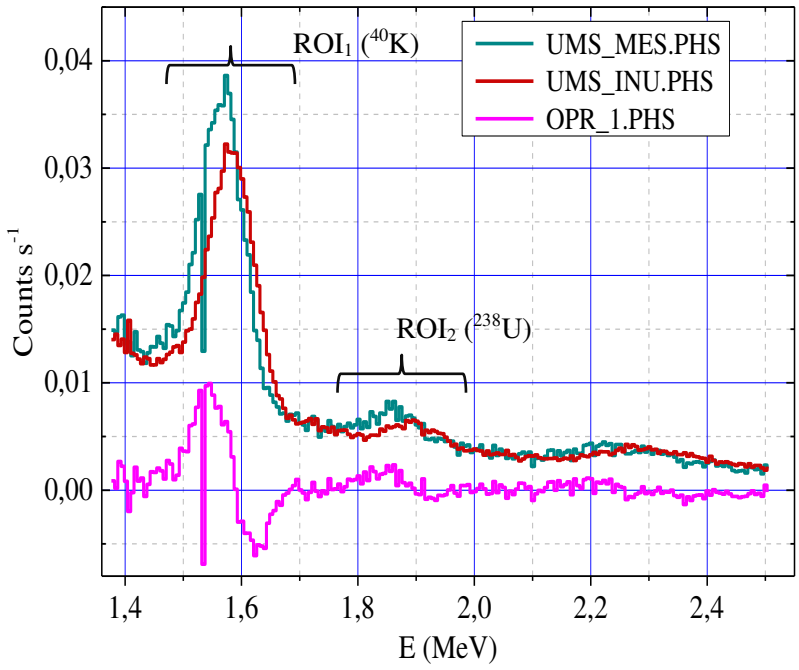

Figure 4. 4: Selected range chosen for gamma spectra unfolding in cement sample for ^{238}U at 1764.5 keV and ^{40}K at 1460.8 keV.

Secondly, the detector response function at the ROIs must be constructed following the provided data in Table 4.2. Figure 4.5 presents an example of the energetical response $R(E, E_0)$ of NaI(Tl) detector measured by Geant4 code and ranged from 1 MeV to 1.7 MeV

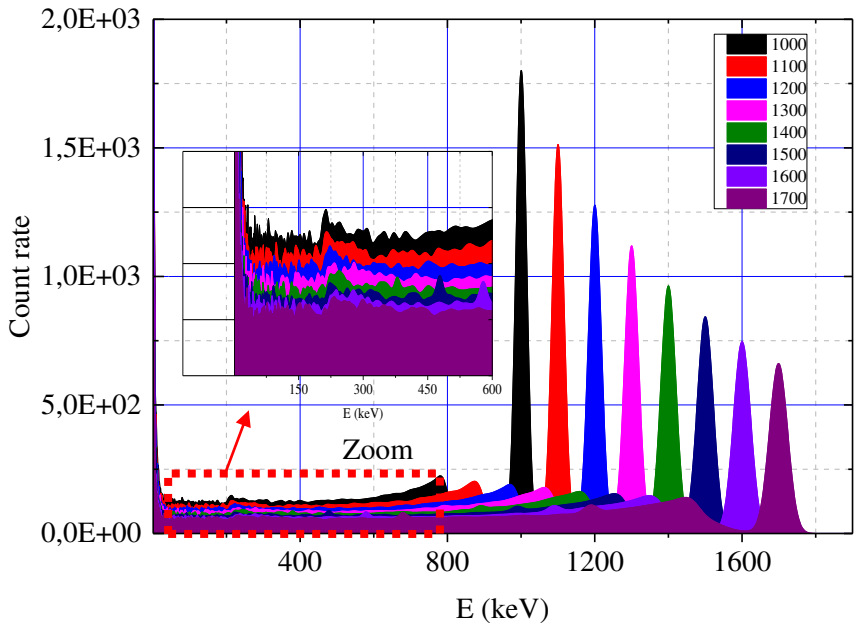

Figure 4. 5: Convolution process in scintillator detector, the total response function matrix represents how the detector will respond to different incident gamma energies from 1 MeV to 1.7 MeV.

```
 2.00000E-02   130  0.00000E+00  1.29987E-01
3.4483E+05 2.9132E+04 3.0360E+04 3.1513E+04 3.2578E+04 3.3543E+04 3.4398E+04
3.5133E+04 3.5740E+04 3.6210E+04 3.6540E+04 3.6724E+04 3.6760E+04 3.6649E+04
3.6391E+04 3.5990E+04 3.5450E+04 3.4777E+04 3.3981E+04 3.3069E+04 3.2052E+04
3.0942E+04 2.9750E+04 2.8489E+04 2.7172E+04 2.5812E+04 2.4421E+04 2.3012E+04
2.1598E+04 2.0189E+04 1.8796E+04 1.7429E+04 1.6096E+04 1.4806E+04 1.3564E+04
1.2377E+04 1.1248E+04 1.0181E+04 9.1786E+03 8.2414E+03 7.3702E+03 6.5647E+03
5.8237E+03 5.1456E+03 4.5282E+03 3.9689E+03 3.4648E+03 3.0125E+03 2.6088E+03
2.2501E+03 1.9329E+03 1.6538E+03 1.4093E+03 1.1961E+03 1.0111E+03 8.5132E+02
7.1390E+02 5.9625E+02 4.9600E+02 4.1095E+02 3.3911E+02 2.7871E+02 2.2815E+02
1.8602E+02 1.5105E+02 1.2217E+02 9.8413E+01 7.8958E+01 6.3095E+01 5.0217E+01
3.9807E+01 3.1429E+01 2.4714E+01 1.9357E+01 1.5099E+01 1.1731E+01 9.0781E+00
6.9968E+00 5.3710E+00 4.1065E+00 3.1271E+00 2.3717E+00 1.7916E+00 1.3480E+00
1.0101E+00 7.5391E-01 5.6043E-01 4.1494E-01 3.0599E-01 2.2474E-01 1.6440E-01
1.1978E-01 8.6923E-02 6.2825E-02 4.5226E-02 3.2426E-02 2.3156E-02 1.6470E-02
1.1667E-02 8.2319E-03 5.7848E-03 4.0489E-03 2.8225E-03 1.9597E-03 1.3552E-03
9.3344E-04 6.4034E-04 4.3752E-04 2.9774E-04 2.0180E-04 1.3623E-04 9.1594E-05
6.1334E-05 4.0900E-05 2.7153E-05 1.7935E-05 1.1771E-05 7.6565E-06 4.9150E-06
3.2034E-06 2.0104E-06 1.2278E-06 7.2265E-07 4.0551E-07 2.1447E-07 1.0559E-07
4.7662E-08 1.9267E-08 6.6377E-09 1.6559E-09

 2.10000E-02   131  0.00000E+00  1.30987E-01
4.0472E+05 3.3441E+04 3.4775E+04 3.6018E+04 3.7155E+04 3.8175E+04 3.9066E+04
3.9817E+04 4.0419E+04 4.0867E+04 4.1153E+04 4.1276E+04 4.1233E+04 4.1025E+04
4.0655E+04 4.0126E+04 3.9446E+04 3.8622E+04 3.7663E+04 3.6582E+04 3.5389E+04
3.4098E+04 3.2722E+04 3.1276E+04 2.9774E+04 2.8231E+04 2.6661E+04 2.5078E+04
2.3494E+04 2.1922E+04 2.0373E+04 1.8858E+04 1.7386E+04 1.5964E+04 1.4601E+04
1.3300E+04 1.2066E+04 1.0904E+04 9.8137E+03 8.7973E+03 7.8546E+03 6.9849E+03
6.1867E+03 5.4577E+03 4.7955E+03 4.1967E+03 3.6580E+03 3.1758E+03 2.7461E+03
2.3650E+03 2.0287E+03 1.7333E+03 1.4749E+03 1.2501E+03 1.0553E+03 8.8730E+02
7.4306E+02 6.1979E+02 5.1491E+02 4.2606E+02 3.5114E+02 2.8824E+02 2.3566E+02
1.9190E+02 1.5565E+02 1.2574E+02 1.0117E+02 8.1079E+01 6.4718E+01 5.1452E+01
4.0742E+01 3.2133E+01 2.5242E+01 1.9750E+01 1.5391E+01 1.1946E+01 9.2355E+00
7.1114E+00 5.4540E+00 4.1662E+00 3.1698E+00 2.4021E+00 1.8131E+00 1.3630E+00
1.0206E+00 7.6116E-01 5.6540E-01 4.1832E-01 3.0827E-01 2.2626E-01 1.6541E-01
1.2044E-01 8.7348E-02 6.3095E-02 4.5395E-02 3.2531E-02 2.3219E-02 1.6506E-02
1.1688E-02 8.2428E-03 5.7901E-03 4.0510E-03 2.8230E-03 1.9594E-03 1.3546E-03
9.3271E-04 6.3967E-04 4.3695E-04 2.9729E-04 2.0146E-04 1.3598E-04 9.1409E-05
6.1198E-05 4.0799E-05 2.7073E-05 1.7867E-05 1.1709E-05 7.5978E-06 4.8613E-06
3.1696E-06 1.9819E-06 1.2064E-06 7.0897E-07 3.9875E-07 2.1272E-07 1.0666E-07
4.9769E-08 2.1336E-08 8.2267E-09 2.7196E-09 6.5585E-10
```

Response function for 20 keV

Response function for 21 keV

etc…

Figure 4. 6: Example of photon response matrix for 20 and 21 keV, counted for NaI(Tl) detector and translated in HEPROW format[8].

Figure 4.6 represents an example of the sub – response functions transformed in HEPROW format. From the represented matrix, the following information can be explained as:

– ***The first record*** corresponds to the bin width (EKA);

– ***The second record*** attributed to the energy of incident photon (E_0 = *2.0000E– 02 MeV*), number of channels of the response function (for E_0 *=2.0000E– 02 MeV , number of channels =130*), the left boundary correspond to (*E(1)=0.0000E+0*), and the right boundary correspond to (*1.29987E–01 MeV*);

– ***n record*** corresponds to E_n energy, i.e., new values for E_n, channel number, left boundary always *E(1) =0*, and the new value of right boundary.

For the deconvolution process, two separate input data files corresponding to the resulted file (OPR_1.INP) and the inverse response function (ORIGINAL.RSP) must be used.

[8] It was suitable to present tow consecutive response matrix of ^{40}K or ^{238}U, but the huge size of the sub – matrix avoid use from the presentation.

To assure the convergence of the unfolding results regardless of the experimental data, the significance level (a) of χ^2 should be considered as well. The execution has been performed for an equal 10000 iteration number to get a value of χ^2 significance level as lower as possible (See, HEPROW).

The present work presented a deconvolution of 12 different ROIs windows provided from geological (cement, brick, gravel), biological (milk and wheat), and polyethylene sample (rubber), therefore, the incident gamma spectra were restored. The results of unfolding for the environmental sample were presented in the next figures. It should be noted that the key **"**Deconvoluted**"** is the calculated surface obtained after the deconvolution procedure, and the "Convoluted" is the measured surface provided from experimental data. In the same Figures, the GRAVEL results and experimental pulse height are presented for the 3" × 3" NaI(Tl) detector. The deconvolution results indicated that the GRAVEL code allowed obtaining the expected results. In case of negative values in OPR_1.PHS, i.e., the background level is higher than the measured pulse height, the output of unfolding is always positive. It can be noticed that the form of the deconvoluted spectrum depends on the measured spectrum form $\phi(E)$. In other words, measures are more reliable if the counts' number as higher as possible providing significant statistical results. Consequently, the spectrometry analysis should be enhanced by the unfolding process especially for poor resolution detector and complex spectrum. Hence, the peak searching, i.e., qualitative analysis, and net peak area calculation, i.e., quantitative analysis, should become easier and faster.

To investigate the effect of deconvolution per measured spectrums, Table 4.3 represents the difference between the measured data and the reconstructed default spectra.

Table 4. 3:Values of the ratio between measured and deconvolved gamma spectra for ^{40}K and ^{238}U.

	Difference (Experimental\GRAVEL)	
	^{40}K (1.46 MeV)	*^{238}U (1.76 MeV)*
Wheat	66 E–1 ± 8 E–1	57 E–1 ± 3 E–2
Milk	34 E–1 ± 2 E–2	09 E–1 ± 1 E–4
Cement	14 E–1 ± 8 E–2	10 E–1 ± 1 E–4
Brick	17 E–1 ± 8 E–2	03 E–1 ± 8 E–4
Rubber	11 E–1 ± 5 E–2	11 E–1 ±12 E–3
Gravel	BDL	49 E–2 ± 8 E–5

According to the obtained results in Table4.3, it can be observed a significant decrease due to the removal of all distortions noises.

For ^{40}K energetic peaks, there are more recorded events due to the scattering of high energetic peaks inside the sample, scattered photons in the surrounded lead, single, and double – escape peaks. Moreover, an elevation of radiation level in ^{40}K can be clearly observed in comparison to the ^{238}U. This can be recorded for each used material whatever wheat, milk, cement, or brick. From the other side, Figure 4.7 presents the hypothesis of the scattered photons (with blue color) in the inner wall of lead.

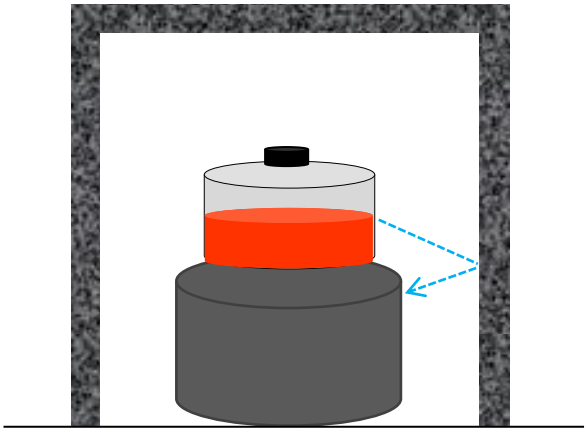

Figure 4. 7: Track of scattered photons in lead shielding wall.

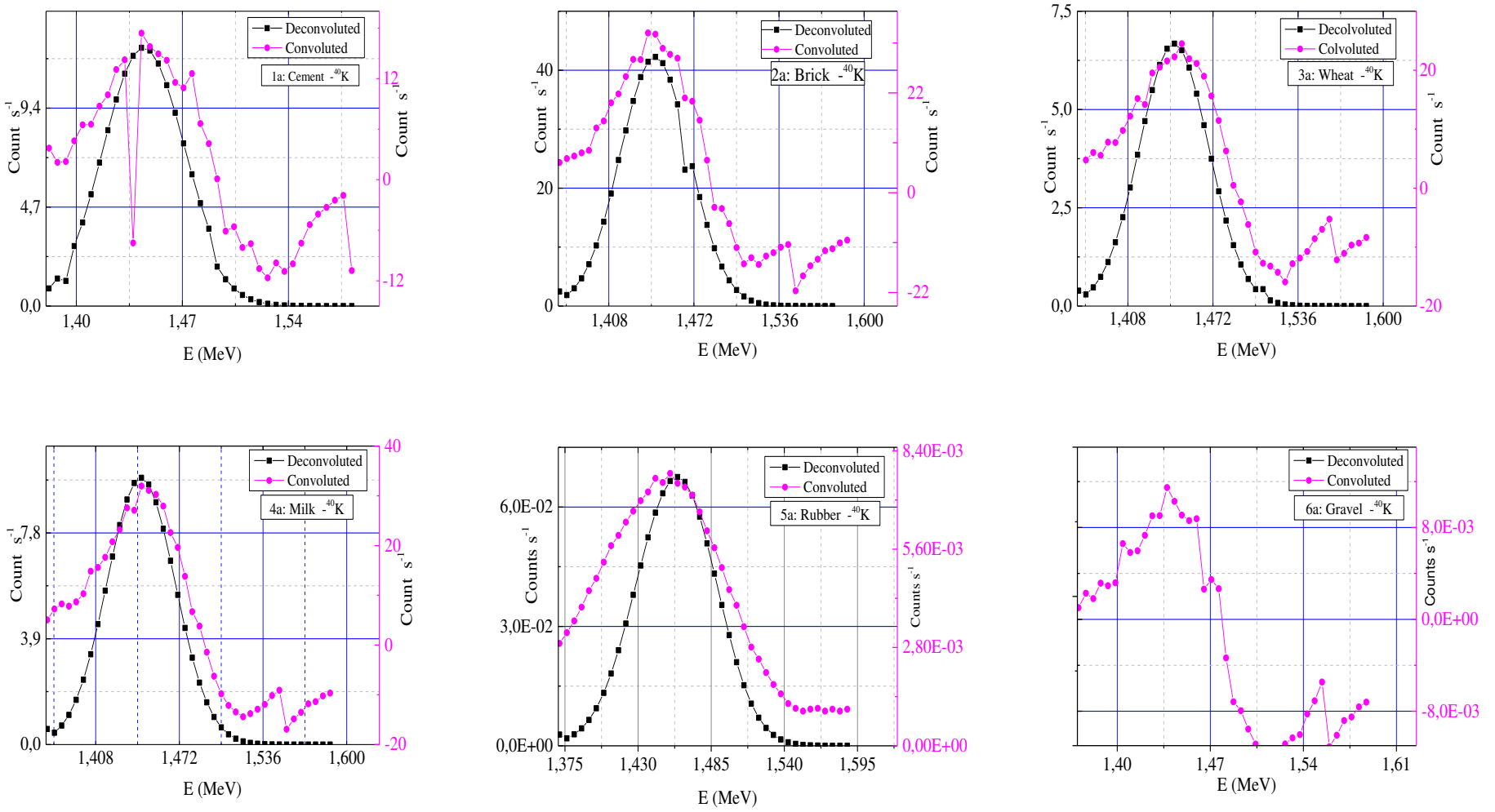

Figure 4. 8: Superposition of measured and original pulse height distribution issued for ^{40}K, and counted by 3" × 3" NaI(Tl) detector.

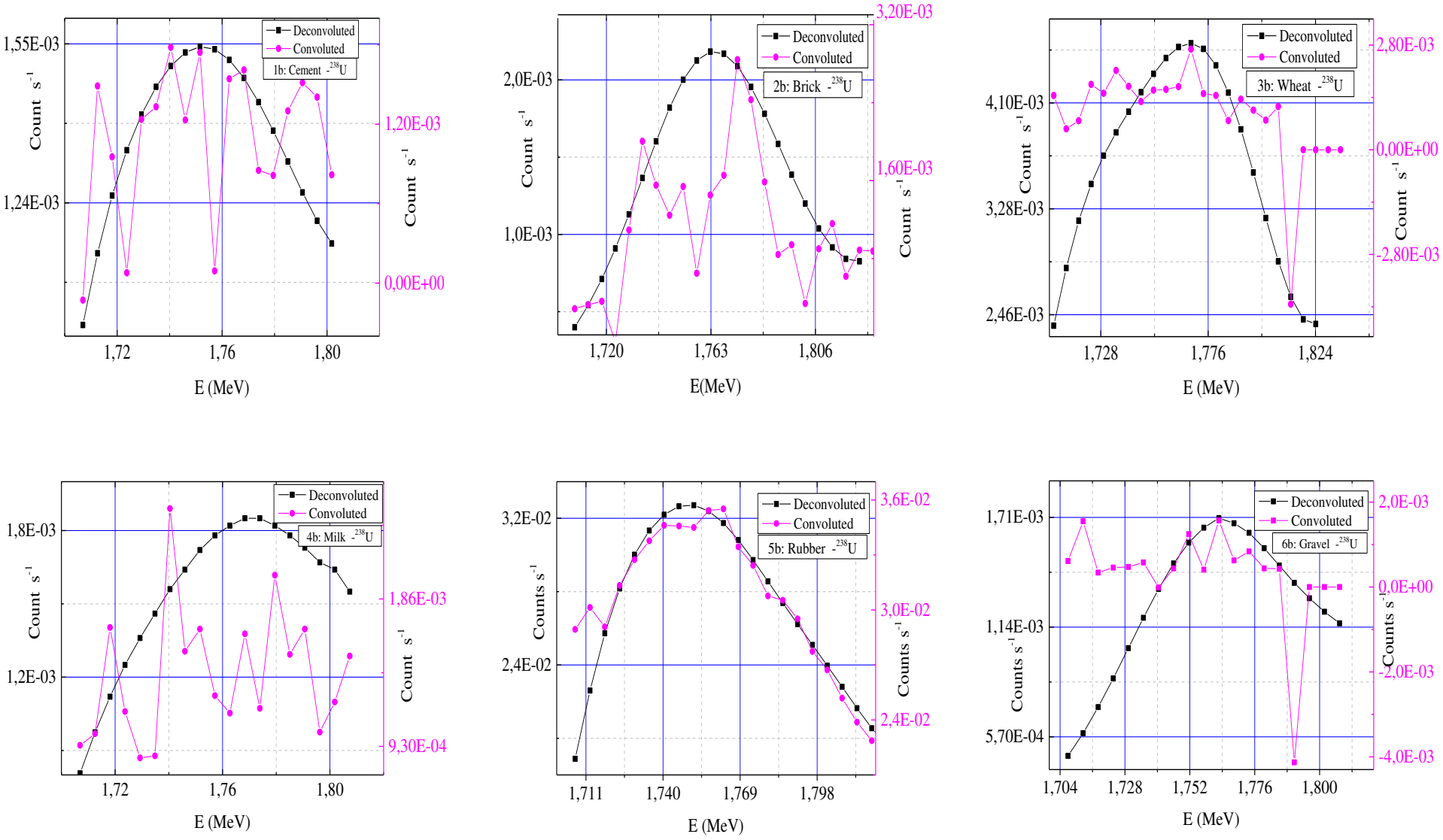

Figure 4. 9: Superposition of measured and original pulse height distribution issued for ^{238}U, and counted by 3" × 3" NaI(Tl) detector.

4.4.2. Modelization of experimental set up: efficiency calibration

In this phase, the Monte Carlo methods have been applied for detection efficiency curves for each modeled sample. In which it used one measurement geometry consisted of an identical model of NaI(Tl) detector and cylindrical polythenes beakers. In this context, the NaI(Tl) detector was already simulated and validated by standard radioactive sources (See, Chapter (2) and (3)). Also, the cylindrical polyethylene beakers were filled with six different types of each environmental sample. For routine measurement, the Geant4 code was used. Where this simulation yields the detection efficiency values that were defined by equation (1.1) (See, Chapter (1)). It should be recalled that the GEB function was included in the model to obtain the $FWHM$ realistic response of the sodium iodine spectrometer NaI(Tl).

Six different sets of the simulation were run after the modeling of volumetric source definition considering the interesting gamma lines corresponding to ^{40}K (1.46 MeV), ^{238}U (1.76 MeV), and ^{232}Th (2.16 MeV). For the modeling of environmental matrixes, it should define the finite volume of sample, elemental composition, and density values. This step is addressed to the description of measurement geometry. Regarding the chemical compositions, the powdered X-Ray Fluorescence technic (XRF) was used for cement, brick, gravel, rubber, milk, and wheat samples[9]. Accordingly, the samples are dry – sieved to eliminate any wetness or humidity, and also to assess the homogeneity of the samples. After that, the prepared samples are in form of smooth capsules with a dimension of 30 mm in diameter, and 5g of weight. Figure 4.10 represents a picture of the prepared environmental capsule format used for XRF analyses. Appendix B Table B.1 summarizes the XRF results of the studied materials. It was used to report the elemental composition in one single parameter called Z_{effe}. This latter'svalues were calculated using the reported equation used by [86 – 88]. Table 4.4 lists the density and the effective atomic numbers Z_{effe} of the analyzed materials.

Table 4. 4: Density and effective atomic number of different biological and geological samples.

Sample	*Cement*	*Brick*	*Gravel*	*Rubber*	*Milk*	*Wheat*
Density	2.08	1.87	2.06	0.7	1.17	1.207
Z_{eff}	17.66	16.6	15.53	15.97	8.63	7.31

[9]The XRF analysis was conducted in CRAPC expertise SPA, Bousmaïl, Tipaza, Algeria.

Figure 4. 10: Some geological samples prepared for XRF analyses.

Figure 4.11 shows a 3D visualization of the simulated experimental setup modeled by Geant4 code. The polyethylene – filled beaker was vertically deposed above the detector to obtain high – efficiency values i.e., approached measurement geometry. It should be mentioned that the approached geometry enhances the importance of the summing effect phenomena. Hence, there is a necessity to add energetic correction factors in respect to activity measurements. Thus, it is recommended to use the Marinelli beaker for augmenting detection efficiency values especially for low radioactivity levels. For the same purpose, the study of the optimum sample geometry (diameter and height) as density and Z_{eff} functions remains very important.

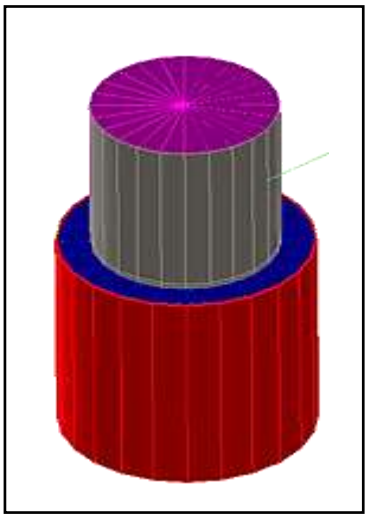

Figure 4. 11: Illustration of the NaI(Tl) model (left) used for Geant4 simulations together with an example of photon tracking (right) for the 40K, 238U, and 232Th gamma ray emissions.

Figure 4.12 presents the efficiency curves plotted by "Origin Program". It can be observed that the efficiency values are inversely related to gammas energy due to the cross – section probability of the photoelectric phenomenon. For the same geometry and at selected energy, different efficiency values can be observed between two dissimilar samples. It can be explained by the effect of the elemental composition and mass fraction of the different samples.

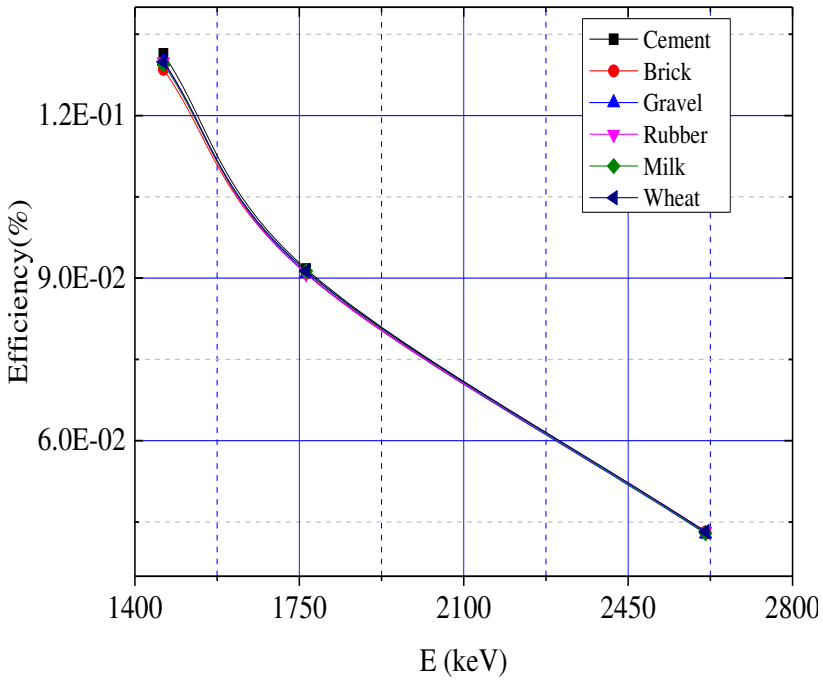

Figure 4. 12: Efficiency curves obtained by Monte Carlo calculation.

Beyond 1.46 MeV, another interesting observation can be stated that the Z_{effe} did not significantly affect the detection efficiency as it is shown in Table 4.5 and Figure 4.13.

Table 4. 5: Dependency of effective atomic number to efficiency values

Z_{effe}	$\Delta\varepsilon$ (1460.8keV)	$\Delta\varepsilon$ (2614.5keV)
Milk (8.63) and cement (17.66)	0.03	0.01
Brick (16.6) and cement (17.66)	0.03	0.2

From the obtained results, the reported values of the examined bottle will be used to calculate the activity concentration of the environmental samples.

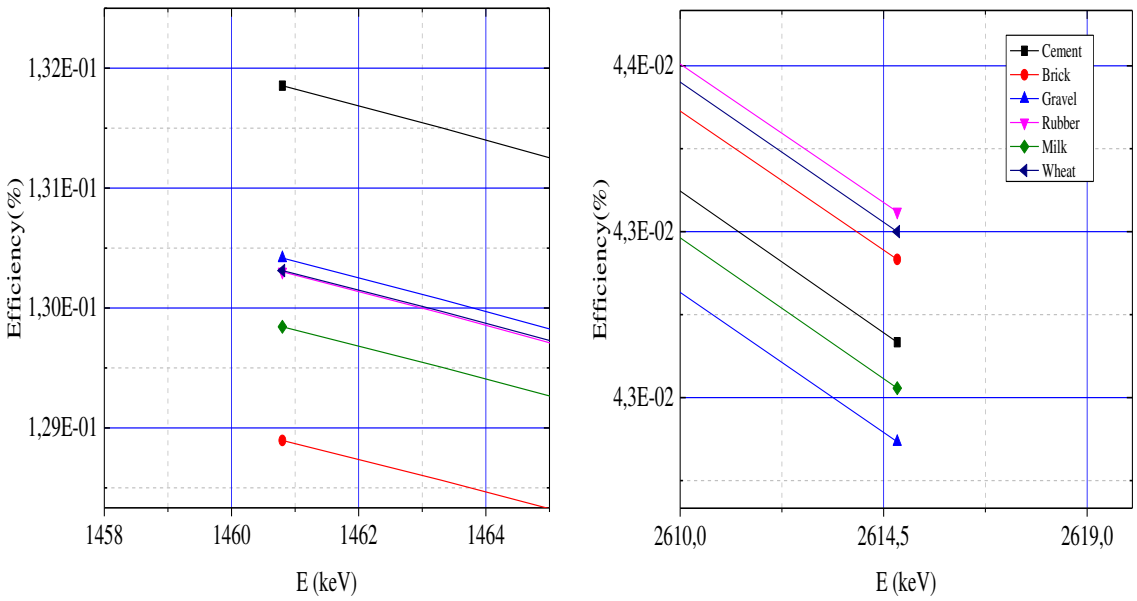

Figure 4. 13: Dependency of efficiency to effective atomic number, density, and energy.

4.4.3. Application for environmental samples: activity and radiation dosimetry

4.4.3.1. Activityconcentration

Figure 4.14 illustrates the activity concentration of the studied environmental sample. Obviously, the assessed NORM activity concentrations were varied from 0.10 to 5.37, from 0.2 to 3.7, and from 404.73 to 1793.25 $Bq.kg^{-1}$ for ^{238}U, ^{232}Th, and ^{40}K, respectively. For gravel samples, the assessed activity could not be experimentally measured because the background level was higher than the emitted radiation from ^{40}K.

It should be mentioned that the worldwide average of the NORM in construction material and the foodstuffs are outlined in the following table (by UNSCEAR):

Table 4. 6: UNSCEAR limit concentration of ^{226}Ra, ^{228}Ra, and ^{40}K in foodstuff.

	^{226}Ra (parent ^{238}U)	^{228}Ra (parent ^{232}Th)	^{40}K
Foodstuff	30	35	400
Construction materials	82	67	310

*The given limits are in $Bq.kg^{-1}$.

Figure 4.15 presents that a good correlation of 0.99 *r*is observed for all environmental samples. These results indicate that the secular equilibrium between ^{238}U and ^{232}Th daughters' radionuclides have been attained.

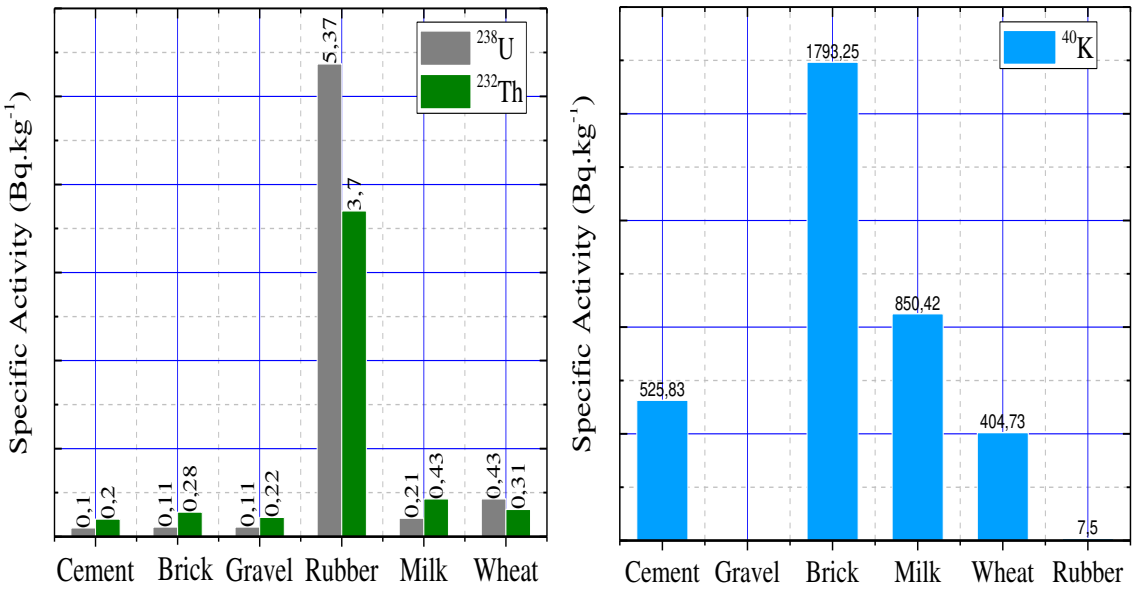

Figure 4. 14: Specific activity of ^{238}U, ^{232}Th, and ^{40}K.

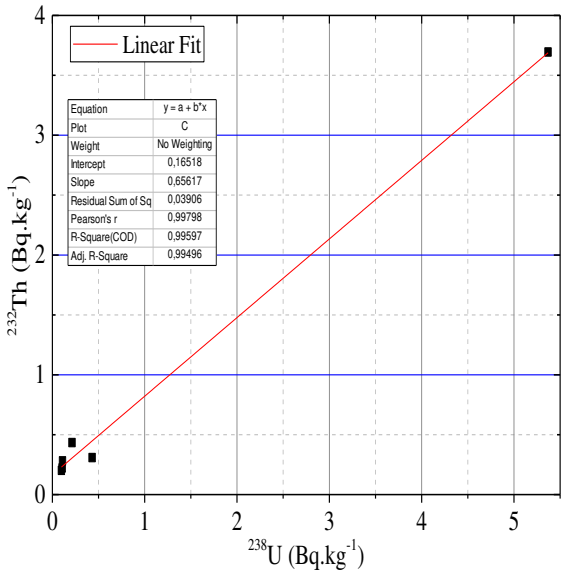

Figure 4. 15 : Correlation curve between ^{238}U and ^{232}Th.

Table 4.7 shows the range and the average values of the measured activities as well as their corresponding uncertainties of ^{238}U, ^{232}Th, and ^{40}K in powdered environmental samples in comparison to previous studies despite different methodologies used around the world. Accordingly, it has been recorded the existence of a high value of ^{40}K in order of almost 1800 $Bq.kg^{-1}$ in the powdered brick. This value is 4 times higher than the UNESCEAR worldwide average corresponding to 400 $Bq.kg^{-1}$. The measured values of ^{232}Th and ^{238}U were compatible with similar mentioned studies. In addition, Table 4.7 indicates that the measured values of ^{232}Th and ^{238}U in the cement sample were rather

similar to those obtained by M Gullyas (1984) from Hungary [18]. Moreover, the value of ^{40}K is lower than those calculated by M Gullyas (1984) [18] and O Baykara (2011) [20] from Hungary and Turkey, respectively. Based on these disparities, the concentration variance can be due to many factors including environmental characteristics (geological formation); background radiation level; and Radon concentration; etc. Regarding biological samples, the values of ^{238}U and ^{232}Th are in accord with those calculated by T Hosseini from France (2006)[10], F.L Melquiades from Brazil (2021) [79], I.U Khan from Pakistan (2020) [81], and F Alshahri from Saudi Arabia (2016). The activity concentration of ^{40}K measured in the milk sample was double of the measured values of T Hosseini from France (2006), W Priharti from Malaysia (2016) [80], S.A Amin from Iraq (2016) [78], and the UNSCEAR limit. The disparities of the specific activities of ^{238}U, ^{232}Th, and ^{40}K in the biological samples might be due to agricultural practices; environmental radiation; the geological structure of agricultural lands; the utilization of contaminated irrigation water in agriculture; consumption of milk of domestic animals consuming contaminated fodder, etc.

4.4.3.2. Radiological parameters

4.4.3.2.1. Radium equivalent

Figure 4.16 presents a graphical representation of the radium equivalent (R_{eq}) activities. For the geological samples, the values of Ra_{eq} is ranged from 0.42, 40.88, to 138.6 $Bq.kg^{-1}$for gravel, cement, and brick, respectively, with a mean value of 59.97 $Bq.kg^{-1}$. However, for the biological materials, the values of Ra_{eq} is ranged from 32.04 to 66.32 $Bq.kg^{-1}$ for wheat and milk, respectively, with a mean value of 49.18 $Bq.kg^{-1}$. It should be mentioned that the measured values did not exceed the permissible safe limit (370 $Bq.kg^{-1}$).

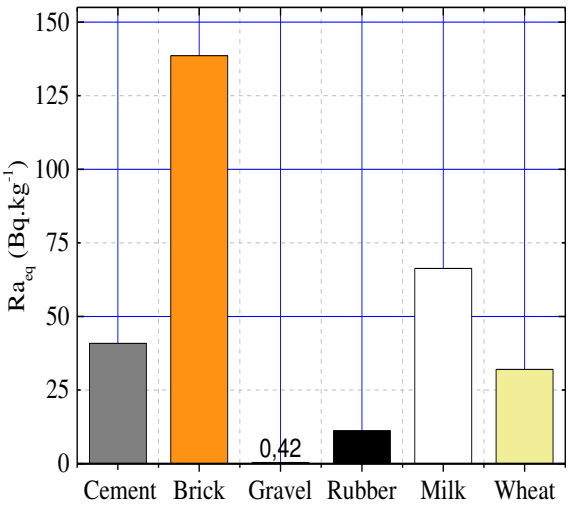

Figure 4. 16: Radium equivalent activity in $Bq.kg^{-1}$of some environmental samples.

[10] The present values was obtained from the analyses of imported foodstuff in Iran.

Sample	*Country*	*^{226}Ra ($Bq.kg^{-1}$)*		*^{232}Th ($Bq.kg^{-1}$)*		*^{40}K ($Bq.kg^{-1}$)*		*Reference*
Brick		*Min*	*Max*	*Min*	*Max*	*Min*	*Max*	
	Italy (2006)	20 ± 2	110 ± 9	25 ± 2	97 ± 8	160 ± 10	680 ± 60	(Righi, 2006)
	Italy (2015)	41.4 ± 1.5	74.4 ± 1.9	64.9 ± 3.5	87.6 ± 2.4	986.5 ± 3.7	1156.8 ± 12.7	
	Iran (2021)	20	39	19	34	167	535	(Imani, 2021)
	China (2020)	45		49		647		(Fei, 2020)
	Present Work	0.1095		0.28126		1793.2517		
Cement		*Min*	*Max*	*Min*	*Max*	*Min*	*Max*	
	Hunguray (1984)	0.6	228	0.6	199	7	709	(Gullyas, 1984)
	Turkey (2011)	2407		207		2493.1		(Oktay, 2021)
	Italy (2015)	41.04 ± 2.4	82.8 ± 2.2	58.6 ± 4.6	67.7 ± 2.6	915.4 ± 12	1033.3 ± 12.7	
	Iran (2021)	24	38	11	18	145	312	(Imani, 2021)
	Present Work	0.0981		0.20246		525.83227		
Gravel		*Min*	*Max*	*Min*	*Max*	*Min*	*Max*	
	Greec (2005)	17.8 ± 2.4	66.0 ± 1.0	4.9 ± 0.7	78.8 ± 2.2	1000 ± 13	-	(Papastefanou, 2005)
	China (2013)	56.7	90.6	92.2	138.6	324.4	448	(Guang, 2013)
	Egypt (2018)	4.59	6.01	0.89	2.95	12.57	31.6	(Moussa, 2018)
	Iran (2021)	31	81	17	25	243	454	(Imani, 2021)
	Present Work	0.106		0.22191		BDL		
Rubber		*Min*	*Max*	*Min*	*Max*	*Min*	*Max*	
	Iraq (2017)	8.484 ± 3.470		5.102 ± 2.550		337 ± 20.760		(Karar, 2017)
	Present Work	5.3693		3.69427		7.49788		
Milk		*Min*	*Max*	*Min*	*Max*	*Min*	*Max*	
	France (2006)	0.05 ± 0.011		0.142± 0.026		434.1± 13		(Hosseini, 2006)
	Malaysia (2016)	24.8		3.21		7.18		(Priharti, 2016)
	Iraq (2016)	–		–		203.43	355.88	(Amin, 2016)
	Brazil (2021)	–		<0.5 ± 35.4%		489 ± 2.65%		(Melquiades, 2021)
		–		<0.3 ± 38.22%		475 ± 2.53%		
	Present Work	0.213		0.4342		850.42131		
Wheat		*Min*	*Max*	*Min*	*Max*	*Min*	*Max*	
	Pakistan (2020)	1.075 ± 0.128	11.824 ± 1.031	0.321 ± 0.061	2.153 ± 0.022	39.248 ± 0.081	189.378 ± 1.005	(Ullah Khan, 2020)
	Saudi Arabia (2016) *WF*	1.075 ± 3.7	34.6 ± 4.1	8.56 ± 1.7	28.3 ± 3.3	200 ± 15	379 ± 19	(Alshahri, 2016)
	Wb	14.9 ± 3.5	25.7 ± 3.1	10.6 ± 3.2	26.0 ± 3.1	203 ± 26	297 ± 23	
	Bb	8.67 ± 1.0	37.3 ± 4.4	6.9 ± 0.8	2.153 ± 0.022	241 ± 19	432 ± 20	
	Present Work	0.4306		0.30823		404.72863		

Table 4. 7: Comparative study between the measured activities of ^{238}U, ^{232}Th, and ^{40}K in different types of samples.

4.4.3.2.2. Radiation hazard indexes

It should be noted that the concept of the internal hazard index (H_{in}) is defined to control the internal exposure of radon and its short – life decay products. Also, it is defined to evaluate the harmful and the radium effect on respiratory organs. On the other side, the (H_{ex}) index is used to examine the external exposure of gamma radiations. Whereby, the values of H_{ex} and H_{in} must be always less than the unit limit.

For biological materials i.e., milk and wheat, the external hazard index is varied from 8.8 E–2 to 1.79 E–01, and the internal index is ranged from 8.7 E–2 to 1.8 E–1. For the construction materials, the external hazard index is ranged from1.43 E–3 to 3.75 E–1 and the internal index is varied from 1.2 E–3 to 3.7 E–1.

The obtained results confirmed that the radiological and non – radiological risks derived from these samples are well below the limit (Figure (4.17)).

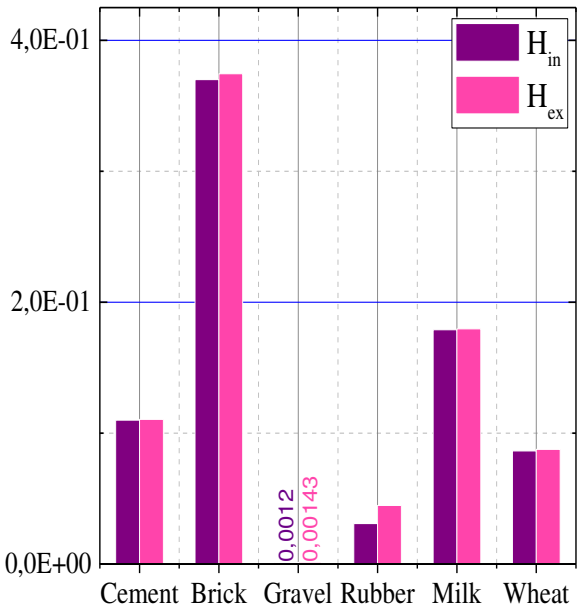

Figure 4. 17: External and internal hazard indices of analysed sample

4.4.3.2.3. Absorbed dose in construction materials

Figure 4.18 illustrates the absorbed doses attributed to gamma radiation in the different geological samples. The absorbed doses of gravel, rubber, cement, and brick are ranged from 5.02 to 74.99 $nGy.h^{-1}$ with the highest value recorded for the brick sample. The

radiological indices indicated that the investigated brick in Blida province, Algeria, is not acceptable for life long construction.

4.4.3.2.4. Annual effective dose due to the external exposing of construction materials

Figure 4.19 presents the measured annual doses $mSv.y^{-1}$ calculated for a geological sample and provided from the annual exposing of primordial radioelements. It should be noted that the showed values are calculated for adults. During one year, received radiation of 3.68 E–2, 1.08 E–2, 2.47 E–3, and9 E–4, mSv are emitted from brick, cement, rubber, and gravel, respectively.

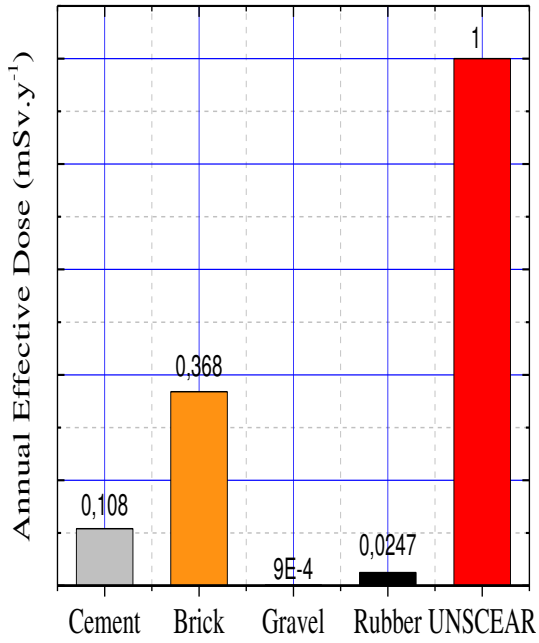

Figure 4. 18: Annual dose for environnemental sample

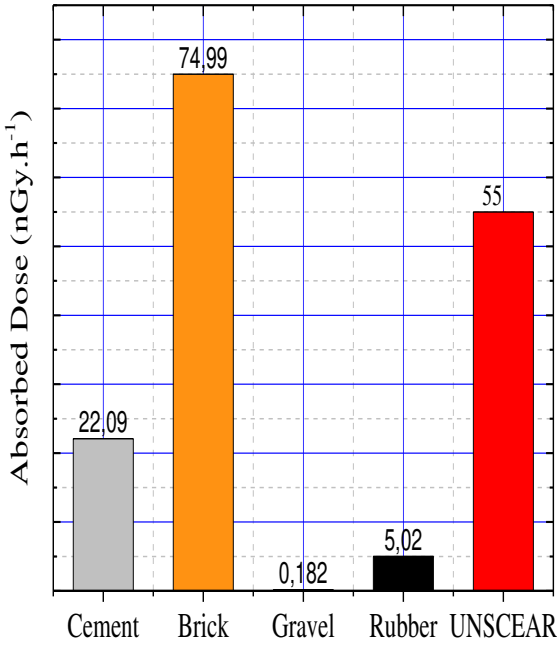

Figure 4. 19: Absorbed dose of environmental sample

4.4.3.2.5. Yearly intake of natural radionuclides from the consumption food (Bq.y^{-1})

Figure 4.20 shows the annual intake of NORMs radioactivity via the ingestion of wheat and milk samples by algerian population (adult > 17 y). The values of Y_{intake} (%) show the greatest value of ~ 96 % of wheat and 3.67 % of milk. In this example, we have suppososed that the individual consumption is limited for wheat and milk. Thereford, more statistical studies on the yearly intake of natural radionuclides from the consumption of foodstuffs for children and adults is suggested.

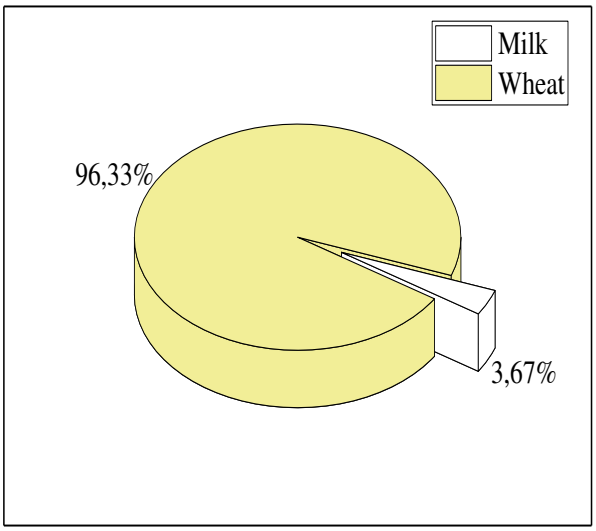

Figure 4. 20: Annual intake of radionuclides in milk and powdered wheat.

4.4.3.2.6. Annual commited dose received from the foodstuffs:

Figure 4.21 represents the annual committed dose of wheat and milk samples comparing to the UNSCEAR reference limit corresponding t 290 $mSv.y^{-1}$. In this study, the annual committed dose was calculated for the age group > 2 years i.e., the infants less than two years are considered to be non – wheat consumers as they are fed on breastfeeding only. Firstly, for the wheat sample, the obtained value corresponding to 7.88 $\mu Sv.y^{-1}$ is very greater than the reported UNSCEAR limit. This value can be explained through several factors such as the agricultural activities and/or the over – use of fertilizers in agricultural soils; contaminated irrigation water; industrial and mines activities; the sample might be industrially contaminated and/or mixed with imported wheat; the high rates of the Algerian consumption of wheat (~11 MMT per year); anda higher concentration of ^{40}K (850.42 $Bq.kg^{-1}$), etc.

UNSCEAR report (2000, Annex B Table 5) indicates that the high concentration of ^{40}K is directly related to their natural abundance in soils. At this point, the wheat and/or wheat derivers e.g., flour, breakfast cereals, semolina, pasta, etc should be carefully consumed.

Secondly, the analyzed milk powder showsan annual consumption dose of 2.28 E− 5 $\mu Sv.y^{-1}$ which is very low than Sarker (2021); Bangladesh milk, and UNSCEAR limit.

It is important to highlight that the assessed value, represents the consumption of powdered milk samples and not their derivers (cheeses, yogurts, ace creams…etc.)

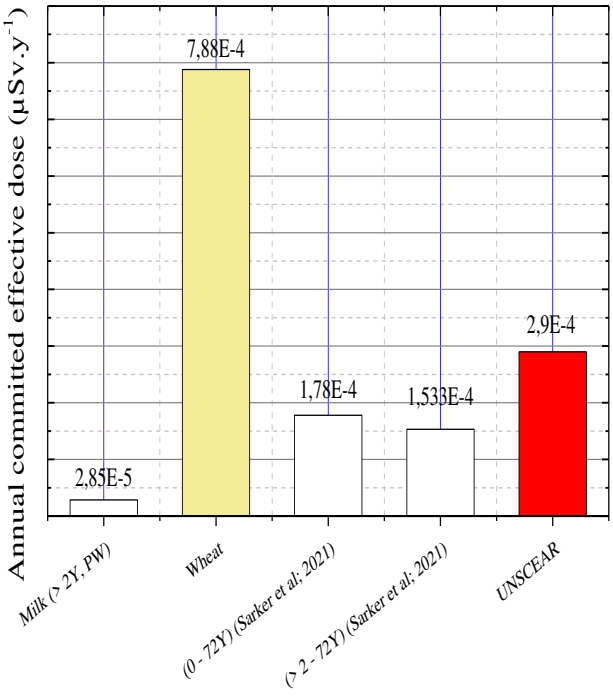

Figure 4. 21: Annual effective dose due to the consumption of milk, powdered wheat and compared to Sarker study and UNSCEAR limit[11].

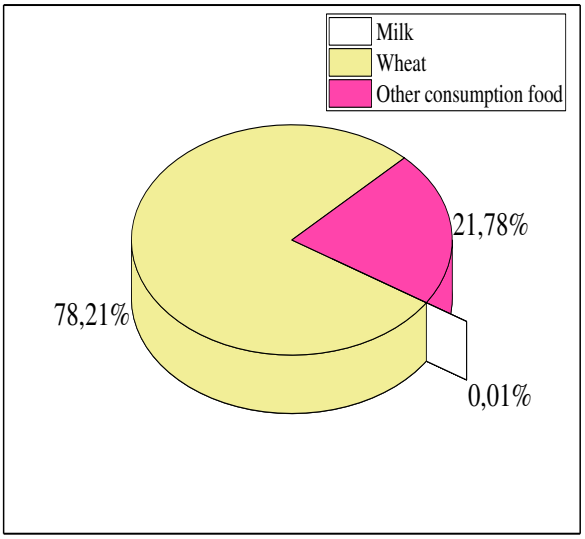

Figure 4. 22: Distribution of the annual committed dose for investigated powdered milk and wheat samples.

Figure 4.22 presents the annual distribution of committed doses for investigated milk and wheat powders. Fractionally, 0.01 % of the annual dose was taken from the ingestion of

[11] PW : Present Work

^{40}K, ^{238}U, and ^{232}Th series. Therefore, an individual adult person receives 7.88 μSv per year. In the same way, the effective dose due to the consumption of wheat sample was estimated at 78.21% while the rest at 21.78 % of the annual consumption food was coming from the ingestion of other foods. The given values indicated that the wheat food should be carefully consumed, or the annual threshold consumption should be as low as possible. A statistical study on the annual threshold consumption for children and adults can be presented in the next subsection.

4.4.3.2.7. Threshold consomption of foodstuffs

Figure 4.23 shows the annual consumption weight of wheat and milk sampleswas estimated at different age groups: children (2 – 7, 7 –12, and 12 – 17 years) and adults (>17 years). According to the UNSCEAR threshold, the individual consumption of any foodstuffs present always a significant value of intake dose provided from the NORM's.

Therefore, radiological health always exists. The results indicate that the individual consumers should decrease the annual consumption of wheat where the annual committed dose is approximately three times greater than the UNSCEAR limit (290 $\mu Sv.y^{-1}$). Building upon this point, the annual Algerian consumption of wheat should be decreased to less than one – third (~ 3 Ton per year) to reduce the radiological health risks. Thus, it means that the estimated annual consumption should be less than one-third of 32.7, 50.3, 76.3, and 107 *kg* for children of 2 – 7y, 7–12y, 12–17y, and adults > 17y, respectively, which are equivalent to ~ 22*g/day*, ~ 46*g/day*, ~70 *g/day*, and ~98 *g/day*, orderly.

For the powdered milk, the annual threshold consumption was estimated at 16, 25.6, 42.1, and 53.4 kg for groups age 2 –7y, 7–12y, 12–17y, and >17y, respectively. Therefore, the daily consumption share should be estimated at ~ 44*g/day*, ~ 70*g/day*, ~ 115*g/day*, and ~ 147*g/day* for each age group, orderly.Therefore, the reported values for the milk powder sample are lower than the results of Sarker (2021). Accordingly, more sample types should be called for more significant results including infant milk and different markets, etc.

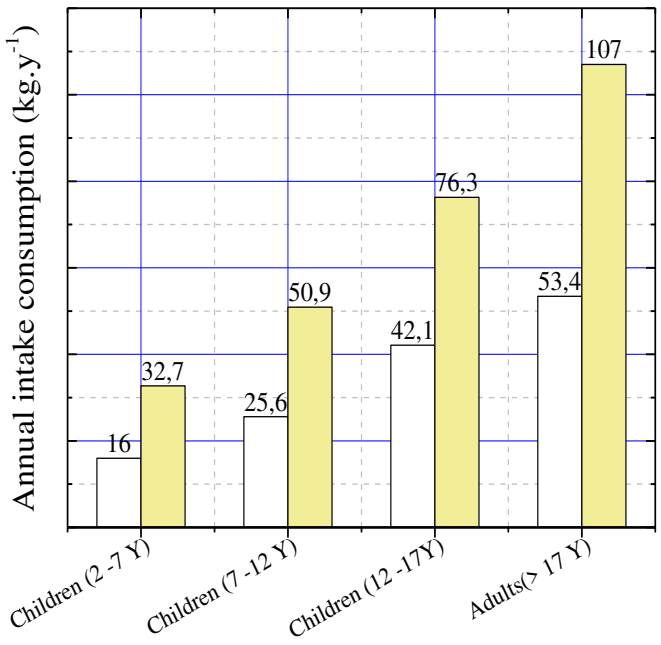

Figure 4. 23: Annual intake consumption ($kg.y^{-1}$) of investigated environnemental samples for different age groups.

4.5. Conclusion

This chapter aimed to evaluate the radioactivity level of ^{238}U, ^{232}Th, and ^{40}K in the samples of cement, brick, gravel, rubber, wheat, and milk. The evaluation of dosimetric parameters was made by combining the unfolding process (for photopeaks area) and Monte Carlo calculation (efficiency curves). The results have shown that:

- Good gaussian shape was observed after the unfolding process for $^{238}U$and ^{40}K. Therefore, the net area can be quickly analyzed. However, the unfolding of the ^{40}K area of gravel was impossible because that the input data was lower than the detection limit;
- A combination of NaI(Tl) spectrometer with the unfolding process can solve the poor resolution problem;
- It is observed that the detection efficiency was related to density, energy, and atomic effective number;
- The specific activities of the studied materials compared with other areas around the world have shown that the obtained results are comparable to *Italy* for brick corresponding to ^{40}K, *Hungary* for cement, *Egypt* for gravel, *Iran* for rubber, *France, Malaysia,* and *Iraq* for Milk, *Pakistan,* and *Saudi Arabia* for Wheat;
- It is observed that the majority of the gamma –emitting had come from ^{40}K;

- The radium equivalent average *(Ra_{eq})*, external *(H_{ex})*, and internal *(H_{in})* indices were below the recommended limit;
- The absorbed doses were within the permissible worldwide average (55 $nGy.h^{-1}$), except the brick sample that had shown a value of 75 $nGy.h^{-1}$;
- Annual external exposure of NORMs emitted from walls is estimated at 3.68 E–2, 1.08 E–2, 2.47 E–3, 9 E–4 $\mu Sv.y^{-1}$ of received radiations from brick, cement, rubber, and gravel, respectively, where the time of exposure (in offices, home…etc) was chosen at 80 %;
- The daily consumption share of the milk samplewas estimated at ~ 44 *g/day*, ~ 70 *g/day*, ~ 115 *g/day*, and ~ 147 *g/day* for the children group 2 – 7 y, 7 – 12 y, 12 – 17 y, and adults (>17 y) respectively;
- The daily consumption of wheat should be equivalent to ~ 22 *g/day*, ~ 46 *g/day*, ~ 70 *g/day*, and ~ 98 *g/day*, for age group 2 – 7 y, 7 – 12 y, 12 – 17 y, and (>17 y) respectively;
- The annual consumption of the wheat sample should be divided into one third where the annual committed dose shows ~ 3 × of UNSCEAR limit;
- The present data are estimated to protect and help the consumers and/or the people from exposureto natural radiations.

GENERAL CONCLUSION

The main objective of this thesis is the development of laboratory gamma spectrometry technic employing NaI(Tl) detector applied for environmental measurements (dosimetry). Two main objectives are treated: a) detection efficiency of large samples employing Monte Carlo code, and b) solving the poor energy resolution of NaI(Tl) spectrometer. The first part required experimental validation of the NaI(Tl) detector modelled according to the manufacturer information. Two Monte Carlo codes have been used: MC_Gamma and Geant4. The employed codes are firstly tested by standard gamma sources (^{137}Cs and KCl), and satisfactory results have been presented. Next, the detection efficiency for environmental samples was calculated using the validated code. The chemical characteristics as the densities and the elemental composition of different matrixes were determined using X-Ray fluorescence technic (XRF). The results show the dependency of the elemental composition, density, and energy on the detection efficiency values. The simulation results show that the feasibility of the Monte Carlo code for gamma – ray interaction requires the use of the detector and source parameters as size, chemical parameters, GEB function etc., where the simulator should be careful in data entering. Fortunately, the detection efficiency for large or point source, detector response function, etc., can be made employing computer code (complexity in experimental and theoretical measurements). Further, numerical simulation is necessary for energetic spectrometer purposes.

The next part consisted of solving the overlap spectrum problem. For this purpose, the GRAVEL iterative algorithm is used to restore the initial spectrum (interest ROIs regions) emitted by the gamma source. It requires the: construction of the instrument response function, outcome spectrum, background radiation level, energy bin width etc. The iterative code was examined by a standard gamma source (^{133}Ba). The unfolded window was used to calculate the source activity and therefore compared to the certified source activity. The unfolding results report the power of the used code on the subtraction of the: background, scattered and, secondary radiations issued from the diffusion or escape peaks. The results of this part (tested part) offer the validity of the followed methodology for gamma spectra unfolding. For application purposes, the concentration of the ^{40}K, ^{238}U, and ^{232}Th in different environmental samples are calculated from the photoelectric regions corresponding to 1.46, 1.76, and, 2.61 MeV respectively. It should note that: the expansion time in

GRAVEL is less than the experimental measurements and the response function construction.

The end part is interested in radioactivity and dosimetry evaluation. The radium equivalent parameter, external and internal indices, absorbed and annual doses, consumption dose (for foodstuffs), yearly intake of natural radionuclides from the consumption food, and threshold consumption rate are measured.

From these results, several conclusions can be presented: firstly, the coupling between the unfolding algorithm and the Monte Carlo method can solve the quantification and/or qualification of the interest radioactive elements; secondly, the followed methodology can also be applied as a routine method (for the same source and detector geometry) especially when the gamma spectrometer has poor resolution; thirdly, the radiological parameters can be calculated employing the created database. Where the manipulator can easily pass from density to mass activity. The purposed code is created according to the laboratory needs. It offers a simplified code (in C++ language) for activity measurement in different matrixes. From this point, the usefulness of our algorithm is the measurement in the live – time, where the bibliographical box contains the experimental and simulated data including the detection efficiency curves, density, effective atomic numbers, mathematical equation etc. Therefore, the output results reflect the experimental value.

PERSPECTIVES

– The obtained values of Z_{eff} can be used in XCom or Geant4 code to calculate the linear attenuation coefficient of the sample.Therefore, the mathematical Gauss – Legendre equation can be used to calculate the efficiency of large samples. In the same way, the Z_{eff} values can be used in MC_Gamma to calculate the detection efficiency at 1.46, 1.74, and 2.61 MeV.

– It was very interesting to compare similar results obtained by GRAVEL code with other unfolding methodssuch as experimental technic, mathematical calculations, etc.

References

[1]. S.Y.L Mouandza, A.B Moubissi, P.E Abiama, T.B Ekogo, and G.H Ben – Bolie, Int J. Rad. Res. 16 (2018) 443 – 453.

[2]. L.S Quindós, P.L Fernández, J Soto, C Ródenas, and J Gómez, Health Phys. 66 (1994) 194 – 200.

[3]. H Al–Baidhani, K Gunoglu, and A Iskender, Int J. Com. and Exp. Sci. and ENg. 5 (2019) 48 – 51.

[4]. C Bangou, F Otoo, and E Ofori Darko, Methods X. 8 (2021)

[5]. O Günay, M.M Saç, M çhedef et al., Int. J. Environ. Sci. and Technol. 16 (2019) 5055 – 5058.

[6]. A.K Ademola, I Ayo, Babalola, et al., J. of Med. Phy. 39 (2014) 106 – 111.

[7]. A Rani, S Mittal, R Mehra, and R.C Ramola, J. App. Radi. and Isot. 101 (2015) 122 – 126.

[8]. S Özden, and S Aközcan, Arab. J. Geosci. 14 (2021).

[9]. G Bouhila, A Azbouche, F Benrachi, et al., J. Environ. Earth. Sci. 76 (2017).

[10]. N Venunathan, C.S Kaliprasad, and Y Narayana, J. Rad. Prot. Dosim. 171 (2016) 271 – 276.

[11]. F Darabi – Golestan, A Hezarkhani, and M.R Zare, J. Mar. Pollu. Bul. 118 (2017) 197 – 205.

[12]. N.M Ibraheim, S Shawky, and H.A Amer, J. App. Radi. and Isot. 46 (1995) 297 – 299.

[13]. Y Kobya, H Taşkın, C.M Yeşilkanat, et al., J. Radioanal. and Nucl. Chem. 303 (2015) 287 – 295.

[14]. N.H Cutshall, I.L Larsen and C.R Olsen, J. Nuc. Instru. and Meth. in Phy. Res. A 206 (1983) 309 – 312.

[15]. M Bolca, M.M Saç, B Çokuysal, T Karalı, and E Ekdal, J. Radi. Measu. 42 (2007) 263 – 270,

[16]. S Righi, L Bruzzi, J. of Env. Radio. 88 (2006) 158 – 170.

[17]. M Imani, et al., J. Env. Sci. and Pollu. Res. (2021).

[18]. T Fei, P Xuan, Z Qiang, and Z Jing, J. Rad. Prot. and Dosi. 188 (2020) 316 – 321.

[19]. M Gullyas, and I Török, J. Rad. Prot. and Dosi. 7 (1984) 1 – 4.

[20]. O Boykara, K Sule, and D Mahmut, J. of Rad. Meas. 46 (2011) 153 – 158.

[21]. M Moussa, M.A.M Uosif, S.A.M Issa, A.A Ebrahim, and E.M Zahran, J. of Nuc. and Rad. Phy. 13 (2018) 39 – 57.

[22]. Y Guang, L Xinwei, Z Caifeng, and L Nan, J. Rad. Prot. and Dosi. 155 (2013) 512 – 516

[23]. C Papastefanou, S Stoulos, and M Manolopoulou, J. Radioanal. and Nuc. Chem. 266 (2005), 367 – 372.

[24]. R Hewamanna, C.S Sumithrarachchi, P Mahawatte, H.L.C Nanayakkara and H.C Ratnayake, J. App. Radi. and Isot. 54 (2001) 365 – 369.

[25]. S.A Amin, and M Naji, J. Rad. Phy. and Chem. (2013) page 144.

[26]. D Amrani, and M Tahtat, J. App. Radi. and Isot. 54 (2001) 687 – 689.

[27]. C Ye, J Liu, et al., J. Radioanal. and Nucl. Chem. 314 (2017) 1547 – 1555.

[28]. IAEA, International Atomic Energy Agency, Annual Report 2010.

[29]. UNSCEAR, United Nations Scientific Committee on the Effects of Atomic Radiation (1988).

[30]. UNSCEAR, United Nations Scientific Committee on the Effects of Atomic Radiation (2000a).

[31]. WHO, World Health Organization, Ionizing Radiation in our Environment (2012).

[32]. P Tchokossa, J.B Olomo, F.A Balogun, and C.A Adesamni, Int. J. Environ. Sci. and Technol. 3 (2013) 245 – 250.

[33]. WHO, World Health Organization, Ionizing Radiation in our Environment (2011), Nuclear accidents and radioactive contamination of foods. Retrived July 8.

[34]. N.N Jibiri, L.P Farai, and S.K Alausa, J. Rad. and Env. Biophy. 94 (2007) 31 – 40.

[35]. E Mahiban Ross, Y Lenin Raj, S Godwin Wesley, and M.P Rajan. J. Envi. Radio. 115 (2013) 201 – 206.

[36]. G Le Petit, and G Granier. EC DOC (2002).

[37]. UNSCEAR, United Nations Scientific Committee on the Effects of Atomic Radiation (1997).

[38]. A.S Alaamer, J Tur. J. of Eng. and Envir. Sci. 32 (2008) 229 – 234.

[39]. S.N Tahir, K Jamil K, J.H Zaidi, M Arif, N Ahmed, and S.A Ahmad. J. Rad. Prot. Dosim. 113 (2005) 421 – 227.

[40]. Pearce A, Recommended Nuclear Decay Data. NPL Report IR 6. National Physical Laboratory, Middlesex (2008).

[41]. F.M Khan, and J.P Gibbons, Physics of Radiation Therapy, John P. Gibbons — Fifth edition. (See pages: 16 –18, 58).

[42]. G.F Knoll, Radiation Detection and Measurement, John Wiley & Sons — 3rd edition., New York. (See page: 49, 50 – 51, 51, 223, 223 – 224, 231, 409).

[43]. N Tsoulfanidis, and S Landsberger, Measurement and Detection of Radiation, Taylor & Francis Group — 4th edition. (See pages: 141 – 142, 142 – 143, 145, 203, 204, 207).

[44]. R.D Evans, The Atomic Nucleus, McGraw – Hill Book Co, New York, 1955.

[45]. J.B Birks, The Theory and Practice of Scintillation Counting. Pergamon Press, London, 1964. (See: mecanism of scintillation).

[46]. J Jurkowski, T Jurkowska, R Misiak, A Szperlak, and W Kowalski, Coaxial and Planar HPGe Detectors.

[47]. V Lohrabian et al., J. Rad. Phys. and Chem. 189 (2021) 271 – 276.

[48]. M Moszyński, A Syntfeld-Każuch, L Swiderski, M Grodzicka, J Iwanowska, P Sibczyński, and T Szczęśniak, J. Nuc. Instru. and Meth. in Phy. Res. A. 805 (2016) 25 – 35.

[49]. D Darambara, and A Todd – Pokropek, J. Nuc. Med. 46 (2002) 3 – 7.

[50]. H Métivier, Radioprotection et ingénierie nucléaire, EDP Science, 2006.

[51]. J.C Nénot, J Brenot, D Laurier, A Rannou and T Dominique, The ICRP Recommendations, J. Rad. Prot. Dosim. 127 (2007) 2 – 7.

[52]. Recommendations of the International Commission on Radiological Protection, ICRP Publication 103 (2007), Published by Elsevier Ltd. Volume 37, NOS 2 – 4.

[53]. C.M Davisson, Interaction of γ – Radiation with Matter (P. 37 – 78), Gamma – Ray Attenuation Coefficients (P. 827 – 843), Alpha, Beta, and Gamma-Ray Spectroscopy, K. Siegbahn, ed., North – Holland, Amsterdam (1965).

[54]. Radioisotopes et Méthodologies de Rayonnement I, II. Soo Hyun Byun, note des cours. Université McMaster, Canada.

[55]. J Boson, G Ågren, and L Johansson, J. Nuc. Instru. and Meth. in Phy. Res. A. 587 (2018) 304 – 318.

[56]. D.M.M Olivares, M.M Guevara, and F.G Velasco, J. App. Radi. and Isot. 130 (2017) 34 – 42.

[57]. R.G Helmer, J.C Hardy, V.E Iacob, M Sanchez – Vega, R.G Neilson and J Nelson, J. Nuc. Instru. and Meth. in Phy. Res. A. 511 (2003) 360 – 381.

[58]. K Gehrcke, 33 (1990), 21 – 26 https://inis.iaea.org/search/search.aspx?orig_q=RN:21020525.

[59]. R.M.W Overwater, The physics of big sample sample instrumental neutron activation analysis, (1994) Thesis. Delft University Press Stevinweg 1, Technische Universiteit Delft.

[60]. M.I Abbas, J. Radiat. Phys. Chem. 60 (2001) 3 – 9.

[61]. M.I Abbas, and Y.S Selim, J. Nuc. Instru. and Meth. in Phy. Res. A. 480 (2002) 651 – 657.

[62]. M.I Abbas, Y.S Selim, and Nafee S, J. Radiat. Phys. and Chem. 75 (2006) 729 – 736.

[63]. A El – khatib, M.S Badawi, M Abd – elzaher, and A.A Thabet, J. Adv. Res. Phys. 3 (2012) 1 – 8.

[64]. M.I Abbas, J. Nuc. Instru. and Meth. in Phy. Res. B. 256 (2007) 554 – 557.

[65]. M Mostajaboddavati, S Hassanzadeh, H Faghihian, M.R Abdi, and M Kamali, J. Radioanal. and Nucl. Chem. 268 (2005) 539 – 544.

[66]. N Mezerreg, A Azbouche, and M Haddad, J. of Env. Radioa. 232 (2021) 106573.

[67]. S Ahmadi, S Ashrafia and F Yazdansetad, J. of Instr, 13 (2018) P05019.

[68]. M Tourang, A Hadadi, M Athari, and D Sardari, J. Radiat. Phys. and Chem. 327 (2021) 345 – 352.

[69]. S.A Dupree and S.K Fraley, Monte Carlo Primer: A pratical approach to radiation transport, Kluwer Academic/Plenum Publishers, New York, Boston, Dordecht, London, Moscow (2002).

[70]. S Agostinelli et al., J. Nuc. Instru. and Meth. in Phy. Res. A. 506 (2003) 250 – 303.

[71]. R.A.R Bantan, M.I Sayyed, K.A Mahmoud, and Y Al – Hadeethi, J. Prog in Nucl. Ener. 126 (2020) 103405.

[72]. M Irfan, Prasad, and R.D.G Relative, J. Nucl. Instrum. Meth. 88 (1970), 165 – 176.

[73]. Y.S Selim, M.I Abbas, J. Phys. 26 (1995), 79 – 89

[74]. N Demir, U.A Tarim, and O. Gurler, Int. J. Rad. Res. 15 (2017) 123 – 128.

[75]. M Abramowitz, and I Stegum, Handbook of Mathematical Functions with Formulas, Graphs, and Mathematical Tables, Dover Publications (1964).

[76]. J Baró, J Sempau, J.M Fernández – Varea, and F. Salvat, J. Nuc. Instru. and Meth. in Phy. Res. B. 100 (1995) 31 – 46.

[77]. A Karar, and K Mohsin. Words news of natural science (2017). EISSN 2543 –5426.

[78]. S.A Amin, M.S.M AL – kafaje, and R.R. Al – Ani, J. of Natu. Sci. Res. 6 (2016).

[79]. F.L Melquiades, and C Appoloni, J. Tecnol. Aliment. 24 (2021) 501 – 504.

[80]. W Priharti, S.B Samat, M.S Yasir, and N.N Garba, J. of Radioanal. and Nucl. Chem. 307 (2016) 297 – 303.

[81]. I.U Khan, W Sun, and E Lewis, J. of Food Prot. 83 (2020) 377 – 382.

[82]. F Alshahri, Life Sci. J. 13 (2016) 34.

[83]. J Beretka, P.J Matthew et al., Health Phy. 48 (1985) 87.

[84]. F Otoo, et al., Res. J. of Env. and Ear. Sci. 3 (2011).

[85]. M Ngachin, M Garavaglia, C Giovani, M.G Kwato Njock and A Nourreddine, J. of Env. Radio. 99 (2008) 1056 – 1060.

[86]. E Pantelis, A.K Karlis, M Kozicki, P Papagiannis, L Sakelliou and J.M Ro – siak, Phy. in Med. and Biol. 4 (2004) 3495 (See page 117).

[87]. K Meynard, Polymérisation radio – induite : Calcul de dose et modélisation dans le cas d'irradiations prolongées de sources non scellées, (2009) Thesis, Université de Toulouse III–Paul Sabatier, Toulouse, France (pages 62 and 117.)

[88]. A.K Jones, D.E Hintenlang, and W.E Bolch. Med. Phy – Sics. 30 (2003) 2072 (See page 117.)

[89]. UNSCEAR, Exposures from Natural Radiation Sources. Annex B PP.124 –127 (2000 b).

[90]. UNSCEAR, Sources and Effects of Ionizing Radiation. Annex B Vol. 1 (2008)

[91]. M.U Khandaker, N.B Wahib, Y.M Amin, and D.A Bradley, J. Radi. Phy. and Chem. 88 (2013) 1 – 8.

[92]. M.U Khandaker, H.K Shuaibu, F.A.A Alklabi, K.S Alzimami, and D.A Bradley, J. Health. Phy. 116 (2019) 789 – 798.

[93]. GAIN Report, Global Agricultural Information Network, Algeria, 2019.

[94]. M Matzke, Unfolding of Pulse Height Spectra, Technical Report PTB-N – 9 (2000)

[95]. M Reginatto, Unfolding programs in the UMG Package: MXD_FC31 and IQU_FC31, and GRV_FC31. Technical Report (2000)

[96]. M Matzke (2002) Propagation of uncertainties in unfolding procedures, J. Nucl. Instr. Meth. Phys. Res. A .

[97]. M Matzke, Unfolding of Particle Spectra. In: Editor PS 2867 (ed) International Conference: Neutrons in Research and Industry. Crete, Greece, (1997) 598 – 607.

[98]. M.J Berger, and S.M Seltzer, J. Nucl. Instru. Meth. 104 (1972) 317 – 332.

[99]. N Starfelt, and H.W Koch, Phy. Rev. 102 (1956) 1598 – 1611.

[100]. P.C Fisher, and L.B Engle, Phy. Rev. 134 (1964) B 796 – B816.

[101]. M.S.D Sarker, R Rahman, M.M.M Siraz, M.U Khandaker, and S Yeasmin, J. of Radi. Phy. and Chemi. (2021).

Appendix A Monte Carlo Simulations

The present Appendix describes numerical Monte Carlo used for detection efficiency measurement. In addition, it presents the execution steps for gamma spectra unfolding using Gravel code.

A.1.Modeling interaction mechanisms

The process of interaction of the incident history with the target in any Monte Carlo program is done by sampling X random number uniformly distributed between 0 and 1. The total cross – section and the geometrical path length should be considered.

If the distance "X" traveled by the incident photon is higher than the thickness L of the target, the incident photon will not interact in the active volume of the detector, and it will be dead (not counted). Au contraire, if the path length is less than the traveled distance, the cross – sections of interactions will be considered.

$$
\begin{aligned}
0 \le X \le \frac{\sigma_{pe}}{\sigma_{tot}} &\quad \text{Photoelectric effect} \\
\frac{\sigma_{pe}}{\sigma_{tot}} \le X \le \frac{\sigma_{pe}+\sigma_{com}}{\sigma_{tot}} &\quad \text{Compton scattering} \\
\frac{\sigma_{pe}+\sigma_{com}}{\sigma_{tot}} \le X \le \frac{\sigma_{pe}+\sigma_{com}+\sigma_{r}}{\sigma_{tot}} &\quad \text{Rayleigh scattering} \\
\frac{\sigma_{pe}+\sigma_{com}+\sigma_{r}}{\sigma_{tot}} \le X \le \frac{\sigma_{pe}+\sigma_{com}+\sigma_{r}+\sigma_{pp}}{\sigma_{tot}} &\quad \text{Paires production}
\end{aligned}
\qquad (A.1)
$$

A.2. Monte Carlo simulation codes

A.2.1. MC_Gamma: photo – peak efficiency measurements

The matrix compositions, the geometry of the detector and the sample, the distance between them must be introduced during MC_Gamma execution. The next example is written in MC_Gamma language for efficiency measurement (Figure A.1 and A.2).

A.2.2. Geant4: efficiency, attenuation, and response function construction

The triangular response function of the NaI (Tl) scintillation counter was done using the Monte Carlo code based on Geant4 (GEometry ANd Tracking) code (Figrue A.3). The physic list used in this study is G4EmStandardPhysicsList. The detector and source geometries are structuredusing the **Detector Construction** class. Or, it should define the dimension, orientation, density, material composition of the detector, surrounded materials, and the characteristics of the sample. For the incident particle, it should define the type, the energy range in **Primary Generator Action** (electromagnetic). The last step is to define the number of primary particles in the **Run Action** class. The process of interaction and the cross – sections of any primary particle are defined in the **Physic List** class.

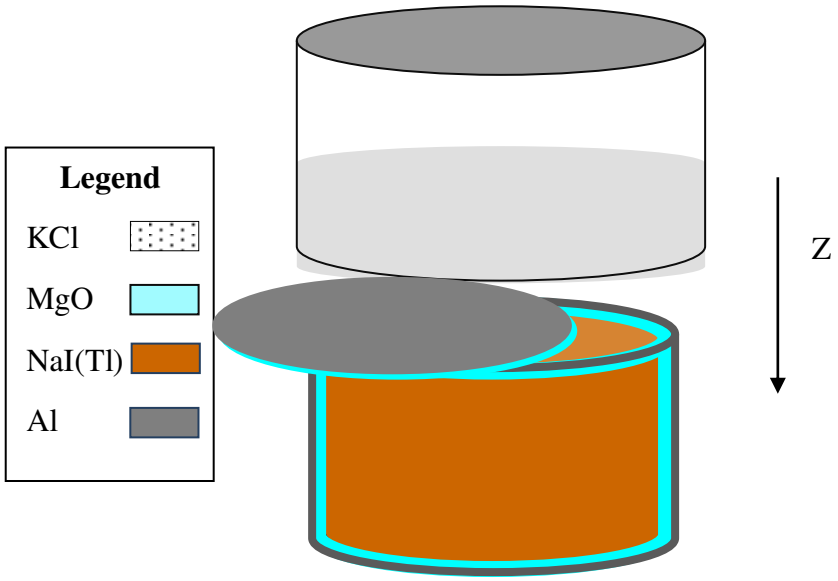

Figure A. 1: Extended source geometry and NaI(Tl) 3” × 3” detector used for efficiency measurement.

```
Object      n     1      :   Cylinder
Centre                   :   (0,0, 0.1)                          Polythylene beaker
Dimensions               :   (4.72 ,4.72, 4.52)
Object      n     2      :   Cylinder
Centre                   :   (0,0, 0.2)                          KCl sample
Density                  :   50  mass % of  Z= 19
                             50 mass % of  Z= 17
                             Object is a SOURCE
Object     n      3      :   Bar...(Air)
Centre                   :   (0, 0, 0)                           Air
Object      n     4      :   Cylinder
Centre                   :   (0,0, -0.1)                         Aluminium
Dimensions               :   (3.85, 3.85, 7.7)
Density                  :   2.7 g.cm-3
                             100 mass % of  Z= 13

Object      n     5      :   Cylinder
Centre                   :   (0,0, -0.3)                         MgO
Dimensions               :   (3.85, 3.85, 7.7)
Density                  :   2.0 g.cm-3
                             50  mass % of Z= 12
                             50 mass % of  Z= 8

Object      n     6      :   Cylinder
Centre                   :   (0, 0, -0.4)                        NaI(Tl)
Dimensions               :   (3.81, 3.81, 7.62)
```

Figure A. 2: Execution process in MC_Gamma code for KCl large sample

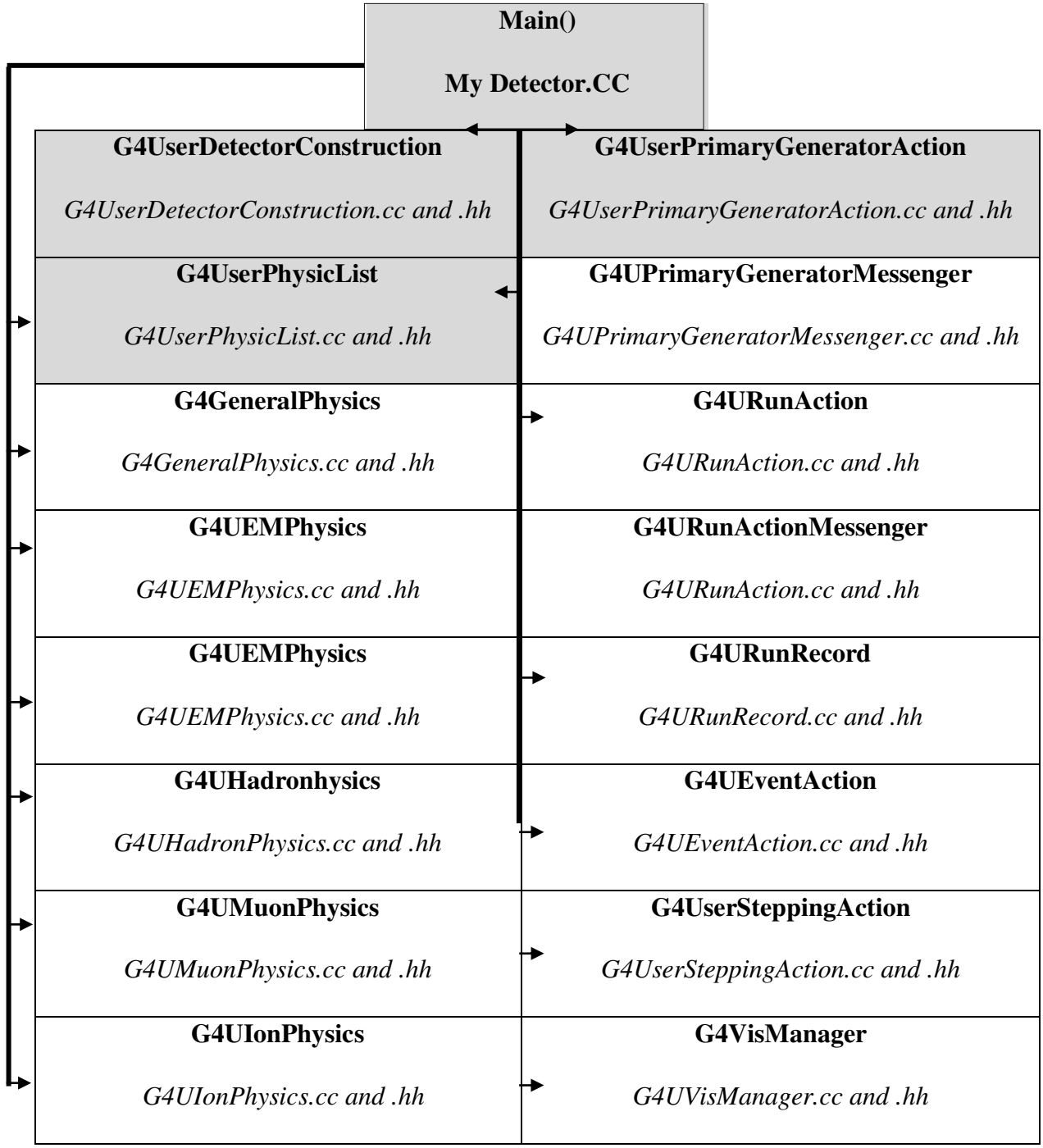

Figure A. 3: Geant4 diagramm. By CERN, Geant4.

A.2.3. XCom and Geant4: Self-absorption measurements

A.2.3.1. XCom

Open access to the open database called XCom adapted to the mass attenuation coefficient for any energy range and any type of target (mixture, compound, or element) is

presented. The particle cross – sections are introduced in XCom program. The output file contains the total attenuation coefficient as energy function (in a table and figure format).

A.2.3.2 Geant4

In Figure A.4, I_0 and I are the incidents and the transmitter number of photons traversed at X thickness.

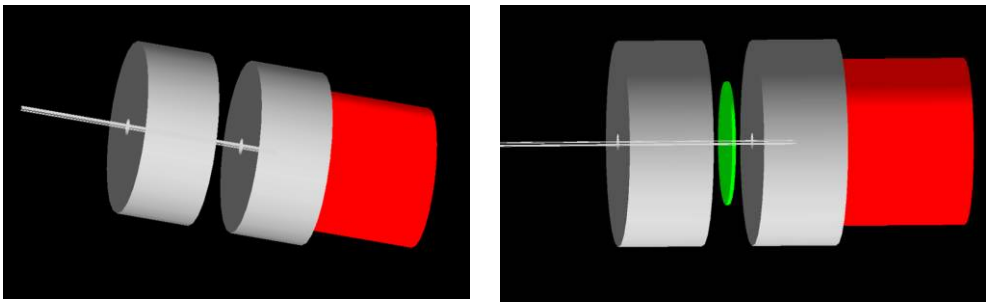

a. Without target (I_0) b. With target (I)

Figure A. 4: 3D visualization of experimental set-up simulated for linear attenuation measurement using Geant4 code.

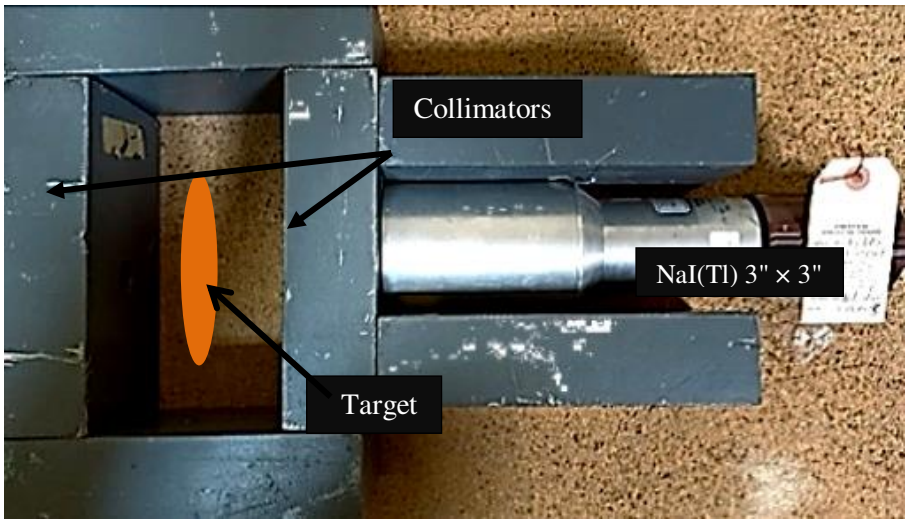

Figure A. 5: Experimental setup.

A.2.4 GRAVEL: unfolding algorithm

The description given in Matzke reference for computing HEPROW code enables the user to construct any input file easily in HEPROW format. In this thesis, only the next classes were used for spectra unfolding, by priority order. From the same reference, the original (deconvolve) spectrum is:

$$Z_i^{\alpha+1} = Z_i^{\alpha} \exp\left(\frac{\sum_k^{nk} A_{ik} \ln\left(\frac{\phi_k}{R_k^{\alpha}} \right)}{\sum_{k=1}^{nk} A_{ik}^k} \right)$$

Or the incident gamma spectrum is given by:

$$\phi_k = \sum_i R_{ik} \times Z_i = \sum_i R_{ik} \times \exp\left(\ln\left(Z_i\right)\right)$$

In the next equation, TAYLOR series at second term is introduced:

$$\ln Z_{\vartheta}^{k+1} - \ln Z_{\vartheta}^{k+1} = \lambda_{\vartheta'}^{k} \sum_i \left(\ln \phi_{i0} - \ln \phi_i^{(k)}\right) \frac{A_i^{(k)}}{\rho_i^2}$$

During GRAVEL running, the iteration procedure stopped for the minimum value of the covariance matrix χ^2 (minimum value of uncertainty). The value of χ^2 per degree of freedom is defined as:

$$\frac{\chi^2}{n} = \frac{1}{n} \sum_i \frac{\left(\sum_i R_{ij} Z_j - Z_i \right)^2}{\sigma_i^2}$$

It should be noted that a very good solution $\frac{\chi^2}{n} \approx 1$ should be considered as consistent. So, if $\frac{\chi^2}{n}$ is almost 1, the iteration is convergent.

UMSPHW	Transformation of the measured pulse – height of the radioactive source and the background in HEPROW format "*extension .phs*".The objective is to have the same energy structures for two input files. The energy calibration, *XI0* channel number related to energy 0, the bin width "*EKA*" in MeV, counting time, number of pulse in each channel "*UNS*", number of channels, dead time *"Tcorr"* and the name of input "*extension .PH*" and file are needed.
OPERAW	Applied for the subtraction of background from measured spectrum. The input files have the same energy and *MODE* parameter (0 for point value F(i), 1 for average value ie F(i) and, 2 for σ(i) group value (MC and multichannel values), 3 for group value per unit of lethargy. The input file must be in HEPROW format "*extension phs*". The resulting file is a single input pulse height file without background. The name of the output data file is "*OPR_1.phs*".
RSPGW	The ideal response function R is continuing only in a single file. The Gaussian energy bordering or the FWHM must be introduced.
GRAVEL	Unfolding program applied for particle spectra in selected energy range.

Figure A. 6: Steps of unfolding gamma spectra using GRAVEL code.

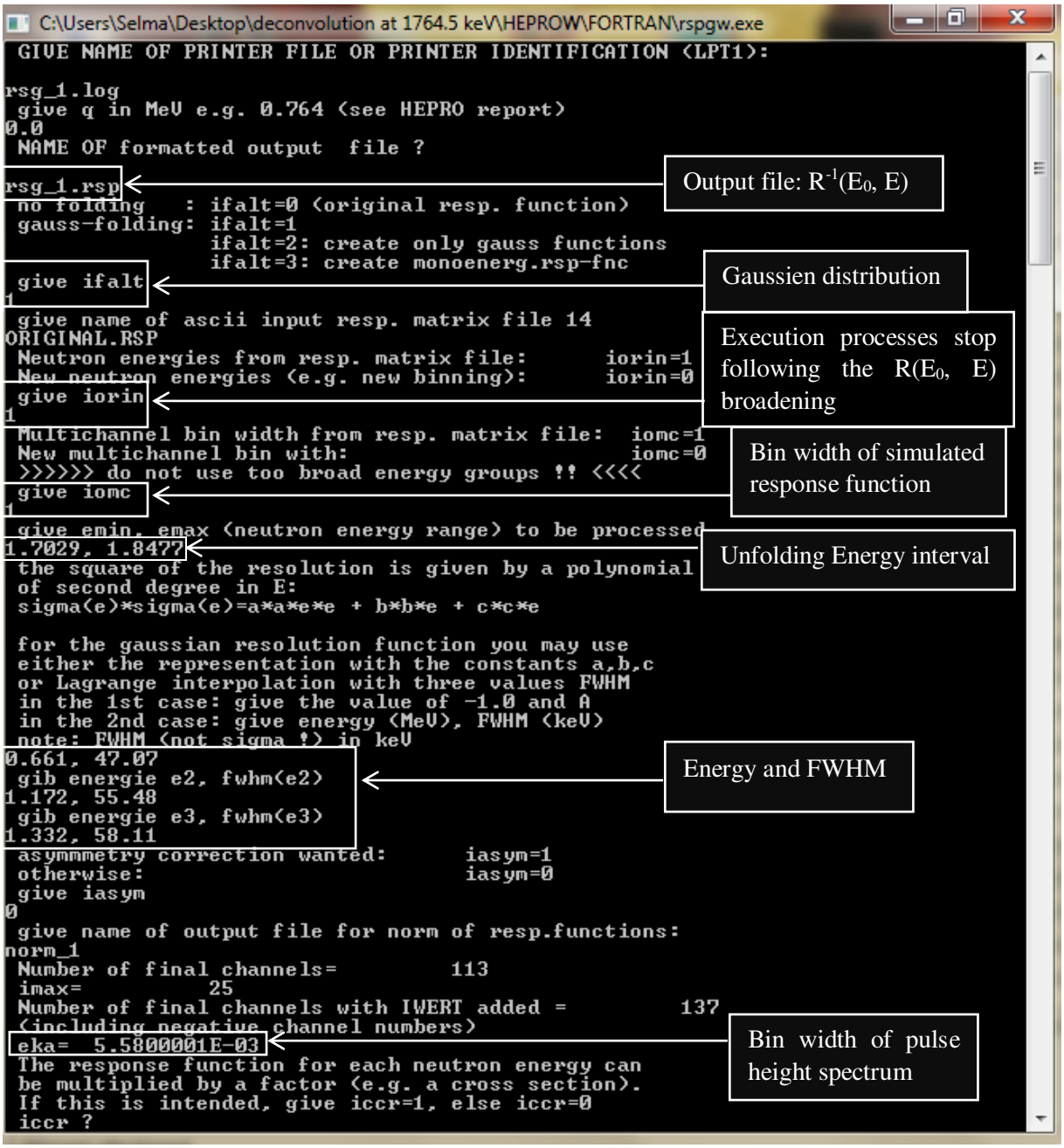

Figure A. 7: Execution process for inversing matrix. The input data file is ORIGINAL.RSP

```
N=60 //degree of precision
PI=3.14 // π value
A=2 // distance between the detector and the scal of cylindrical counter
B=12 // distance between the detector and the top of cylindrical counter
ALFA=0.5*(B-A)// parameters of Chebychev transformation
BETA=0.5*(B+A)//parameters of Chebychev transformation
S=0
Do      H=1*K
Z(K)= cos((PI*float(2*k+1))/(2*(N+1))//the transformation function
COF=sqrt(1- Z(K)* Z(K))
S=S+ COF*eps(Z(K))
Continue
S=(ALFA*PI)/(float(N+1))// effciency values
Stop
End
```

Figure A. 8: MATLAB language for efficiency measurement (Gasse – Legendre method).

Appendix B Effective Atomic Number

The detector model and the gamma-ray source must be introducedfor efficiency calibration using either MC_Gamma or Geant4 codes. To facilitate the definition of source geometry, a single quantity called Z_{eff} (of atoms not for charges) can be used as a single parameter to calculate the gamma-ray efficiency at chosen energies.

B.1. Effective atomic number calculation

The following equations were used in this study for Z_{eff}calculation:

$$\alpha_i = \frac{\frac{W_i Z_i}{A_i}}{\sum_i \left(\frac{W_i Z_i}{A_i} \right)}$$

$$Z_{effe} = \left(\sum_i \alpha_i Z_i \right)^{\frac{1}{3.5}}$$

$Z_i$the atomic number, $A_i$masse number and W_i mass fraction of i element.

B.2. Application

For environmental materials, the elemental composition is presented in the next table. As any environmental matrix, the oxides as SiO_2, CO_2, MgO, Al_2O_3, MnO, Na_2O, P_2O_5, SO_3, K_2O, CaO, TiO_2, Cr_2O_3, Fe_2O_3, NiO, ZnO, Rb_2O, SrO, Y_2O_3, ZrO_2, and Nb_2O_5 in the selected matrix are found.

Table B. 1: Elemental composition in mol fraction (Wi (%)) of environmental sample.

Code	B01	B02	Ci01	L01	G01	B03
B_2O_3	-	1.1907	1.5551	-	-	-
CO_2	98.3241	55.1987	40.7576	97.0258	58.8993	14.5546
Na_2O	0.0094	0.1248	0.0883	0.1372	-	0.5902
MgO	0.1514	0.774	1.2411	0.0578	1.0416	2.5093
Al_2O_3	0.0077	2.0961	2.9327	-	0.2071	11.8756
SO_3	0.1867	0.3746	-	0.2449	0.03	3.3987
SiO_2	0.0253	11.8103	11.3851	0.0033	0.7579	50.4724
P_2O_5	0.5644	0.0356	0.0695	0.7596	0.0104	0.1828
K_2O	0.3223	0.2824	0.485	0.6289	0.0211	1.6602
CaO	0.0392	27.2902	37.8041	0.4565	38.931	9.6602
TiO_2	-	0.0609	0.1316	-	-	0.5517
Cr_2O_3	-	0.007	0.0039	-	-	0.0258
MnO	0.0019	0.019	0.022	-	-	0.0334
Fe_2O_3	0.0029	0.699	1.487	-	0.0746	4.3309
NiO	0.0004	0.0016	0.0039	-	-	0.0044
CuO	0.0005	-	-	-	-	-
ZnO	0.0024	0.0026	0.0028	0.0016	0.003	0.0088
Rb_2O	-	0.0008	0.0013	0.0009	-	0.0075
SrO	-	0.0154	0.0488	-	0.0158	0.0396
ZrO_2	-	0.0027	0.0042	-	-	0.0166
Nb_2O_5	-	-	-	-	-	0.0023
Y_2O_3	-	-	-	-	-	0.0023

CONSTRUCTION ALGORITHM FOR ENVIRONMENTAL RADIOELEMENTS ANALYSES IN GAMMA SPECTROMETRY TECHNIQUE

Step 1:

Global Monte Carlo simulation

Experimental data:

- Elemental composition
- Density of sample
- Energy of incident particle
- N_{det}

Data base

Efficiency curves as energy, Z_{eff} and density functions.

Step 2:

Deconvolution process

Experimental data:

- Detectedcounts
- Background
- Counting time
- FWHM (GEB function)
- Distribution type
- E=f(C)
- Dead time

GRAVEL (data base)

Convoluted spectrum and($R^{-1}(E_0,E)$)

GammaSpectrum

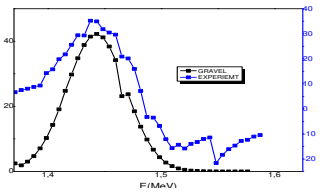

Step 3:

Activity measurement

Experimental data:

- Density of sample
- Incident particleenergy

Database

- Sample weight in kg
- Gamma intensity
- Efficiency values
- Deconvoluted spectrum

$$A\left(Bq.kg^{-1}\right)=\frac{r}{F(E).\varepsilon.\Omega.I_{\gamma}}$$

Dosimetry evaluation

DOSIMETRY ORGANIGRAMM

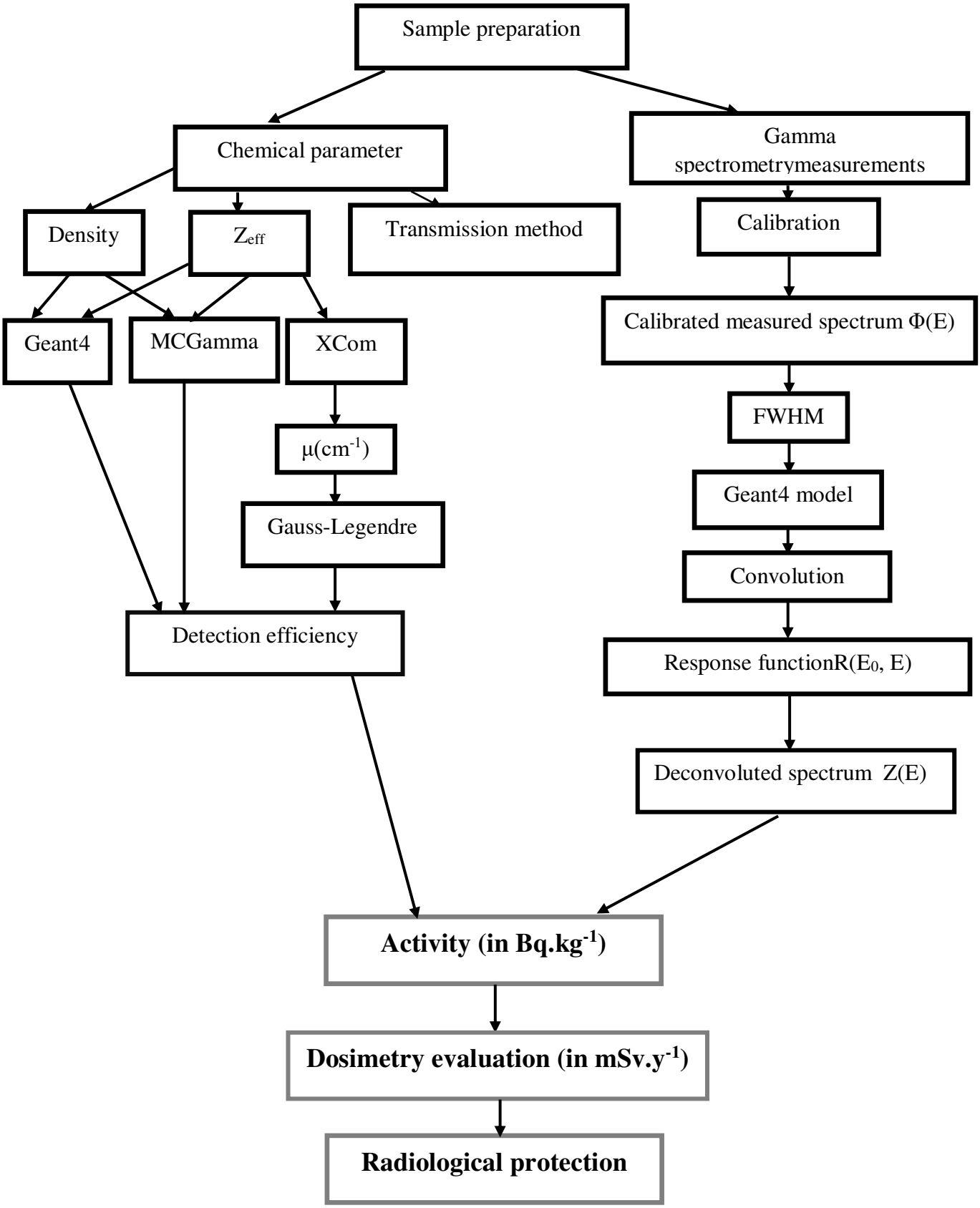

SCIENTIFIC PAPERS AND CONFERENCE LIST

PAPERS

1. Salma Boukhalfa, and Khelifi Rachid, Low-Energy Gamma Unfolding Using NaI(Tl) Geant4 Detector Model and GRAVEL Code, Jordan Journal of Physics (JJP), Accepted.
2. Salma Boukhalfa, Ould Mohamed Mounir, and Khelifi Rachid, Monte Carlo Simulation of NaI(Tl) Detector and GRAVEL Deconvolution for Biological, Geological Samples and Their Dosimetry Evaluation, Journal of Instrumentation (JINST), Accepted .
3. Salma Boukhalfa, and Khelifi Rachid, Gamma-Ray Spectrometry And Elemental Composition Analysis For Natural Radioactivity Evaluation Associated With Radiation Hazard in Construction Materials, Jordan Journal of Physics (JJP), Accepted.

CONFERENCES

1. Salma Boukhalfa, and Khelifi Rachid, Application of Self-Absorption Correction in Gamma Spectroscopy for Different Types of Samples, 2nd International Conference on Radiations and Applications ICRA, 2019.
2. Salma Boukhalfa, and Khelifi Rachid, Calculation Method for Detection Efficiency of Voluminous Samples, 1 Meeting on Monte Carlo Simulations in Radiation Physics, 2018.